Master's thesis

NTNU
Norwegian University of Science and Technology
Faculty of Engineering
Department of Marine Technology

Mathias Tomren

Design and Numerical Analysis of Mooring Systems for Floating Wind Turbines

Comparison of concepts for European Waters

Master's thesis in Marine Technology
Supervisor: Kjell Larsen
June 2022

NTNU
Kunnskap for en bedre verden

Mathias Tomren

Design and Numerical Analysis of Mooring Systems for Floating Wind Turbines

Comparison of concepts for European Waters

Master’s thesis in Marine Technology
Supervisor: Kjell Larsen
June 2022

Norwegian University of Science and Technology
Faculty of Engineering
Department of Marine Technology

NTNU
Norwegian University of
Science and Technology

NTNU Trondheim
Norges teknisk-naturvitenskapelige universitet
Institutt for marin teknikk

MASTER THESIS SPRING 2022

for

Stud. tech. Mathias Tomren

Design and Numerical Analysis of Mooring Systems for Floating Wind Turbines – comparison of concepts for European Waters

Design og numerisk analyse av flytende vindturbiner – case studie for South Europe (France)

Background

In recent years, the wind industry has seen a very fast development, moving from onshore to offshore, and from bottom-fixed shallow water to deep water floating solutions. Many of the floating wind turbine (FWT) concepts have been proposed for water depths larger than 100m. So far, the costs of energy for floating wind turbines is quite high as compared to bottom-fixed turbines, and they are significantly larger than onshore turbines. Therefore, the reduction of cost of the turbines is one of the main challenges for the floating wind turbines. An important contribution to the cost of FWTs is the mooring system.

During the recent development of FWTs for utilizing the offshore wind resource, various technologies from the offshore oil and gas industry have been adopted, including mooring system solutions. The purpose of the mooring system is to keep the floating wind turbine safely at a required position. Today, standard practice is that the mooring system of a single FWT consists of 3-9 mooring lines of chain, chain/steel wire rope or chain/synthetic rope. FWTs are considerably smaller than floating O&G structures. The external loads are characterized with large mean loads (due to the rotor thrust) in moderate wave conditions and high wave motions in extreme wave conditions. In deep water, the mooring system can be particularly expensive and novel solutions are needed.

The importance of the mooring system for a FWT is crucial. The moorings must be reliable enough to prevent any free drift where power cable rupture and collisions are typical consequences. The cost of mooring must be as low as possible to make such developments profitable. Design and optimization of the mooring system is therefore an important task.

The overall objective of this thesis is to perform a detailed assessment of the mooring system for a floating wind turbine. The work shall comprise a description of the status of floating wind turbines, an overview of rules and regulations and a deep dive into design methods and numerical analysis. Both state-of-art mooring systems and novel solutions shall be assessed and compared.

One of the frontrunners for piloting FWTs is France. The site off the west coast of France shall therefore serve as basis for the assessment.

Scope of Work

1) Review relevant literature regarding floating wind turbine concepts and mooring system design. This includes:
- Give a brief description of the status of floating wind turbines concepts.
- Describe different types of mooring systems in general and what types that could be attractive for floating wind turbines in particular. Focus on station keeping principles and main hardware components.

2) Give an overview of some of the design standards for floating wind turbines. Consider IEC 61400, DNV-ST-0437 and DNV-ST-0119. Based on the Design Load Cases (DLCs) given in the rules, propose and discuss relevant cases for ULS design of mooring systems for FWTs.

3) Describe the mooring design process and how numerical mooring analysis can be performed for a FWT. Environmental loads and FWT motions to be included. Different approaches using time-domain analysis methods shall be considered. Topics like how characteristic extreme values is estimated and models for mechanical behavior (tension-elongation) of synthetic ropes shall be described. Theory to be based on the SIMO/SIMA software suite and respective theory and user manuals and other sources. A separate section on aerodynamics shall also be included.

4) Further develop a SIMA model of a 12MW FWT; the 12MW “INO WINDMOOR” model. Describe the model and the different QA checks that is performed. Establish a “base case” mooring system based on chain only to comply with the design requirements outlined in task 2) and operating in France (Jupiter location) in 100m water depth.

5) Perform a numerical simulation comparison study of different mooring concepts and design methods. The numerical simulations shall focus on the use of both a coupled approach based on the use of SIMO and RIFLEX and checks using a quasi-static, un-coupled approach based on SIMO only. Propose, based on results from numerical analysis, alternative and novel mooring systems based on use of synthetic ropes. Such systems may also include clump weight components and buoys, often called “hybrid” solutions. The extent of this task shall be agreed with supervisor.

6) Conclusions and recommendations for further work.

General information

All necessary input data for the simulation case is assumed to be provided by NTNU/Equinor.
The work scope may prove to be larger than initially anticipated. Subject to approval from the supervisor, topics may be reduced in extent.
In the project, the candidate shall present his personal contribution to the resolution of problems within the scope of work.
Theories and conclusions should be based on mathematical derivations and/or logic reasoning identifying the various steps in the deduction.
The candidate should utilise the existing possibilities for obtaining relevant literature.

Report/Delivery
The project report should be organised in a rational manner to give a clear exposition of results, assessments, and conclusions. The text should be brief and to the point, with a clear language. Telegraphic language should be avoided.

The report shall be written in English and edited as a research report including literature survey, description of relevant mathematical models together with numerical simulation results, discussion, conclusions and proposal for further work. List of symbols and acronyms, references and (optional) appendices shall also be included. All figures, tables and equations shall be numerated.

The original contribution of the candidate and material taken from other sources shall be clearly defined. Work from other sources shall be properly referenced using an acknowledged referencing system.

Ownership
NTNU has according to the present rules the ownership of the project results. Any use of the project results has to be approved by NTNU (or external partner when this applies). The department has the right to use the results as if the work was carried out by a NTNU employee, if nothing else has been agreed in advance.

Thesis supervisor**:**
Adjunct Professor Kjell Larsen, NTNU/Equinor

Deadline: 11,06, 2022

Trondheim, January 28th, 2022

Abstract

Renewable energy sources are being added to the energy mix at great speed, with floating offshore wind being one of the leading emerging technologies. One of the key challenges with floating wind technology is the cost, where large contributions are the complex substructures with high production costs and mooring systems originally designed for oil and gas installations. New mooring systems, tailor-made for floating wind turbines, are currently in development. Common for these systems is the use of lighter and new materials, opting for a more cost-effective mooring system.

In this thesis, a numerical simulation comparison study of different mooring concepts and design methods for floating wind turbines has been performed in accordance with ULS design. Six mooring configurations have been investigated in four design load cases acting in two different directions at 100 m water depth. Synthetic fibre ropes are used in five of the mooring configurations, among which, four of the systems with polyester lines and one with nylon lines. The base case mooring configuration is a catenary system with chain mooring lines.

For the chain mooring system, both a quasi-static and fully dynamic mooring analysis has been performed using two different modelling setups in the SIMA software suite. This is done to compare the two calculation procedures in ULS design in shallow waters. For the synthetic systems a newly developed design practice, the SyROPE-model, has been used to model the synthetic fibre ropes in SIMA.

In the comparison between the quasi-static and fully dynamic simulation approaches, it is found large differences in dynamic responses and utilization factors during extreme loading conditions. Even in shallow waters, the quasi-static approach underestimates the tension in the lines due to the dynamic motion of the mooring lines excited by a severe sea state.

Pure synthetic fibre rope mooring configurations are found to be highly suitable for the mooring of floating wind turbines in shallow European waters. For systems with polyester mooring ropes, it may be necessary to incorporate clump weight components to reduce to amount of dynamic responses in the mooring lines. Furthermore, an adequate mooring line length should be used for systems with polyester lines to avoid a too stiff behaviour. Nylon ropes are found to be the best performing material for mooring floating wind turbines in shallow waters due to the material properties resulting in an appropriate stiffness even with short mooring lines.

Sammendrag

Fornybare energikilder tilføres energimiksen i stor fart, med flytende havvind som en av de ledene nye teknologiene. En av hovedutfordringene med den flytende vindteknologi er kostnadene, hvor store bidrag er de komplekse underkonstruksjonene med høye produksjonskostnader og fortøyningssystemer opprinnelig designet for olje- og gassinstallasjoner. Nye fortøyningssystemer, spesiallaget for flytende vindturbiner, er for tiden under utvikling. Felles for disse systemene er bruken av lettere og nye materialer, i søken etter et mer kostnadseffektivt fortøyningssystem.

I denne oppgaven er det utført en numerisk simuleringssammenligningsstudie av ulike fortøyningskonsept og designmetoder for flytende vindturbiner i samsvar med ULS-design. Seks fortøyningskonfigurasjoner er undersøkt i fire designlasttilfeller som virker i to forskjellige retninger på 100 m vanndybde. Syntetiske fibertau brukes i fem av fortøyningskonfigurasjonene, hvor blant annet fire av systemene er med polyesterliner og ett er med nylonliner. Base case fortøyningskonfigurasjon er et catenary system med kjetting liner.

For kjetting systemet er det utført både en kvasistatisk og heldynamisk fortøyningsanalyse ved bruk av to forskjellige modelleringsoppsett i SIMA-programvarepakken. Dette er gjort for å sammenligne de to beregningsprosedyrene i ULS-design på grunt vann. For de syntetiske systemene har en nyutviklet designpraksis, SyROPE-modellen, blitt brukt til å modellere syntetiske fibertau i SIMA.

I sammenligningen mellom den kvasistatiske og heldynamiske simuleringstilnærmingen er det funnet store forskjeller i dynamiske responser og utnyttelsesfaktorer under ekstreme belastningsforhold. Selv på grunt vann undervurderer den kvasistatiske tilnærmingen spenningen i linene på grunn av dynamisk bevegelse av fortøyningslinene som er forårsaket av en alvorlig sjøtilstand.

Fortøyningskonfigurasjoner av ren syntetisk fiber har vist seg å være svært egnet for fortøyning av flytende vindturbiner i grunne europeiske farvann. For systemer med fortøyningstau i polyester kan det være nødvendig å inkorporere klumpvektskomponenter for å redusere mengden dynamisk respons i fortøyningslinene. Videre bør det benyttes tilstrekkelig fortøyningslinelengde for systemer med polyesterliner for å unngå en for stiv oppførsel. Nylontau viser seg å være mest egnede materialet for fortøyning av flytende vindturbiner på grunt vann på grunn av materialegenskapene som resulterer i en passende stivhet selv med korte fortøyningsliner.

Preface

This thesis is the final part of my master's degree in Marine Technology with a specialisation in marine hydrodynamics. The thesis has been completed at the Department of Marine Technology at the Norwegian University of Science and Technology (NTNU) during the spring semester of 2022. A large portion of the necessary input data has been provided by NTNU and Equinor.

I want to express great gratitude to my supervisor, Professor Kjell Larsen, for his supportive guidance and encouragement over the last year. Our weekly meeting has provided me with valuable information and expertise that I have truly benefited from. Further, I would like to thank my fellow student, Kaushik Shiva Manjeri Ramakrishnan, for good discussions and troubleshooting during the project work.

Finally, I want to thank my family and dear partner, Silje, for their support and heartening words over the past few years.

Table of Contents

4 Applied Theory 19

List of Figures

List of Tables

Nomenclature

Abbreviations

ALS	Accidental Limit State
BEM	Blade Element/Momentum
COD	Do-Directional
CoG	Centre of Gravity
DLC	Design Load Case
DLF	Dynamic Load Factor
DOF	Degrees Of Freedom
ECM	Extreme Current Mode
ESS	Extreme Sea State
EWLR	Extreme Water Level Range
EWM	Extreme Wind Speed Model
FLS	Fatigue limit State
FWT	Floating Wind Turbine
HMPE	High Modulus Polyethylene
JONSWAP	JOint North Sea WAve Project
LCOE	Levelized Cost Of Energy
LF	Low Frequency
MBL	Minimum Breaking Load
MIS	Misaligned
MPM	Most Probable Maximum
MSL	Mean Sea Level
MUL	Multi-Directional
NCM	Normal Current Model
NSS	Normal Sea State
NTM	Normal Turbulence Model
NWLR	Normal Water Level Range
RNA	Rotor and Nacelle Assembely
SSS	Severe Sea State
TDP	Touch Down Point
TLP	Tension Leg Platform

ULS	Ultimate Limit State
UNI	Uni-Directional
VSVP	Variable Speed, Variable Pitch
WF	Wave Frequency

Symbols

$\boldsymbol{r}, \dot{\boldsymbol{r}}, \ddot{\boldsymbol{r}}$	Structural displacement, velocity and acceleration vector
$\boldsymbol{R}^S$	Internal structural reaction force vector
ζ	Damping ratio
α	Relative velocity direction in local coordinate system
$\bar{v}(z)$	Average velocity at height z
$\bar{v}_r$	Average velocity at the reference height
β	Frequency ratio
β	Height coefficient
$\boldsymbol{R}^D$	Damping force vector
$\boldsymbol{R}^E$	External force vector
$\boldsymbol{R}^I$	Inertia force vector
$\dot{m}$	Air mass flow rate
ϵ	Strain
ϵ_{dyn}	Dynamic strain
ϵ_{mean}	Mean strain
γ	Gumbel location parameter
γ_m	Soil material factor
γ_{dyn}	Dynamic load factor
γ_{mean}	Mean load factor
λ	Wave length
λ_r	Local speed ratio,
λ_{TSR}	Tip speed ratio
$\mathbf{A}_\infty$	Added mass at infinite frequency
$\mathbf{A}_\infty$	Damping at infinite frequency
$\mathbf{A}(\omega)$	Frequency-dependent mass matrix
$\mathbf{a}(\omega)$	Frequency dependent added mass
$\mathbf{C}(\omega)$	Frequency-dependent potential damping matrix
$\mathbf{c}(\omega)$	Frequency dependent damping
$\mathbf{D_l}$	Linear damping matrix
$\mathbf{D_q}$	Quadratic damping matrix

$\mathbf{h}(\tau)$	Retardation function
$\mathbf{K}(x)$	Stiffness matrix (non-linear)
$\mathbf{Q}(\mathbf{t}, \mathbf{x}, \dot{\mathbf{x}})$	Excitation force vector
$\mathbf{x}$	Position vector
μ_S	Mean value of the breaking strength
Ω	Angular velocity of the rotor
ω	Wave frequency
ω_{ii}	Uncoupled eigenfrequencies
ω_{wake}	Angular velocity imparted to the free stream
$\overline{GM}_L$	Longitudinal metasentric height
$\overline{GM}_T$	Transverse metasentric height
ϕ	Phase angle between load and response
ρ	Water density
ρ_{air}	Density of air
σ	Solidity ratio of the rotor
τ	Gumbel scale parameter
θ	Angle between mooring tension and the horizontal plane
ε	Random phase angle
φ	Angle of attack plus blade pitch angle
φ_0	Incident wave velocity potential
φ_7	Diffraction velocity potential
ζ	Surface elevation
ζ_A	Wave amplitude
A	Cross-sectional area
a	Axial induction factor
a'	Angular induction factor
a_b	Body acceleration
a_d	Dynamic material property synthetic rope
A_r	Rotor disc area
a_r	Relative acceleration between structure and fluid
a_w	Wave particle acceleration
A_{33}	Added mass in heave
A_{44}	Added mass in roll
A_{55}	Added mass in pitch
A_{wp}	Waterplane area

B	Number of turbine blades
b_d	Dynamic material property synthetic rope
C_2	Quadratic current force coefficient
C_a	Added mass coefficient
C_D	Drag coefficient
C_f	Froude-Kriloff coefficient
C_m	Mass coefficient
C_n	Normal coefficient for lift and drag force
C_P	Power coefficient
C_T	Thrust coefficient
C_t	Tangential coefficient for lift and drag force
C_w	Wind force coefficient
C'_{33}	Hydrostatic restoring coefficient in heave
C'_{44}	Hydrostatic restoring coefficient in roll
C'_{55}	Hydrostatic restoring coefficient in pitch
$C_{d,y}$	Drag coefficient in y-direction
$C_{d,z}$	Drag coefficient in z-direction
COV_S	Coefficient of variation of the breaking strength
D	Cross-section diameter
D_H	Mean normal hydrodynamic force
E	Elastic modulus
E_w	Energy in wave
EA_d	Dynamic elastic stiffness
EA_s	Static elastic stiffness
F^{exc}	Wave excitation forces
F_b	Buoyancy force
F_H	Mean tangential hydrodynamic force
f_s	Static material property synthetic rope
$F_y(y)$	Gumbel cumulative distribution function
$f_y(y)$	Gumbel probability density function
F_{drag}	Aerodynamic lift force
F_{lift}	Aerodynamic lift force
F_m	Force per unit length - Morison equation
g	Acceleration of gravity
g_s	Static material property synthetic rope

H	Wave height
h	Distance from the reference origin to the rotor hub
h	Vertical distance between mooring attachment point and seafloor
H_s	Significant wave height
$H_{s,50}$	50-year value of the significant wave heigh
$H_{s,SSS}$	significant wave height of severe sea state
I_{xx}	Moment of inertia about x-axis
I_{yy}	Moment of inertia about y-axis
I_{zz}	Moment of inertia about z-axis
k_E	Elastic stiffness
k_G	Geometric stiffness
K_{44}	Hydrostatic stiffness in roll
K_{66}	Mooring stiffness in yaw
l	Total length of mooring line
M	Mass matrix
M_{44}	Total inertia in roll
M_{66}	Total inertia in yaw
n	Structure normal component
P	Power
p_0	Ambient pressure
p_d	Linear dynamic pressure
p_N	Force acting normal to the rotor plane
p_T	Force acting tangential to the rotor plane
Q_a	Aerodynamic torque
q_{cu}	Current drag force
q_{ext}	Any other excitation forces
$q_{wa}^{(1)}$	First order wave excitation force
$q_{wa}^{(2)}$	Second order wave excitation force
q_{wi}	Wind drag force
q_w	Wind force
R	Radius of the rotor
r	Local radius of the rotor
R_0	Excitation force for 1-DOF system
R_c	Characteristic geotechnical anchor resistance
R_d	Design anchor resistance

s	Suspended length of mooring line
$S(\omega)$	Spectral density
S_0	Mean wetted structure surface
S_c	Characteristic capacity of the mooring line
S_C^*	Statistically uncertain characteristic capacity
S_{mbs}	Minimum breaking strength
T	Mooring line tension
t	Time
T_a	Aerodynamic thrust
T_d	Design tension
T_p	spectral peak period
T_x	Horizontal component of line tension
T_z	Vertical component of line tension
$T_{c,dyn}$	Characteristic dynamic tension
$T_{c,mean}$	Characteristic mean tension
T_{dyn}	Dynamic stiffness
T_{mean}	Mooring line mean tension
T_{MPM}	Most probable max tension of a time series
$T_{n,heave}$	Natural period in heave
$T_{n,pitch}$	Natural period in pitch
$T_{n,roll}$	Natural period in roll
u_b	Body velocity
u_c	Current velocity
u_r	Relative velocity between structure and fluid
u_w	Wave particle velocity
U_{10}	50-year value of the current velocity
U_{50}	50-year value of the current velocity
$u_{c,r}$	Relative velocity between low frequency body velocity and current velocity
UF	Utilization factor
v	Wind velocity
v_0	Inflow air velocity
v_1	Wake air velocity
v_A	Air velocity at the rotor disc
v_r	Relative wind speed between the structure and wind
V_{hub}	10-minute average wind speed at hub height

V_{in}	Cut-in wind speed
V_{out}	Cut-out wind speed
V_{ref}	50-year value of the wind speed
V_{sub}	Submerged volume
w	Wet weight per unit length of the mooring line
w_{air}	Weight in air
$x, \dot{x}, \ddot{x}$	Position, velocity, acceleration
X_B	Horizontal distance between anchor and TDP
x_h	Horizontal distance between TDP and mooring attachment point
X_l	Horizontal distance between anchor and mooring attachment point
y	Vertical distance from seafloor to mooring element
z	Depth/height below/over mean water line
z_r	Reference height

1 Introduction

Clear signs of change in the world's energy systems are emerging after over two years of the Covid-19 pandemic. In 2020, even with economies struggling to hold the weight of restrictions and lockdowns, additions of renewable sources of energy such as wind and solar increased at the fastest rate in two decades [1]. In the midst of the recovery from the pandemic, the Russian invasion of Ukraine has made the deployment of more renewables a strategic imperative for many countries in the European Union to accelerate the clean energy transition in order to reduce the dependency on imported fossil fuels from Russia [2].

Advancements in technology for renewable energy are steadily being made, making it more economically viable for large projects with high potential for energy production. One of the technologies that have experienced vast development in the past few years is Floating Wind Turbines (FWT). Several floating wind farms are now up and running around the globe where the Kincardine 50 MW project is the latest and largest operational offshore floating wind farm in the world, showing the feasibility of the technology. The first floating wind farm, Hywind Scotland, has been in operation since 2017 and has achieved the highest average capacity factor of all offshore wind farms in the UK [3], proving that the floating wind technology may match or even out-compete bottom fixed offshore turbines.

FWTs are a major enabler to harnessing enormous resource potentials. An estimated 81% of total offshore wind electricity potential is located in waters deeper than 40 meters [4]. In these areas the wind is more consistent and stronger due to little or no disturbance from land areas, allowing for a more reliable power generation. Europe has a major opportunity with FOW due to extraordinary power production potential in the surrounding waters. With a potential for floating wind capacity of 4000 GW, it has a significantly higher potential than the US and Japan combined [5]. The floating wind technology also allows for less concern regarding noise and visual pollution when used in areas far from shore. Here, noise regulations to protect local residents are not needed allowing for larger turbines to be installed.

One of the key challenges with floating wind technology is the cost. Bottom-fixed wind projects are currently managing to reach a Levelized Cost Of Energy (LCOE) below 50 USD/MWh, while the first floating wind farms have seen LCOE exceed 200 USD/MWh [3]. There are numerous reasons for the higher cost of floating wind farms, much of which is due to their currently small size and the immaturity of the technology. However, some specific features of floating wind technology need to be enhanced for the technology to be profitable. Firstly, a floating structure is much more complex than for instance a fixed monopile with a much higher design and production cost. A typical substructure for a FWT requires more than double the amount of steel as a monopile supporting the same turbine [3]. Further, the dynamic behaviour of the floater sets requirements for power cables and a high capacity mooring system. DNV predicts that by 2050 the cost of floating wind is reduced by 70% as illustrated in Figure 1.1.

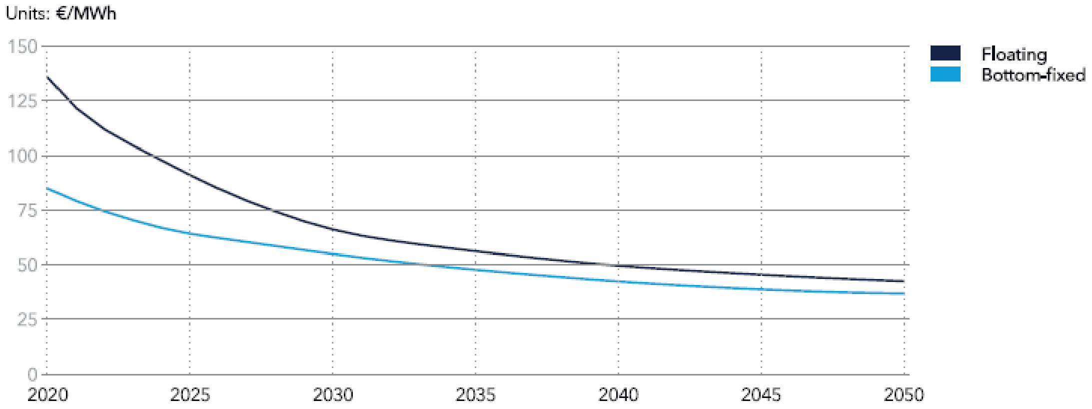

Figure 1.1: Predicted LCOE of offshore wind [3].

One of the key reasons for the predicted reduction in cost is the new and improved design of floating wind. Over 40 concepts are currently in development with new concepts frequently being announced. Common to all the concepts is the mooring system, where significant development is anticipated. Present-day FWTs are commonly moored by systems build-up by chain, wire rope, or a combination of the two. This is a highly cost demanding system due to the large steel weight and demanding installation requiring powerful installation vessels. New mooring systems are in development employing lightweight synthetic fibre mooring lines. Systems of such configuration have a high potential in reducing the cost of mooring systems for FWTs, due to a lighter weight, high fatigue performance and easier installation.

1.1 Scope of Work

The overall objective of this thesis is to perform a detailed assessment of the mooring system for a floating wind turbine. The work shall comprise a description of the status of floating wind turbines, an overview of rules and regulations and a deep dive into design methods and numerical analysis. Both state-of-art mooring systems and novel solutions shall be assessed and compared. The work includes a review of relevant literature regarding floating wind turbines and mooring system design. The literature review also includes an overview of relevant design standards where DNV-ST-0119 [6] is used as the main guidance for mooring system design. The relevant theory used in the time-domain simulation software suite SIMA is described. One of the frontrunners for piloting FWTs is France. The site off the west coast of France shall therefore serve as basis for the assessment.

A SIMA model of the 12 MW INO WINDMOOR FWT has been further developed to perform a numerical simulation comparison study of different mooring concepts and design methods. A base case catenary mooring system with chain mooring lines has been established where both a quasi-static and fully dynamic approach has been used to calculate the mooring line tensions. Several alternative and novel mooring systems based on the use of synthetic ropes have been purposed and analysed with the intent of being deployed in European waters.

Work done in this thesis is the continuation of my specialisation project thesis [7] completed during the autumn semester of 2021, where parts of the presented theory used in this thesis were mapped and presented. Work done in the project thesis also includes the development of a SIMO-model of the 12 MW FWT, including decay simulations and a load-displacement study.

1.2 Report Outline

- Section 2-4 gives the relevant theory to understand the fundamental concepts used in the design of mooring systems of FWTs.
- Section 5 and 6 give a detailed overview of how the design load cases are defined and of the modelling procedure in SIMA.
- Section 7 presents results from various quality analyses where the behaviour of the developed SIMA-models with a chain mooring system is controlled in addition to a seed convergence study.
- Section 8 presents the investigated mooring configurations covered in this thesis.
- Section 9 and 10 present the obtained results and concluding points in addition to recommendations for further work.

2 Floating Wind Turbine Concepts

Four main concepts for the floating substructure have emerged in the development of offshore floating wind. The design of the substructures is heavily inspired by knowledge and experiences from the oil and gas industry resulting in resilient structures. The main concepts will be described in the following sections. Figure 2.1 gives an overview of the main concepts that are currently in development for offshore floating wind.

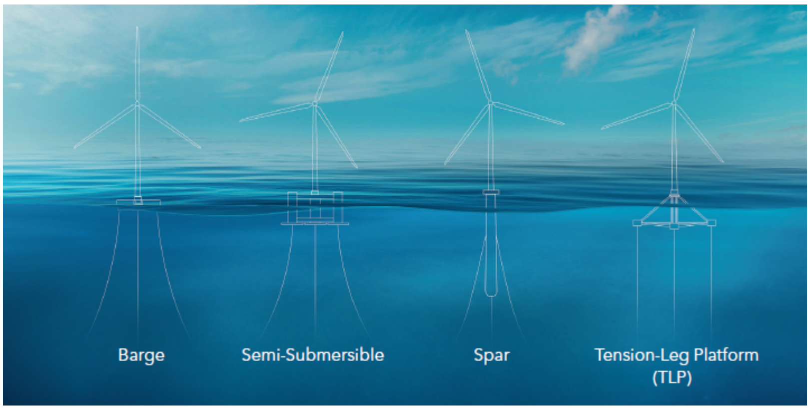

Figure 2.1: Main concepts for offshore floating wind [8].

2.1 Semi-submersible

The semi-submersible substructure is typically built up by a top deck supported by vertical columns that are connected by pontoons or braces. The vertical columns provide hydrostatic stability to the structure due to the large waterplane area moment of inertia. The pontoons or braces provide additional buoyancy to the structure. Different concepts within the semi-submersible category have been proposed with the turbine installed either in the centre of the structure or on top of the vertical columns. Common mooring line configuration is the use of three mooring lines, one connected to each of the offset columns. The semi-submersible substructure is flexible with respect to water depths due to the moderate draft of the structure.

The latest project to be installed utilising a semi-submersible substructure is the Kincardine Offshore Wind project located approximately 15 kilometres off the southeast coast of Aberdeen, Scotland. The wind farm consists of five 9.525 MW wind turbines resulting in a combined power production of 50 MW [9]. One of the installed wind turbines from the Kincardine project is illustrated in Figure 2.2.

Figure 2.2: One of the semi-submersible wind turbines installed in the Kincardine Offshore Wind project [10].

2.2 Spar Platforms

Spar platforms are deep draft structures that achieve their stability by having the centre of gravity below the centre of buoyancy. The spar platform is essentially a thin vertical buoy with a small waterline area, resulting in the behaviour of small and slow motions in the sea. The mooring system of a spar platform is similar to the type used for the semi-submersible, with three catenary mooring lines distributed with a 120-degree spacing around the substructure. The challenge with the spar platform is the large draft of the structure, which for the Hywind Tampen project is planned to be close to 90 m [11]. The large draft limits the number of possible assembly sites for the FWTs due to the need for a deep water port and a towing route out to the farm location with adequate depth. The Hywind Tampen wind farm is to be situated on the Norwegian west coast and will consist of eleven 8 MW turbines providing electrical power to the Snorre and Gullfaks field operations [12]. Figure 2.3 illustrates one of the FWTs for the Hywind Tampen project.

Figure 2.3: Illustration of the Hywind Tampen wind farm [13].

2.3 Tension Leg Platform

Tension Leg Platforms (TLPs) are bottom founded floating structures that are moored to the seabed by steel tethers. The TLP has a larger buoyancy than its displacement creating a force upwards that tensions the tethers. This effect gives high stability and stiffness for the vertical motions of the platform, meaning heave roll and pitch motions. Stiffness in the surge, sway and yaw motions are provided thru geometric stiffness. No major offshore wind projects utilizing the TLP technology is currently under development, but several companies are in the process of developing concepts for wind turbines larger than 10 MW. One concept in development is the joint venture of MODEC, Toyo Construction, and Furukawa Electric in Japan, using a substructure similar to the semi-submersible concept but moored using tensioned tethers. Another TLP concept is proposed by Bluewater, illustrated in Figure 2.4.

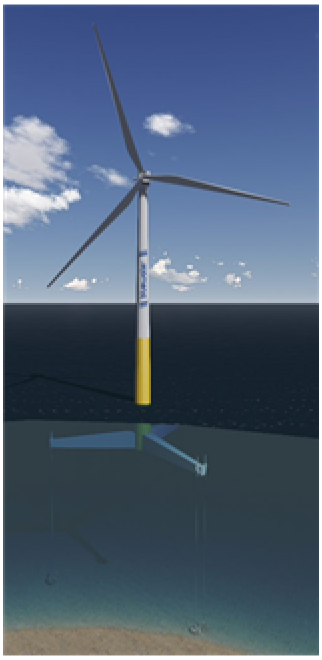

Figure 2.4: Illustration of the Bluewater TLP [14].

2.4 Barge Platforms

The barge concept utilizes a flat-bottomed large-volume type foundation that is stabilized by the waterplane area. There exist only a few barge-type concepts for floating offshore wind turbines today with one of the latest concepts being a squared ring-shaped support structure with a moonpool developed by BW Ideol called FLOATGEN. The purpose of the moonpool is to act as a damper to the structure's motions. The concept from Ideol is shown in Figure 2.5. The FLOATGEN demonstrator is installed off the coast of France and has a 2 MW wind turbine installed onboard. The FLOATGEN uses six synthetic fibre mooring lines made of nylon and is a world-first for a permanent mooring system of this size using nylon fibre mooring lines.

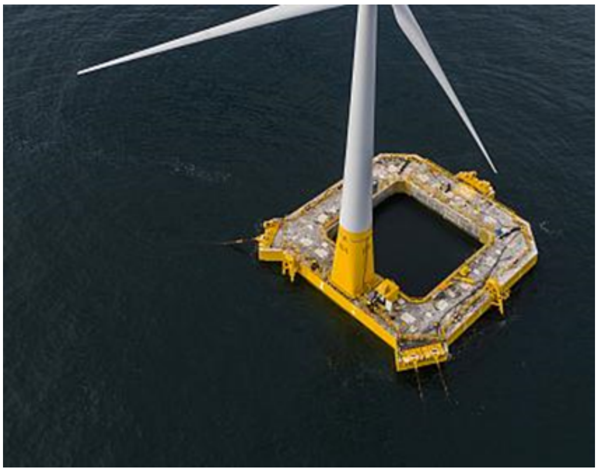

Figure 2.5: Barge-type floating wind turbine, BW Ideol FLOATGEN concept [15].

3 Station Keeping of Floating Wind Turbines

A station keeping system refers to the mooring system of a floating structure based on either a catenary or taut system. Alternatively, the station-keeping system could be based on dynamic positioning, but this is not considered to be applicable for FWTs due to high cost and long operational duration.

The following sections will focus on the fundamental concepts for state-of-the-art moorings systems used for offshore floating wind and relevant hardware components. Figure 3.1 gives an overview of the main mooring system components covered in this report that are used to make a complete mooring system.

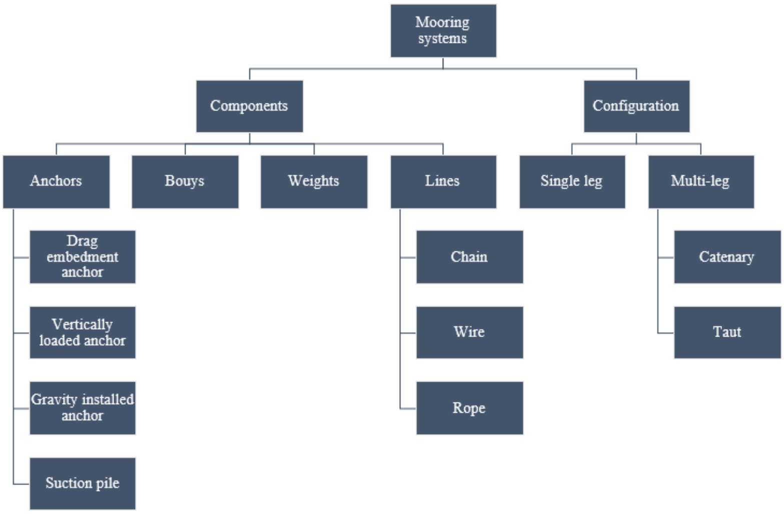

Figure 3.1: Overview of elements combined to make a complete mooring system.

3.1 Functional Requirements

The main task of the mooring system is to restrain the FWT at its designed location under extreme loading conditions and ensure its survivability, while also permitting efficient power production during operational conditions. The horizontal offset of the FWT should be limited such that power umbilicals are guarded against damage and avoid collision with other FWTs. The mooring system should be designed with an adequate lifetime before replacement is needed, generally, the systems are designed to match the lifetime of the wind turbine.

3.2 Mooring Systems

Mooring systems can be categorised into catenary mooring systems and taut leg mooring systems depending on the configuration [16], as illustrated in Figure 3.2.

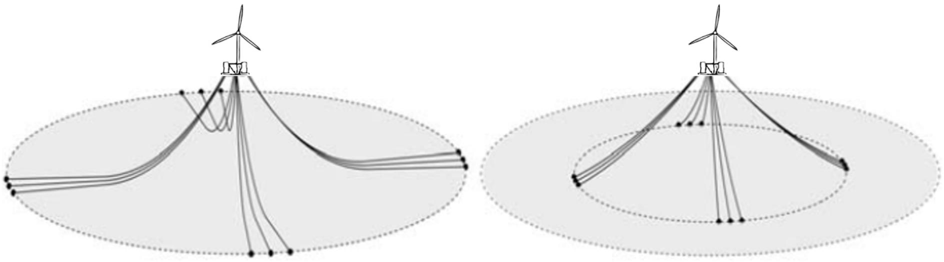

Figure 3.2: Catenary mooring system (left) and taut leg mooring system (right) [16].

A catenary mooring system has mooring lines where a part of the line is lying on the seabed when the system is in static equilibrium. Restoring forces are introduced when the mooring line is lifted from the seabed and the weight of the line increases. The taut leg system does not have any portion of the line lying on the seabed but has taut mooring lines from the anchor up to the attachment point on the floater. This results in a smaller footprint of the mooring system and less material usage for mooring lines compared to the catenary system. Due to the taut lines, the floater motions are absorbed by the line tensile stretch and not a geometric stiffness[16]. A more detailed description of the two systems is provided in the following sections.

3.3 Catenary Lines

Catenary lines are the most widely used mooring configuration and are viewed as the traditional mooring system. In Figure 3.3 a catenary mooring line is suspended from a submerged point A on a floating structure and is anchored to the seabed in point B. As point A is moving horizontally through the positions A_1 - A_4 the portion of the catenary line laying on the seabed decreases to none in point A_4. The tension in the line at point A is due to the total weight of the suspended line in seawater. Due to an increasing portion of the line being suspended as the structure move through the points A_1 - A_4 the tension in the line at point A also increases. This effect, coupled with the simultaneous decrease in line angle to the horizontal, generates a horizontal restoring force that increases with the structure offset in a non-linear manner [17].

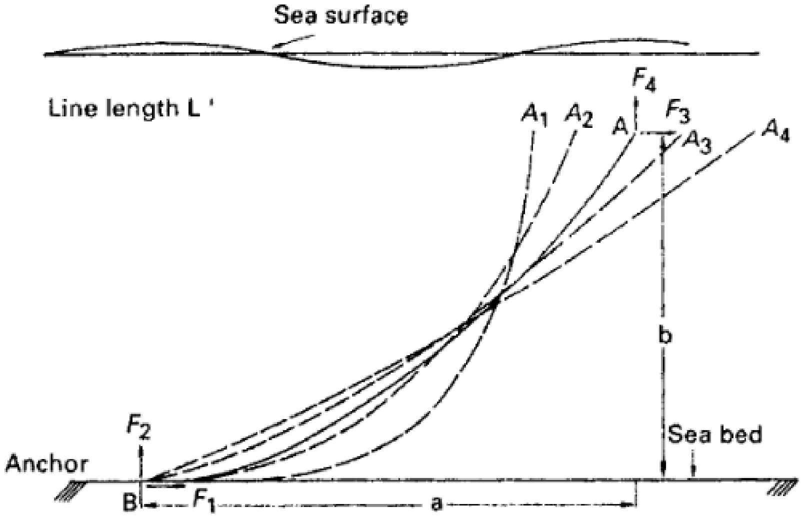

Figure 3.3: The behaviour of a catenary mooring line [17].

This non-linear restoring force and geometric shape can be described by the catenary equations. The equations are derived by considering a mooring line as displayed in Figure 3.4 in the x-z-plane. Bending stiffness and dynamic effects in the line is neglected, which for chain and wire is an appropriate approximation [18].

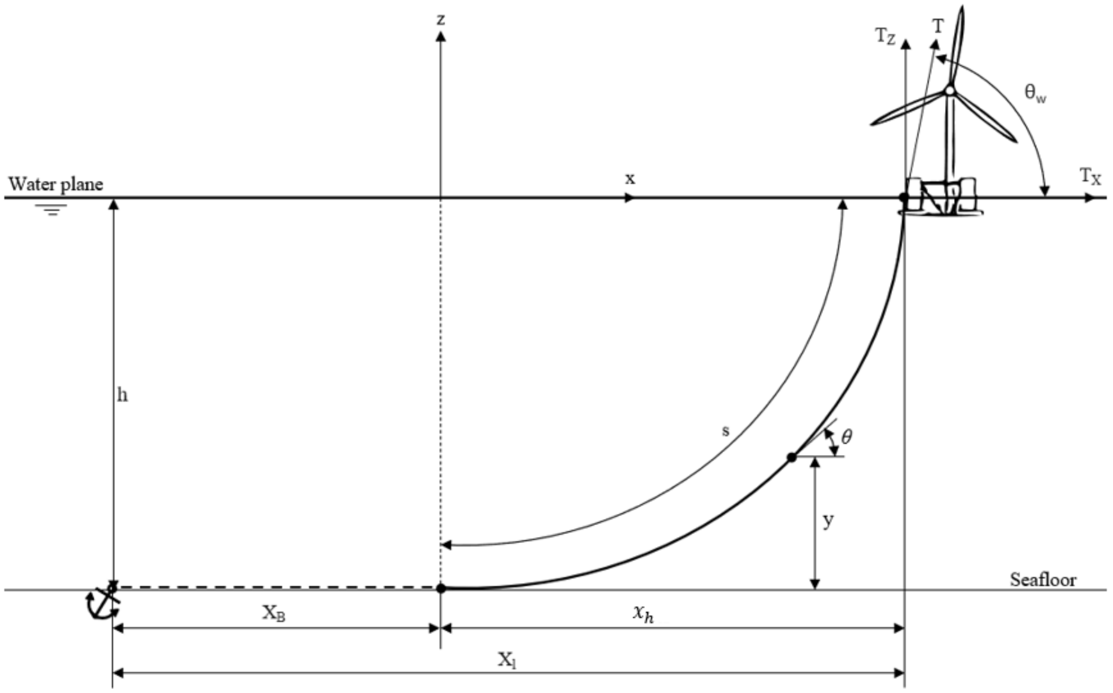

Figure 3.4: The geometry of a catenary line.

In Figure 3.4, T_z and T_x denotes the vertical and horizontal component of the line tension respectively. s is the suspended length from the attachment point on the floater down to the Touch Down Point (TDP) at the seafloor. h is the vertical distance from the attachment point to the seafloor.

In Figure 3.5 one element from the line is shown. Where D_H and F_H denote the mean hydrodynamic forces per unit length in the normal and tangential direction respectively. T is the effective tension, w is the wet weight per unit length, A is the cross-sectional area of the cable line and E is the elastic modulus.

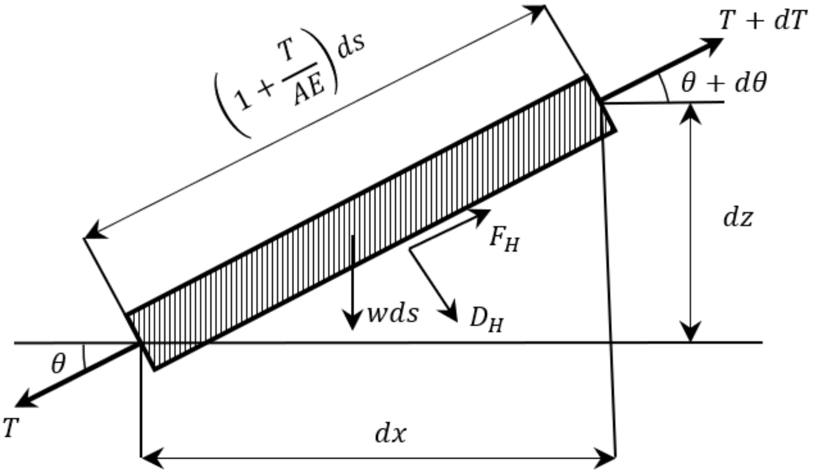

Figure 3.5: Forces acting on an anchor line element, adapted from [18].

From Figure 3.5 the following relationship can be obtained

$$\mathrm{d}T = [wsin(\theta) - F_H(1 + \frac{T}{AE})]\mathrm{d}s$$

$$T\mathrm{d}\theta = [wcos(\theta) + D_H(1 + \frac{T}{AE})]\mathrm{d}s$$

These equations are the governing differential equations for a mooring line considering both mooring line dynamics and elastics. The equations are non-linear, and it is in general not possible to find an explicit solution. Neglecting the dynamic loads on the mooring line and the effect of elasticity results in a static solution to the equations from where the catenary equations emerge as a solution to the following set of equations [16]:

$$\mathrm{d}T = wsin(\theta)\mathrm{d}s \tag{3.1}$$

$$T\mathrm{d}\theta = wcos(\theta)\mathrm{d}s \tag{3.2}$$

Solving Equation 3.1 and 3.2 with the appropriate boundary conditions gives the solution to the catenary equations as follows:

$$s = \frac{T_x}{w} sinh(\frac{w}{T_x}x) \tag{3.3}$$

$$h = \frac{T_x}{w}\left[cosh(\frac{w}{T_x}x) - 1\right] \tag{3.4}$$

The horizontal distance between the TDP and the attachment point on the floater is given by:

$$x_h = \frac{T_x}{w} ln\left[1 + \frac{hw}{T_x} + \sqrt{\left(1 + \frac{hw}{T_x}\right)^2 - 1}\right] \tag{3.5}$$

The tension in the line can be expressed as:

$$T = T_x + wh \tag{3.6}$$

or

$$T = \sqrt{T_x^2 + T_z^2} \tag{3.7}$$

Where the vertical component of the tension is equal to the weight of the suspended line and can be expressed as:

$$T_z = ws \tag{3.8}$$

To calculate the mean position of the floater a fixed point is needed as a reference, for this, the anchor point is selected. The horizontal distance between the anchor point and attachment point on the floater can be written as:

$$X_l = l - s + x_h \tag{3.9}$$

Where l is the total length of the mooring line. By combining Equation 3.3 and 3.5 into Equation 3.9 the following can be written for a line with no elasticity

$$X_l = l + \frac{T_x}{w} cosh^{-1}\left(1 + \frac{wh}{T_x}\right) - \sqrt{h\left(h + \frac{2T_x}{w}\right)} \tag{3.10}$$

This is often denoted as the line characteristics and is the relation between the floater offset and the horizontal tension in the line for a given water depth and line weight [19].

3.3.1 Mooring Line Stiffness

The stiffness of a mooring line is composed of two contributions, axial elongation and geometric change of the mooring line during a change in position of the floating structure. Thus, the total stiffness of a mooring line is the product of axial stiffness, EA, and geometric stiffness, as shown in Figure 3.6.

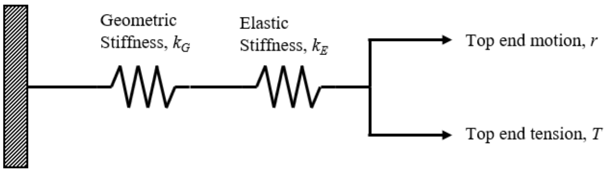

Figure 3.6: Stiffness contributions to mooring line stiffness in a quasi-static analysis.

The resulting total mooring line stiffness can be found through the following relation:

$$\frac{1}{k_{\text{Total}}} = \frac{1}{k_{\text{elastic}}} + \frac{1}{k_{\text{geometric}}} \tag{3.11}$$

According to Faltinsen [18], the horizontal in-elastic geometric stiffness of a catenary mooring line may be expressed as:

$$k_G = \frac{\mathrm{d}T_{\mathrm{H}}}{\mathrm{d}X} = w\left[\frac{-2}{\left(1+2\frac{T_H}{wh}\right)^{\frac{1}{2}}} + \cosh^{-1}\left(1+\frac{wh}{T_H}\right)\right]^{-1} \tag{3.12}$$

Geometric stiffness will be the dominating component for catenary systems consisting of chain and steel wire ropes due to the high weight of the components, while for the taut systems the axial stiffness will be dominating.

3.4 Synthetic Lines - Elasticity models

Synthetic fibre lines can have several advantages over a catenary chain or wire lines in deep water. They are substantially lighter, highly flexible and can absorb dynamic motions through extension without causing an extreme dynamic tension [17]. Further, the vessel experiences smaller vertical loads due to the lighter weight of the rope, a reduced line length is needed which results in a smaller seabed footprint and generally a reduction in the mean- and low-frequency platform offsets is attained [17].

A major disadvantage of synthetic fibre ropes is their complex material and mechanical properties that are not as well understood as for chain and wire ropes. Due to this, the design of mooring systems containing synthetic fibre ropes may be too conservative resulting in the loss of some of the advantages that the synthetic fibre rope has. Also, mooring systems that use polyester in the mooring lines tend to be too stiff in shallow waters due to the properties of the polyester rope.

For conventional mooring lines, both the geometric and elastic stiffness characteristics are important for describing the restoring properties and stiffness of the mooring system. However, for systems with synthetic line segments, it is the axial elastic properties of the synthetic rope that determines the resulting line stiffness [20]. Understanding the behaviour of synthetic ropes becomes especially important for mooring systems of the taut leg configuration where elastic stiffness is the dominating component.

The conventional model for axial elastic stiffness of a synthetic rope is a linear stiffness model given as:

$$T = EA \cdot \epsilon \tag{3.13}$$

where T is the line tension, EA is the axial stiffness and ϵ is the line strain. Until recently, the industry has relied on simplified models such as the upper-lower bound model which defines lower and upper bound stiffness values as an approximation. The lower bound represents the static rope stiffness while the upper bound represents the dynamic stiffness. Using only two limiting values to represent the complicated behaviour of a synthetic rope may result in overly conservative or non-conservative analysis results [16]. The desire is to have a more advanced, but still manageable design practice that allows for a more optimised design.

A conceptual model for the behaviour of synthetic ropes has newly been developed, referred to as the "SyROPE" model. This model has been developed from the tension-strain characteristics observed and measured during full-scale testing [20], the model is shown in Figure 3.7.

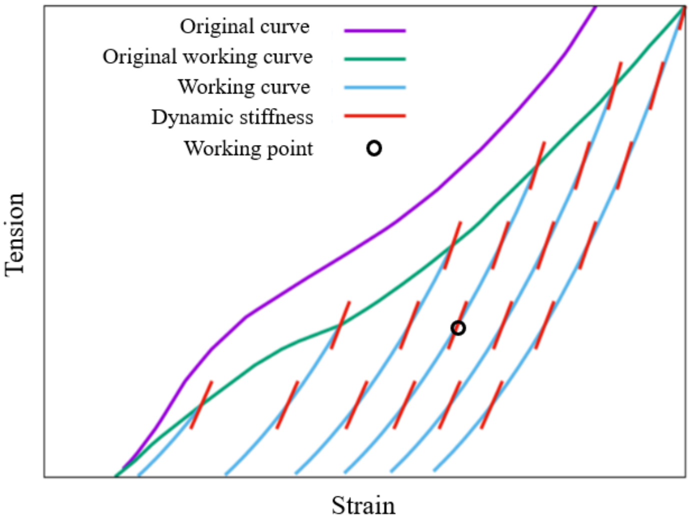

Figure 3.7: Principle tension-strain curves used in the SyROPE model [20].

The model defines the following characteristics [20]:

Working point:
The working point is the combination of mean strain and mean tension around which the dynamic wave frequency and low-frequency responses take place. For polyester ropes most of the change in length occurs during the first 10-20 min after the mean environmental loads have changed, a good approximation will hence be to analyse the mooring lines with the length they will have at the end of a 3-hour sea state [21].

Original curve
The original curve represents the tension versus strain that is obtained during the first, quick loading of a new rope.

Original working curve
The original working curve represents the stationary working point if the rope is at its historical highest tension, and as the permanent strain has been taken out.

Working curve
The working curve represents the working points when the rope is at a lower mean tension than the preceding maximum tension. The working curve is a downwards working curve as defined by

the previous highest mean tension. To further refine the model an upwards working curve may be defined. Together the upwards and downwards working curves will form a convex shape. During a 3-hour stationary sea state, each rope will be represented by a working point on the working curve as defined by the highest preceding mean tension. The rope will have a mean working length defined by the working curve and the mean tension. From the working curve, the static elastic stiffness is defined, which shall be used for estimating offset due to mean environmental loads.

Dynamic Stiffness
The dynamic stiffness will increase to some degree with the mean tension. Other than that, it is assumed to be linear and independent of tension amplitude and frequency. The dynamic elastic stiffness is to be used when estimating response due to WF and LF excitation. Observing Figure 3.7 the dynamic stiffness can be seen to be somewhat higher than the static elastic stiffness.

3.4.1 Static Elastic Stiffness Model

As stated, the static elastic stiffness is described by the non-linear working curves. The working curve during operation may be regarded as constant if the tension is lower than the installation tension. The relation between change in mean tension and mean strain is proposed as:

$$dT_{mean} = EA_s \cdot d\epsilon_{mean} = (100 \cdot g_s \cdot T_{mean} + f_s \cdot MBL)d\epsilon_{mean} \tag{3.14}$$

Where MBL is the minimum breaking load of the rope, EA_s is the static elastic stiffness, and f_s and g_s are constants estimated from full-scale testing.

The relation in Equation 3.14 can be re-written as a differential equation with the general solution as:

$$T_{mean} = C_1 \cdot exp(100 \cdot g_s \cdot \epsilon_{mean}) - \frac{f_s \cdot MBL}{100 \cdot g_s} \tag{3.15}$$

Imposing that $T_{mean}(0) = 0$, gives $C_1 = \frac{f_s \cdot MBL}{g_s 100}$ Equation 3.15 becomes:

$$\frac{T_{mean}}{MBL} = \frac{f_s}{100 \cdot g_s}[exp(100 \cdot g_s \cdot \epsilon_{mean}) - 1] \tag{3.16}$$

Inserting values for f_s and g_s corresponding to the properties of polyester and nylon ropes given in [20] yields the results given in Figure 3.8.

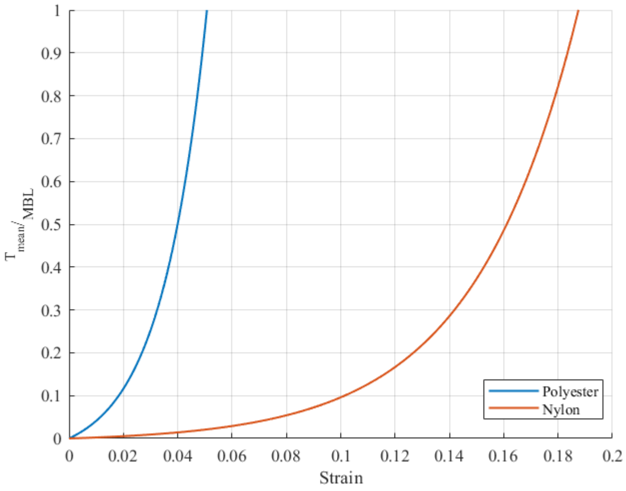

Figure 3.8: Static elastic stiffness (working curves) for polyester and nylon ropes.

3.4.2 Dynamic Elastic Stiffness Model

In the SyROPE-Model the dynamic elastic stiffness is proposed as linear with tension amplitude and is considered to be independent of frequency. Tension responses due to WF and LF excitation are determined through the dynamic elastic stiffness. The model in generated in a similar manner as for the static stiffness model:

$$\frac{dT_{dyn}}{d\epsilon_{dyn}} = EA_d = (100 \cdot b_d \cdot T_{mean} + a_d \cdot MBL) \tag{3.17}$$

Which gives the following relation for dynamic stiffness as function of mean tension:

$$\frac{EA_d}{MBL} = 100 \cdot b_d \cdot \frac{T_{mean}}{MBL} + a_d \tag{3.18}$$

where EA_d is the dynamic stiffness and a_d and b_d are constants estimated from full scale testing. Values for a_d and b_d are taken from[20] for polyester and nylon ropes. Using these values in Equation 3.18 yields the proposed model for dynamic elastic stiffness as shown in Figure 3.9.

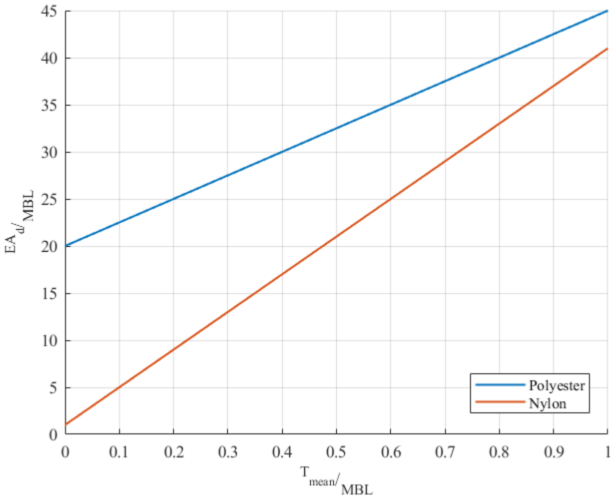

Figure 3.9: Dynamic elastic stiffness for polyester and nylon ropes.

3.5 Mooring Hardware Components

A mooring system is built up from several components contributing to the overall characteristics of the system. Depending on location and system requirements the composition of the various components may vary from one mooring system to another. The following sections will describe the main hardware components used in state-off-the-art mooring systems.

3.5.1 Chain

Chain is the most commonly used component in mooring lines with the typical size for chain links being in the range of 70 to 200 mm. Chains can be divided into two primary constructions, studlink and studless chain, as shown in Figure 3.10.

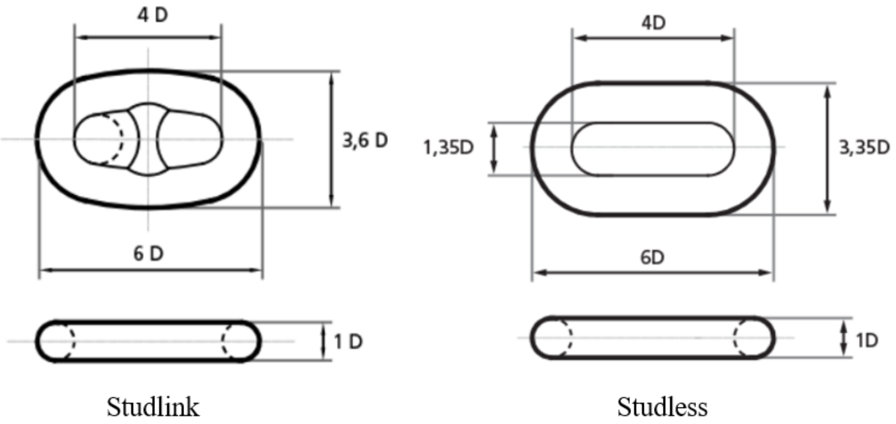

Studlink

Studless

Figure 3.10: Studlink and studless chain links [22] [23].

The studlink chain has a stud fitted inside the link to provide stability to the link and avoid entangling of the chain while it's being handled. Hence, the studlink chain is most commonly used in moorings that have to be deployed and retrieved frequently during their lifetime. The studless chain is about 10% lighter than the studlink chain due to not having the stud fitted, but still has the same breaking strength [16]. Studless chain is preferably used in permanent mooring systems due to the lower weight and longer fatigue life, making it more suited for use in mooring systems with a design life of 20-30 years. Further, the studless chain has a simpler manufacturing process and is easier to inspect.

Mooring chains used in offshore applications are made in different grades which range from R3, R3S, R4, R4S and R5 where R5 has the highest breaking strength.

3.5.2 Wire Rope

Wire ropes consist of individual wires wound in a helical pattern to form a strand. The pitch of the helix in the strand determines the flexibility and stiffness. Typical wire ropes commonly used in offshore mooring lines are of the configuration six-strand, eight-strand and spiral strand, as displayed in Figure 3.11.

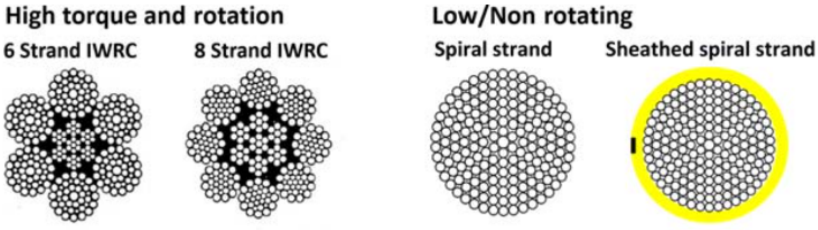

Figure 3.11: Typical wire rope configurations [16].

A wire rope will have lighter weight and higher elasticity than a chain of an equivalent breaking strength and is typically used in combination with a chain to make up a complete mooring line in deep waters where an all chain design becomes too heavy.

Temporary mooring systems often make use of the six-strand or eight-strand wire rope due to its high flexibility making it easy to handle. A disadvantage with these wire ropes is that they generate torque as tension increases [16]. This effect must be considered when using a six-strand wire rope in conjunction with synthetic ropes as the wire rope would tend to unwind itself, using the polyester rope as a swivel. Permanent mooring systems mostly use spiral strand wire ropes which are built up by many individual wires that form a single strand. The wires are laid in layers with each layer wrapped in the opposite direction. This provides torque balancing for the rope and prevents it from twisting during tension. For permanent applications, it is common to use spiral strand wire ropes that are protected from corrosion by an outer coating made of polyethylene.

3.5.3 Synthetic Ropes

Figure 3.12 represents a typical construction of a synthetic rope used in mooring applications. The rope is built up by several sub-ropes laid in parallel construction. The sub-ropes are made up of strands and can be constructed in parallel, braided or laid depending on the desired characteristics of the rope. The bundle of sub-ropes forms a core that is protected with a soil filter to stop soil ingress and a braided jacket to protect against damage from external abrasion. The external jacket does not have any tensile load-bearing capability.

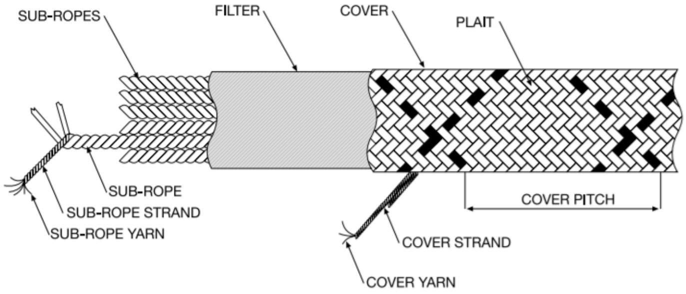

Figure 3.12: Example of polyester rope construction [24].

As mentioned in Section 3.4 the synthetic lines have a very different behaviour compared to a system build-up by components made out of steel. One distinct behaviour that needs to be taken into account when designing a system with synthetic mooring lines is construction stretch. Synthetic ropes exhibit axial load-elongation characteristics that are nonlinear, depending on loading type, and varying with time and loading history [16]. This will cause the installed length of the rope after pretension to be longer than the manufactured length. Additionally, the length of the rope will increase after every historically largest loading. This behaviour makes it difficult to determine the length of the polyester ropes after some time in operation.

Currently, polyester is the most commonly used material in synthetic fibre ropes due to its low weight and cost combined with low axial stiffness and high fatigue resistance. However, there exists a wide range of other synthetic materials that can be well suited for use in mooring applications. This includes nylon, High modulus polyethylene (HMPE), aramid, and others. Nylon is highly elastic and may thus be well suited in shallow water locations where polyester ropes result in too high stiffness.

3.5.4 Buoys and Clump Weights

Buoys and clump weights are components used to change or apply geometric stiffness to the mooring system. By adding buoys to the mooring system, the weight needed to be supported by the floating structure is reduced. The buoy can also provide vertical clearance between the mooring line and other equipment in the water column such as other mooring lines, pipelines and subsea equipment. However, due to the need for extra connectors, which may lead to weak points in the line, they are rarely used in permanent mooring systems [16]. The clump weights may be fitted on ground chains to improve mooring performance, in terms of reducing the vessel offset. The extra weight increases the restoring force of the mooring system due to the larger weight that needs to be lifted by the vessel. Clump weights are typically mounted near the TDP of the mooring line.

3.5.5 Connectors

Connectors are used to connect mooring line segments with another or to other types of equipment. For permanent mooring systems, the requirements for the robustness of these connectors are much higher and should be manufactured with the same level of quality as the offshore mooring chain. Commonly used connectors for permanent mooring systems are of the type D-shackles and H-links [16], as illustrated in Figure 3.13.

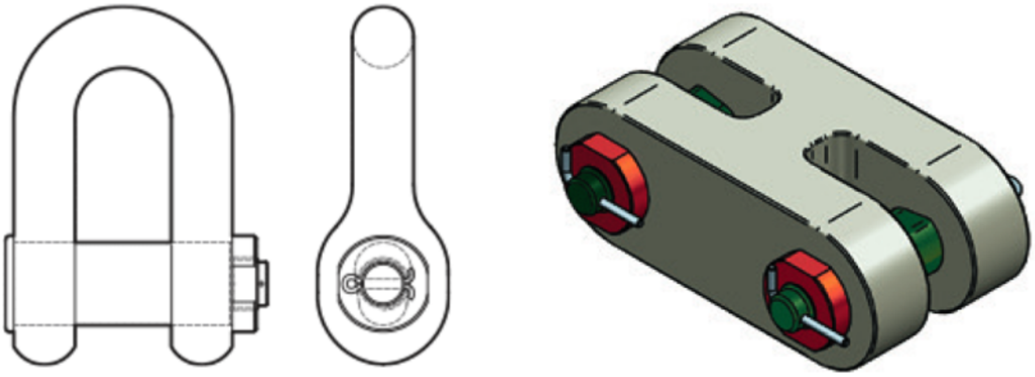

Figure 3.13: Illustration of a D-shackle (left) and an H-link (right) [25].

3.5.6 Anchors

There exists a number of anchoring solutions suitable for the use in station keeping of FWTs. The decision on which anchor type to use is dependent on the mooring configuration, seabed soil conditions, and holding capacity requirement. Applicable anchoring systems are [16]:

- Drag embedment anchor
- Vertically loaded anchor
- Gravity installed anchor, such as torpedo anchor
- Suction pile.

For mooring systems of the catenary configuration, the drag embedment anchor is typically used due to a lower cost. For systems of a taut-leg configuration, the remaining anchors on the list may be used. The suction pile, however, has a high resistance against vertical loads and is well suited in a farm configuration where multiple mooring lines share the same anchor. A brief description of the listed anchoring systems is provided in the following sections.

Drag embedment anchor

The drag embedment anchors are inserted into the seabed by dragging it along the seabed with wire rope or chain until the anchor is partly or fully penetrated into the seabed. Drag embedment anchors were originally used for mobile mooring operations but have been developed extensively such that they offer a much higher holding capacity. The anchors are considered to be easy to install, making them less expensive, and have proven performance. However, the anchors do not have the ability to be installed with high precision and have minimal capacity against vertical loads and are therefore restricted to catenary systems. Typical configurations of drag embedment anchors are given in Figure 3.14.

Figure 3.14: Typical drag embedment anchors [16].

Vertically loaded anchors

Vertically loaded anchors are an enhancement of the drag embedment anchors to ensure a higher pullout resistance in soft clay. The installation method is similar to the one used for drag embedment anchors but they penetrate much deeper into the seabed. The anchors have typically two modes; an installation mode and a normal loading mode. The installation mode allows for the anchor to start to embed into the seabed. When a predetermined installation load is reached a shear pin is ruptured, and thus, triggering the anchor into the normal vertical loading mode. The modes are described in Figure 3.15. The anchors can hold both vertical and horizontal loads.

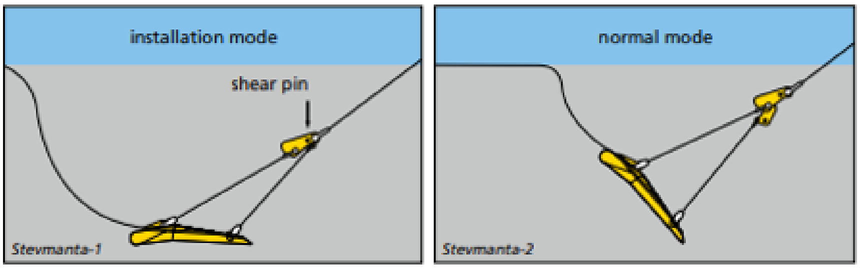

Figure 3.15: Operating modes of the vertically loaded anchors [26]

Gravity installed anchors - Torpedo anchor

Gravity installed anchors, also known as drop anchors, are installed by dropping them from just below the sea surface. The kinetic energy the anchor obtains from free-falling through the water column is what drives the anchors into the seabed. This type of installation method significantly reduces the installation time and does not require a vessel with high pulling capacity. The anchors are normally installed in soft to medium clay conditions and have a high vertical and horizontal holding capacity due to the relative deep embedment of the anchor. Again, the precision of the anchor placement is the main drawback to this type of anchor. Figure 3.16 shows a typical configuration of torpedo anchors.

Figure 3.16: Torpedo anchors on the deck of an anchor handling vessel [27].

Suction pile anchors

Suction pile anchors are large cylindrical piles with a diameter in the range of 4 to 6 m. Suction anchors are installed partly by self-weight and are further driven into the seabed by suction until desired installation depth is reached. The suction is applied at a valve in the top cap of the anchor, this suction increases the differential pressure and the anchor is pushed down by the surrounding water. This process is illustrated in Figure 3.17. The anchors have a high placement accuracy and a high vertical load capacity and are well suited for anchoring multiple mooring lines. However, the installation is time demeaning and more expensive.

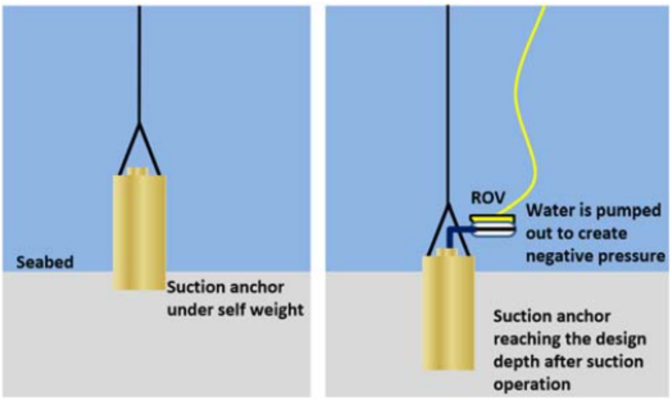

Figure 3.17: Mechanism of pile penetration by suction pressure[16].

4 Applied Theory

The following sections will describe the fundamental theory needed to understand the behaviour of FWTs and what forces the mooring systems of such structures need to withstand. The environmental loads that act on a FWT is first presented, followed by rules and regulations for mooring design. Further, the extreme distribution is described followed by a description of the time-domain analysis. Finlay, two instability phenomena for FWTs are presented and described.

4.1 Environmental Loads

Moored floating structures in open waters encounter environmental loads from waves, wind, and current, as shown in Figure 4.1. Unique for wind turbines is the additional contribution from aerodynamic forces resulting in large mean loads. The combined loading from these forces will excite the floating structure to move in its degrees of freedom. These floater motions at the top end of the mooring line are the governing excitation mechanism for mooring line loading.

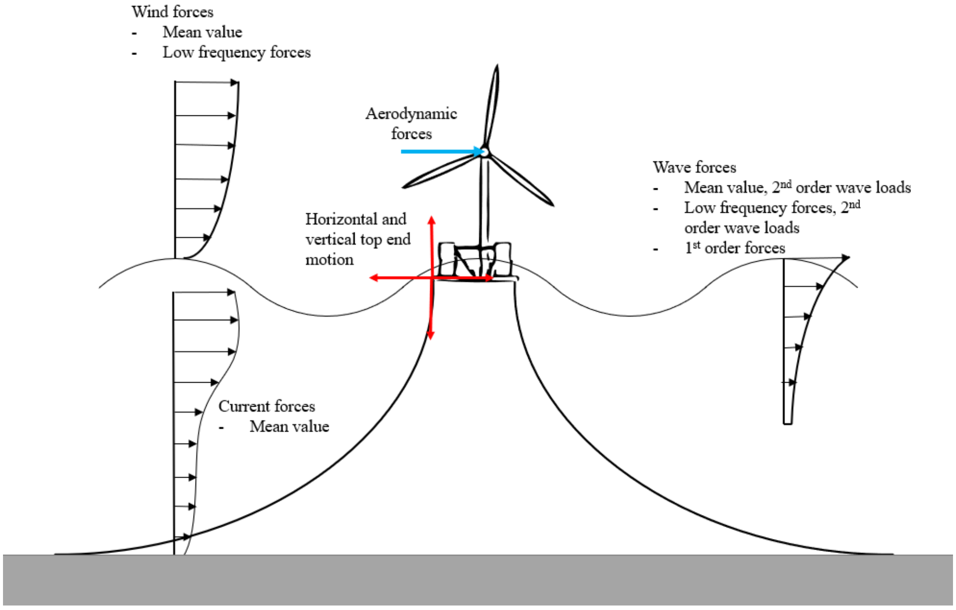

Figure 4.1: Loading mechanisms acting on a moored FWT.

4.1.1 Excitation regimes

The environmental loads acting on the floating structure that is of importance for mooring system design can be classified in the following manner according to their excitation regimes:

- **Mean loads**, this is mean current, wind, and mean wave drift forces that are constant in magnitude during the period of interest. The mean loads from the environmental conditions and the restoring forces from the mooring system will impose a new position of static equilibrium on the system. It is hence the mean loads acting on the systems that give an offset from the original position of the system. The thrust force generated by the turbine will also act as a mean load contribution.
- **Wave Frequency (WF)**, this is loads with a cyclic loading ranging from periods of 5 to 30 seconds. These loads contribute to the wave frequency motions of the floating structure which is transferred to the top end of the mooring line and results in cyclic tension of the mooring line. This cyclic tension contributes to the maximum tension experienced by the mooring line and to the accumulation of fatigue damage.

- **Low Frequency (LF)**, wave drift forces and wind gusts typically give a cyclic loading in the low-frequency regime. Normal loading periods for such loads are from 60 to 200 seconds. Typical resonance periods for FWTs in the horizontal plane are often close to 100 seconds. It is hence of great importance to consider contributions from the low-frequency loads when designing a mooring system to avoid excitation of these resonance modes.

The following sections will further describe the loading mechanisms and the methods used in the estimation of the relevant forces.

4.2 Wave Excitation Forces

Contributions from wave forces that are important when assessing a mooring system may be split into two main categories:

- First-order forces that oscillate with the wave frequencies
- Second-order mean and slowly varying wave drift forces

4.2.1 First-Order Wave Loads

The largest wave loads acting on offshore structures are the first-order forces that act at the same frequency as the waves, causing WF motions of the structure. The forces are called first-order due to the inclusion of only first-order terms in the solution of the boundary value problem for the system. The occurrence of these forces can be split into two parts. One from the undisturbed pressure field in the waves, known as the Froude-Kirloff force, and one due to disturbance of the pressure field in the wave due to the presence of the structure, called diffraction forces [18]. The wave excitation forces acting in each degree of freedom of the structure can thus be obtained through the linear dynamic pressure due to waves. This is multiplied with the structure normal for each degree of freedom and integrated over the mean wetted structure surface S_0, as shown in Equation 4.1:

$$q_{wa}^{(1)} = \int_{S_0} p_d n_j dS = \rho \int_{S_0} \frac{\partial \varphi_0}{\partial t} n_j dS + \rho \int_{S_0} \frac{\partial \varphi_7}{\partial t} n_j dS \tag{4.1}$$

where p_d is the linear dynamic pressure, n_j is the structure normal for each degree of freedom, ρ is the density of the fluid, φ_0 is the incident wave velocity potential, and φ_7 is the diffraction velocity potential. For large volume structures, this problem is solved numerically by panel codes such as WAMIT.

For slender structures, meaning that the wavelength is at least 5 times larger than the characteristic diameter of the structure, the wave forces may be well predicted by the Morison equation. The Morison equation gives the force per unit length as [28]:

$$F_m(t) = \rho \frac{\pi}{4} \left(C_f + C_a\right) a_w(t) + \frac{1}{2} \rho D C_D u_w(t) \left|u_w(t)\right| \tag{4.2}$$

where F_m is the force per unit length, D is the cross-section diameter, $u_w(t)$ and $a_w(t)$ are the velocity and acceleration of the undisturbed fluid at the mid-point of the cross-section. C_m and C_D are the mass and drag coefficients where C_m can be written as $C_m = C_f + C_a$ with C_f being the Froude-Kriloff coefficient and C_a the added mass coefficient. The first term of Equation 4.2 is called the inertia term while the second is called the drag term. The inertia term consists of two contributors, the Froude-Kriloff force and the diffraction force, while the drag term represents the drag force due to flow separation around the structure. The dominating contributor in Equation 4.2 depends on the wave properties relative to the structure, Figure 4.2 illustrates the different wave force regimes. In Figure 4.2, H is the wave height and λ is the wavelength.

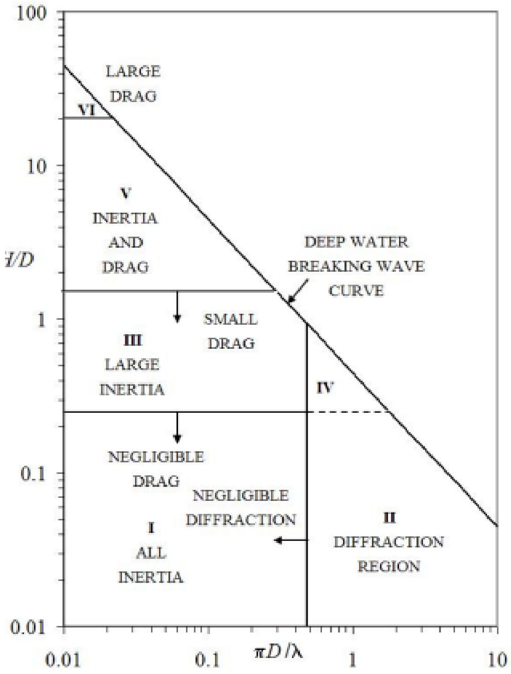

Figure 4.2: Different wave force regimes [29].

For cases when considering a floating structure the relative velocity and acceleration between the structure and fluid must be used, thus Equation 4.2 can be rewritten as:

$$F_m(t) = \rho\frac{\pi}{4}\left(C_f a_w(t) + C_a a_r(t)\right) + \frac{1}{2}\rho D C_D u_r(t)\left|u_r(t)\right| \tag{4.3}$$

where u_r and a_r is the relative velocity and acceleration respectively, expressed as:

$$u_r = u_w - u_b \tag{4.4}$$

$$a_r = a_w - a_b \tag{4.5}$$

where u_b and a_b is the body velocity and acceleration respectively. When the relative velocity is used the drag term will be in phase with the velocity of the structure which will give a damping contribution.

The mass and drag coefficients are determined empirically and depend on several parameters like the Reynolds number, Keulegan-Carpenter number, a relative current number and surface roughness ratio [18]. Mass and drag coefficients for numerous cross-sections are provided in DNVGL-RP-C205 [29].

4.2.2 Second-Order Wave Loads

When considering the second-order problem, all terms in the solution of the boundary value problem that is either linear or proportional to the square of the wave amplitude are kept. When this is done the solution of the problem results in mean forces and forces oscillating with difference frequency or a sum frequency in addition to the linear solution [18]. For moored systems, the mean and slowly-varying wave loads (difference frequency loads) are of great importance due to the mean offset and excitement of resonance motions in the horizontal plane of the floater. The mean and slowly varying lads are related to each other, so if there are no mean wave loads there are no slowly varying loads. The slowly varying forces are caused by time-varying mean loads imposed by wave groups of higher amplitude. The mean drift loads are due to the body's ability to generate waves, and the occurrence of mean loads can be described by Figure 4.3.

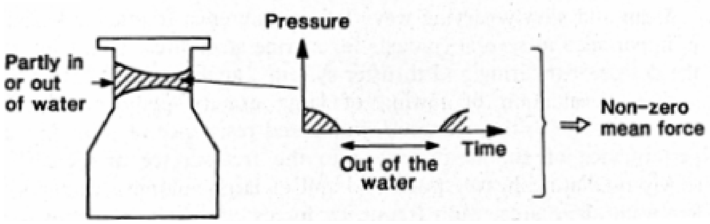

Figure 4.3: Horizontal mean wave force contribution due to pressure forces on the free-surface zone of a structure [18].

Some of the structure in Figure 4.3 is partly in the water and partly out of the water. This results in a non-zero mean pressure at a point along this surface zone which in turn results in a non-zero mean force acting on the structure. It becomes clear when looking at Figure 4.3 that for long waves the contribution to mean loads becomes small.

Slowly varying forces can cause resonance oscillations and are large when the mean drift loads are large. It is the difference in frequency between two wave components, $\omega_i - \omega_j$, that contributes to the slowly varying forces. Second-order wave forces are in general small, and thus, the most important contribution is close to resonance [29], which for surge and sway motions are when $\omega_i - \omega_j$ is small. This gives the opportunity to calculate the slowly varying forces through Newman's approximation which only considers the diagonal terms in the second-order transfer functions.

4.2.3 The Statistical Description of Waves - Wave Spectra

For the description of an irregular sea linear wave theory is used where the surface elevation due to long-crested waves propagating through the point $x = 0$ on the x-axis can be described as the sum of a large number of wave components as [18]:

$$\zeta(t) = \sum_{j=1}^{N} \zeta_{Aj} \cos\left(\omega_j + \varepsilon_j\right) \tag{4.6}$$

where ζ_{Aj}, ω_j, and ε_j are respectively the wave amplitude, circular frequency, and random phase angle of wave component j. The phase angle is uniformly distributed between 0 and 2π. The wave amplitude is assumed to be a stationary, Gaussian distribution with zero mean and ergodic process. The energy in wave component j can be written as:

$$E_{w,j} = \frac{1}{2}\rho g \zeta_{Aj}^2 \tag{4.7}$$

and the energy for in a sea state

$$\frac{E_w}{\rho g} = \sum_{j=1}^{N} \frac{1}{2}\zeta_{Aj}^2\left(\omega_j\right) \tag{4.8}$$

where ρ is the fluid density and g is the acceleration of gravity. This energy is what the wave spectra describe, where the area inside a small frequency interval $\Delta\omega$ is equal to the energy of all the wave components within this interval [30] as shown:

$$\frac{1}{2}\zeta_{Aj}^2 = S\left(\omega_j\right)\Delta\omega \tag{4.9}$$

where $S(\omega_j)$ is the spectral density of the wave elevation $\zeta(t)$. Thus, the wave elevation, $\zeta(t)$, at a point in space as a function of time can be described through the wave spectra, $S(\omega_j)$, as:

$$\zeta(t) = \sum_{j=1}^{N} \sqrt{2S(\omega_j)\,\Delta\omega} \cos(\omega_j t + \varepsilon_j) \tag{4.10}$$

The spectra contain all the necessary information about the statistical properties of the wave elevation. Typical input parameters for the generation of the wave spectra is the significant wave height and spectral peak period. A commonly used wave spectrum, the JONSWAP spectrum, is illustrated in Figure 4.4, γ is a non-dimensional peak shape parameter.

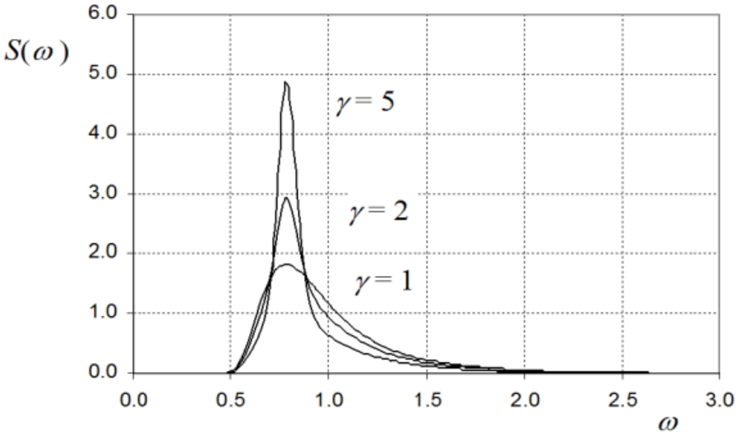

Figure 4.4: JONSWAP spectrum for $H_s = 4$ m, $T_p = 8$ s [29].

4.3 The Wind Environment

The wind is an important environmental load, especially for FWTs due to the exposure to large aerodynamic loads. The wind also has an influence on the operation of the wind turbine where different wind regimes alter how the turbine operates and consequently change the aerodynamic forces from the turbine.

The wind can generally be divided into two parts, one mean component, $\overline{V}(z)$, and one fluctuating gust component, $v(z,t)$, as shown in Equation 4.11. The mean component is only dependent on the height above the still water level and is commonly represented by the 10-minute mean wind speed V_{10} at a height of 10 m. The gust component varies with both the height and time and can be represented as the standard deviation, σ_V, of the wind speed at a height of 10 m. This variability of the wind speed around the mean wind speed is better known as turbulence.

$$V(z,t) = \overline{V}(z) + v(z,t) \tag{4.11}$$

The turbulence of a wind condition is commonly measured by turbulence intensity. It is defined as the ratio of the standard of the wind speed to the mean wind, as shown in Equation 4.12 [31]:

$$TI = \frac{\sigma_V}{V_{10}} \tag{4.12}$$

Turbulence intensity is generally in the range of 0.1 to 0.4 with the highest values occurring at lower wind speeds.

The wind speed profile used to represent the variation of the mean wind speed with height above the still water level is the power-law model given in Equation 4.13 [32]:

$$\overline{V}(z) = \bar{v}_r \left(\frac{z}{z_r} \right)^{\beta} \tag{4.13}$$

where z is the height above the water plane, z_r is the reference height which is normally 10 m, $\bar{v}_r$ is the average velocity at the reference height, and β is the power-law exponent which is dependent on the terrain roughens. Figure 4.5 illustrates how a typical wind profile may vary in space and time with the inclusion of turbulence. Further, the figure clearly shows how the mean wind speed increases with height.

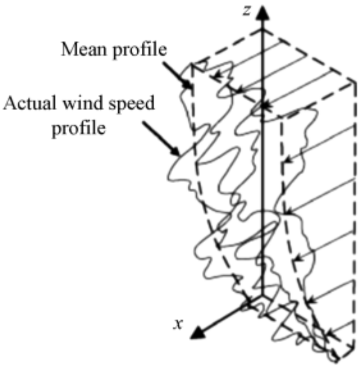

Figure 4.5: Experimental wind speed profile [32].

4.3.1 Turbulence Spectra and Coherence Model

During a time domain analysis the short-term stationary wind conditions may be described by the power spectral density of the wind speed, known as a wind spectrum. Wind conditions considered in this work are IEC 61400-3 compliant and are represented through the Kaimal wind spectrum given in non-dimensional form as [33]:

$$\frac{f S_k(f)}{\sigma_k^2} = \frac{4 f L_k / V_{10}}{(1 + 6 f L_k / V_{10}\ )^{5/3}} \tag{4.14}$$

where f denotes frequency in hertz and L_k is an integral length scale parameter where the index k represents the velocity component in X-, Y-, and Z-direction written as u, v, and w respectively. L_k and the corresponding standard deviation is specified in IEC 61400-1 as shown in table 4.1.

Table 4.1: Turbulence spectral parameters for the Kaimal model.

	Velocity component index, k		
	u	v	w
Standard deviation, σ_k	σ_u	$0.8\sigma_u$	$0.5\sigma_u$
Integral scale, L_k	$8.1\Lambda_u$	$2.7\Lambda_u$	$0.66\Lambda_u$

Λ_u is the longitudinal scale parameter which at hub height z is given by:

$$\Lambda_u = \begin{cases} 0.7z \text{ for } z < 60 \text{ m} \\ 42 \text{ m for } z \geq 60 \text{ m} \end{cases}$$

The turbulence spectra describe the temporal variation of each wind component at any given point. However, as the wind turbine blade rotates through space, the wind speed variations it experiences are not well described by the single point spectra. Thus, the spectral description of turbulence is extended to include the cross-correlations between turbulent fluctuations at points separated laterally and vertically[34]. This is clearly an important contribution since the blade will experience this spatial variation as it rotates through space. The correlations will decrease as the distance separating two points increase and for high-frequency variations in the turbulence. The correlations are described by so-called coherence functions which describe the correlations as a function of frequency and separation. An exponential coherence model is specified in IEC 61400-1 to be used in conjunction with the Kaimal spectrum as shown in Equation 4.15:

$$\mathrm{Coh}(r,f) = \exp\left[-12\left((fr/V_{10})^2 + (0,12r/L_{\mathrm{u}})^2\right)^{0,5}\right] \tag{4.15}$$

Where r is the magnitude of the projection of the separation vector between the two points on a plane normal to the average wind direction.

4.3.2 TurbSim

Wind conditions in the analysis are described by a TurbSim fluctuating three-component wind time series generated using wind spectrum and coherence models as described in the preceding sections. The theory presented regarding the TurbSim program is based on the *TurbSim User's Guide: Version 1.50* [35].

TurbSim is a stochastic, full-field, turbulent-wind simulator. It uses a statistical model to numerically simulate time series of three-component wind-speed vectors at points specified in a two-dimensional vertical rectangular grid fixed in space. Time-series as generated by an inverse Fourier transform of the spectra of velocity components and spatial coherence.

Wind components are defined in two separate coordinate systems as shown in Figure 4.6. Wind speeds are calculated in a coordinate system aligned with the direction of the mean velocity vector at each point in space. The velocities are later transformed to the inertial reference frame coordinate system and written to output files.

Inertial Reference Frame	
U	Along positive *X* (nominally downwind)
V	Along positive *Y* (to the left when looking along *X*)
W	Up, along positive *Z* (opposite gravity)
Aligned with the Mean Wind	
u	Streamwise (longitudinal)
v	Transverse (crosswise)
w	Vertical

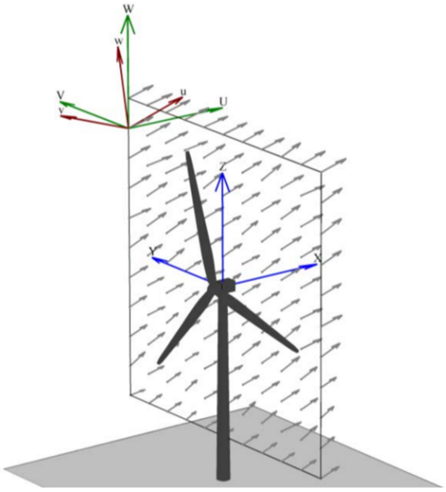

Figure 4.6: Definitions of TurbSim wind component coordinate systems and Coordinates of a TurbSim wind field with 15°horizontal and 8°vertical mean flow angles [35].

4.3.3 Wind Force

The wind force acting on the structure is calculated based on the instantaneous wind and structure velocities, according to the following formula:

$$q_{wj} = C_{wj}(\alpha)v_r^2 \tag{4.16}$$

where j is the degree of freedom, C_w is the wind force coefficient for the instantaneous relative direction, v_r is the relative wind speed between the structure and wind given as $v_r = v - u_b$, where v is the wind velocity. α is the relative velocity direction in a local coordinate system. The wind force coefficient can be written as:

$$C_w = \frac{1}{2}\rho_{air}C_D D \tag{4.17}$$

where ρ_{air} is the density of air. The drag coefficient C_D can again be found in DNVGL-RP-C205 [29] for the relevant cross-section.

4.4 Current force

The force contributions form currents are computed using the current velocity at the surface [36]. The current drag forces are normally expressed by:

$$q_{cu}^{(j)}(\alpha, t) = +C_2^{(j)}(\alpha)|u_{c,r}(t)|^2 \tag{4.18}$$

where $u_{c,r}$ is the relative velocity between low-frequency body velocity and current velocity given as $u_{c,r} = u_c - u_b$ where u_c is the current velocity. C_2 is the quadratic current force coefficient. The current coefficient is calculated in a similar manner as for wind, but with the density of water used instead.

4.5 Aerodynamics of Wind Turbines

A loading mechanism that is unique for FWTs is the loading due to aerodynamic forces generated by the wind turbine. The contribution from aerodynamic forces to the total loading of the FWT may be quite substantial and even dominating at certain wind speeds. Hence, a fundamental understanding of the aerodynamics of wind turbines is crucial for understanding the behaviour of such systems. The following sections will cover central concepts on which the Blade Element/Momentum (BEM) theory is based. BEM-theory is the most common method implemented in tools for the calculation of aerodynamic forces.

4.5.1 1-D Momentum Theory for an Ideal Wind Turbine

Before deriving the theory for the BEM method, it is beneficial to start off with a simple one-dimensional model for an ideal rotor as illustrated in Figure 4.7. The explanations herein closely follow the presentation in [31].

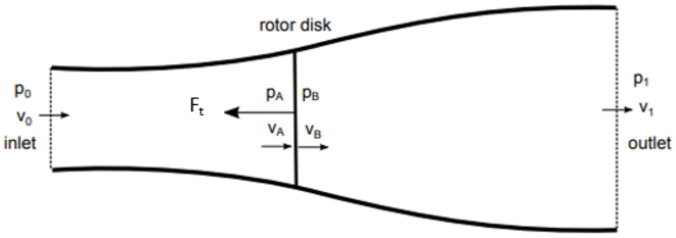

Figure 4.7: One-dimensional actuator disk rotor model [37].

Considering the wind coming in through the control volume at the inlet with a velocity v_0. The only way to extract energy from this wind is to slow it down such that the velocity of the wind behind the rotor is lower than in front of the rotor. Thus, a force needs to be applied to the wind, this force is called the thrust force, F_t. The thrust force acts on the wind and thereby changes its kinetic energy. This change in kinetic energy gives the opportunity to extract power from the wind.

In Figure 4.7 there are two control volumes: One from the inlet to side A of the rotor disc, and one from side B of the rotor disc to the outlet. The flow can not cross the stream tube boundaries, i.e. the flow only travels from the inlet and out through the outlet passing the rotor disc on the way. At the inlet, the pressure is p_0 and the velocity is v_0, corresponding quantities are shown for the other locations in the model.

The following assumptions are made in the 1-D Momentum Theory:

- Homogeneous, incompressible, steady-state fluid flow
- No frictional drag
- The disc has an infinite number of blades
- Uniform thrust over the disc or rotor area
- A non-rotating wake
- The static pressure far upstream and far downstream of the rotor is equal to the undisturbed ambient static pressure

By establishing the conservation of linear momentum to the control volume, and using the Bernoulli equation on each side of the rotor disc one can establish two expressions for the thrust force, as shown:

$$F_t = \dot{m}\left(v_0 - v_1\right) \tag{4.19}$$

$$F_t = \frac{1}{2}\rho_{air} A_r \left(v_0^2 - v_1^2\right) \tag{4.20}$$

where $\dot{m}$ is the mass flow rate of air through the system, ρ_{air} is the air density, and A_r is the rotor disk area. Equation 4.19 is from the conservation of momentum and Equation 4.20 is from the Bernoulli equation. Setting the equations for the thrust force equal to each other gives the velocity at the rotor disc as:

$$v_A = \frac{1}{2}\left(v_0 + v_1\right) \tag{4.21}$$

This relation can be used to describe a quantity called the axial induction factor, indicating the relation between the velocity at the rotor disc and the incoming velocity as:

$$a = \frac{v_0 - v_A}{v_0} \tag{4.22}$$

The extracted power can then be expressed as:

$$P = \frac{1}{2}\rho_{air} A_r v_0^3 4a(1-a)^2 \tag{4.23}$$

and the corresponding power (C_P) and thrust (C_T) coefficients can be written as:

$$C_P = \frac{P}{\frac{1}{2}\rho_{air} v_0^3 A_r} = 4a(1-a)^2 \tag{4.24}$$

$$C_T = \frac{F_t}{\frac{1}{2}\rho_{air} v_0^2 A_r} \tag{4.25}$$

The maximum power that can be extracted from the wind is found by setting the derivative of the power coefficient equal to zero. This gives a maximum value for the axial induction factor equal to $\frac{1}{3}$, inserting this value back into Equation 4.24 gives the maximum power coefficient known as the Betz limit: $C_{Pmax} = \frac{16}{27}$.

4.5.2 Wake Rotation

So far, the equations for the 1-D momentum theory have disregarded the effects from the rotation of the wake behind the rotor. In practice, the torque exerted by the blades causes the airflow to rotate. The turbine thereby uses some energy to put the wake into motion, and thus, the turbine cannot achieve the hypothetical Betz-limit. The angular velocity of the rotor and the angular velocity imparted to the free stream are denoted as Ω and ω_{wake}, respectively. These quantities are used to describe a new variable called the angular induction factor, written as:

$$a' = \frac{\omega_{wake}}{2\Omega} \tag{4.26}$$

From the conservation of angular momentum the power coefficient for the full rotor can be written as:

$$C_P = \frac{8}{\lambda_{TSR}^2} \int_0^{\lambda_{TSR}} a'(1-a)\lambda_r^3 d\lambda_r \tag{4.27}$$

where λ is the tip speed ratio, and λ_r is the local speed ratio, given as:

$$\lambda_{TSR} = \frac{\Omega R}{v_0} \tag{4.28}$$

$$\lambda_r = \frac{\lambda_{TSR} r}{R} \tag{4.29}$$

where R is the radius of the rotor and r is the local radius at a location in the rotor disc. The tip speed ratio gives the ratio between the speed of the tip of the blade and the incoming velocity. Figure 4.8 shows the power coefficient for different values of the tip speed ratio. The figure shows that for large numbers of the tip speed ratio the power coefficient approaches the Betz limit, e.g. the power loss due to wake rotation becomes smaller for larger values of the tip speed ratio.

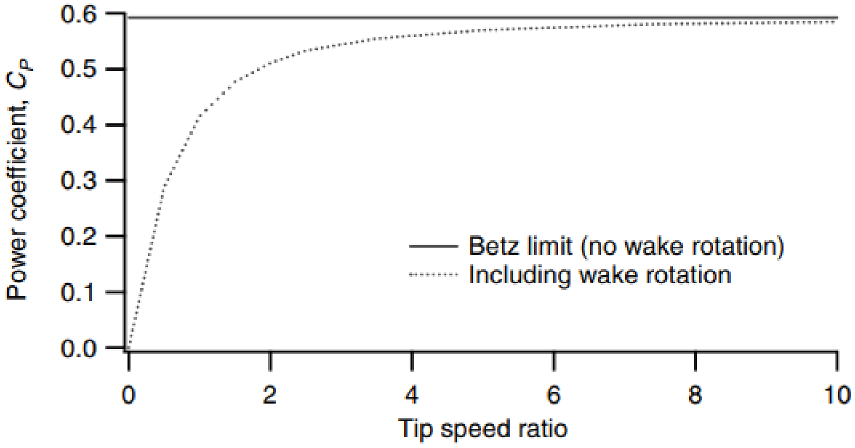

Figure 4.8: Theoretical maximum power coefficient as a function of tip speed ratio, λ, for an ideal wind turbine, with and without wake rotation [31].

The 1-D momentum theory with wake rotation results in the following expressions for the thrust force and torque acting on the rotor:

$$\mathrm{d}F_t = 4a(1-a)\frac{1}{2}\rho_{air} v_o^2 2\pi r \ \mathrm{d}r \tag{4.30}$$

$$\mathrm{d}Q_a = 4a'(1-a)\frac{1}{2}\rho_{air} v_0 \Omega r^2 2\pi r \ \mathrm{d}r \tag{4.31}$$

4.5.3 Blade Element/Momentum Theory

The BEM-theory is the result of combining the 1-D momentum theory with blade element theory where lift, F_{lift}, and drag forces, F_{drag}, acting on blade sections are defined through airfoil theory. Using the derived theory and looking at an airfoil section, as shown in Figure 4.9, the thrust force can be found as a force acting normal to the rotor plane, p_N, and the torque as a force acting tangential to the rotor plane, p_T.

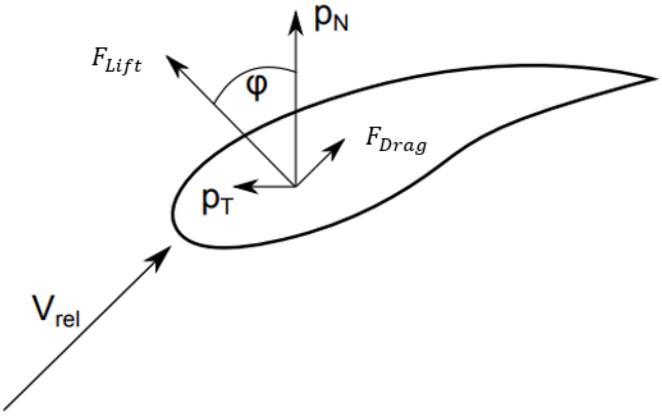

Figure 4.9: Airfoil section in the rotor plane [37].

The inflow velocity at the airfoil, V_{rel}, includes contributions from the incoming wind, the rotational velocity of the blade, the induced axial velocity, and the induced tangential velocity. The angle, φ, is from the angle of attack and the blade pitch angle. From Figure 4.9, the following relations for the thrust and torque can be derived:

$$\mathrm{d}F_t = Bp_N\mathrm{d}r = B(F_{lift}cos(\varphi) + F_{drag}sin(\varphi))\mathrm{d}r \tag{4.32}$$

$$\mathrm{d}Q_a = BrP_T\mathrm{d}r = Br(F_{lift}sin(\varphi) + F_{drag}cos(\varphi))\mathrm{d}r \tag{4.33}$$

where B is the number of blades. Using the expressions for thrust and torque derived from momentum theory and airfoil theory and setting the respective expressions equal to each other gives the following expressions for the axial and angular induction factor:

$$a = \frac{1}{\frac{4\sin^2\varphi}{\sigma C_n} + 1} \tag{4.34}$$

$$a' = \frac{1}{\frac{4\sin\phi\cos\varphi}{\sigma C_t} + 1} \tag{4.35}$$

where C_n and C_t is the normal and tangential coefficient for the lift and drag coefficient of the airfoil section, and $\sigma = \frac{Bc}{2\varphi r}$ is the solidity ratio of the rotor where c is the chord length of the airfoil. The BEM theory is solved through an initial guess of the values for a and a' and further iteration until convergence is reached.

The BEM theory uses important corrections to account for the simplifications done when deriving the theory, these are:

Prandtl correction: Describes the tip loss effect, due to the air flowing around the tip of the blade and not over.

Glauert correction: Accounts for inductions factors above 0.5 where the BEM theory is not valid.

Dynamic inflow/wake: Accounts for the time lag in the induced velocities due to the shedding and downstream convection of vorticity.

Dynamic stall: Accounts for sudden detachment and re-attachment of flow over the airfoils, causing the drag and lift coefficient to not follow the static values.

4.5.4 Wind Turbine Control

The wind turbine control system plays an important role in the response of the wind turbine and has the purpose to manage a safe and automatic operation of the wind turbine. Modern wind turbines operating today commonly use an operating strategy called "Variable Speed, Variable Pitch" (VSVP). This simply means that the turbine can rotate at different speeds and the blades pitch angle can be controlled. Typical behaviour for a wind turbine following this operating strategy is illustrated in Figure 4.10. In this figure, the mean rotor speed, generator torque, generator power, and blade pitch angle are shown as a function of mean wind speed. Furthermore, the figure defines four regions in the operation strategy. In regions 1 and 4, there is no power extraction from the wind since the wind speed is below the cut-in speed in region 1 and above the cut-out speed in region 4. In region 2, the wind speed is in between cut-in and rated, here the aim is to extract as much power as possible from the wind. This is done by keeping a constant pitch angle and allowing for an increasing rotor speed. As the wind speed goes beyond the rated wind speed the wind turbine controller changes its objective. In this region the aim is to keep the power production at the rated level while minimising the loads acting on the turbine, this is done by adjusting the blades' pitch angle.

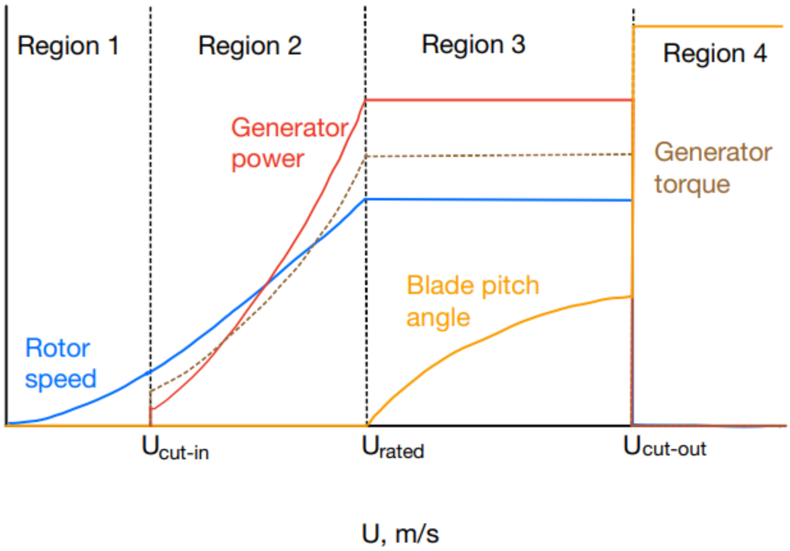

Figure 4.10: Typical behaviour for a VSVP type controller [38].

4.6 Rules and Regulations

This section will cover rules and regulations related to the station keeping systems for floating wind turbine structures. The main design requirements presented herein are from Sections 8 and 9 in DNVGL-ST-0119 [6] with additional guidance from DNV-OS-E301 [39]. The mooring systems covered in this standard are of the type catenary and taut mooring systems. Further, the standard specifies that all components in the station keeping system of the floating support structure shall be designed to consequence class 1. This requirement refers to station keeping systems that have redundancy. Systems without redundancy shall be designed to consequence class 2.

Consequence classes 1 and 2 are defined as:

- **Consequence class 1:** Where failure is unlikely to lead to unacceptable consequences such as loss of life, collision with an adjacent structure, and environmental impacts.
- **Consequence class 2:** Where failure may well lead to unacceptable consequences of these types.

4.6.1 Limit States

A limit state is defined as a condition beyond which a structure or structural component will no longer satisfy the design requirements. A mooring system shall be analysed with respect to three limit states defined as:

- **Ultimate Limit State (ULS)**: The individual mooring lines shall have sufficient strength to withstand the loads resulting from extreme environmental actions.
- **Accidental Limit State (ALS)**: The mooring system shall not lose its integrity in the event of failure of one mooring line.
- **Fatigue Limit State (FLS)**: The mooring system shall not experience fatigue failure as a consequence of cyclic loading during its design life.

4.6.2 Ultimate Loads and Accidental Cases

The design tension in the mooring line during governing ULS-cases is defined as the sum of two factored characteristic tension components denoted as $T_{c,mean}$ and $T_{c,dyn}$ as shown in Equation 4.36:

$$T_d = \gamma_{mean} \cdot T_{c,mean} + \gamma_{dyn} \cdot T_{c,dyn} \tag{4.36}$$

Where $T_{c,mean}$ is the characteristic mean tension, $T_{c,dyn}$ is the characteristic dynamic tension, and γ_{mean} and γ_{dyn} are the respective load factors.

The characteristic mean tension consists of the mean environmental loads from wave drift, current and wind in addition to the pretension and is defined as the mean part of the 50-year value of the line tension. The characteristic dynamic tension is defined as the dynamic part of the 50-year value of the line tension. The contribution to the characteristic dynamic tension is oscillatory LF and WF effects.

The characteristic mean and dynamic tension shall be determined through investigation of several trial sea states along the 50-year contour in (H_s, T_p, U_{10})-space. The values of $T_{c,mean}$ and $T_{c,dyn}$ are then selected from the specific sea state that yielded the largest line tension response along the 50-year contour. During this investigation, the assumption of direction-independent environmental loading acting in the direction which is most unfavourable for the mooring line is used. This assumption gives a conservatism for the largest line tension, and thus, the largest line tension response along the 50-year contour can be considered as a direct estimate of the 50-year value for the line tension without any need for multiplication with an inflation factor.

For a time-domain analysis the following apply for identification of the variables in Equation 4.36:

$T_{c,mean}$ = mean tension of the time series
$T_{c,dyn}$ = $T_{MPM} - T_{c,mean}$
T_{MPM} = most probable max of the time series

Figure 4.11 illustrates a typical time series of the line tension from a time-domain analysis.

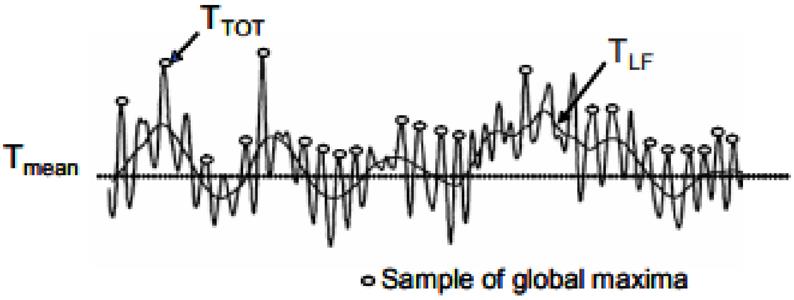

Figure 4.11: Time series of mooring line tension [39].

The global maxima in the time series are assumed to be independent stochastic variables, and can thus be well modelled by the Weibull distribution. A 3 parameter Weibull distribution is commonly used.

The MPM-value shall then be estimated through the extreme value distribution for the line tension, as shown Figure 4.12

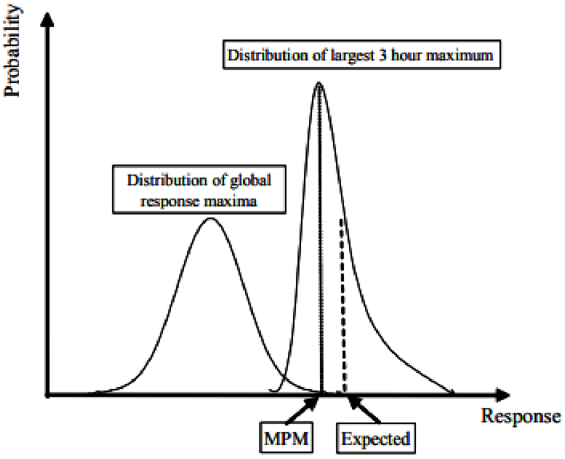

Figure 4.12: Illustration of the distribution of global maxima and the extreme value distribution [39].

The extreme value distribution is known to take the form of a Gumbel distribution for an increasing number of maxima. The MPM-value corresponds to the value with a 63% probability of exceedance. For time-domain analyses, it is recommended to simulate 10-20 realisations of duration 3 hours to get sufficient data for adequate statistics.

For the ALS simulations, one mooring line is assumed to have failed and is thus removed from the analysis. Several lines shall be removed one at a time for cases where all mooring lines are of an equal configuration to identify the line failure leading to the highest line tension in the remaining lines. The response analysis of the platform motions and mooring line tension is carried out exactly as for the ULS-cases. The same environmental conditions are used as for the ULS-cases, thus, the load factors in the ALS case are of a lower magnitude to account for the low probability of occurrence for weather of this severity together with a random initial failure.

Load factors for the two consequence classes are given in Table 4.2 for both the ULS and ALS conditions.

Table 4.2: Load factor requirements for the design of mooring lines.

Limit state	Load factor	Consequence class	
		1	2
ULS	γ_{mean}	1.3	1.5
ULS	γ_{dyn}	1.75	2.2
ALS	γ_{mean}	1.00	1.00
ALS	γ_{dyn}	1.10	1.25

4.6.3 Characteristic Capacity

The mooring lines are built up of several identical elements. As stated, a chain line is composed of a large number of chain links, and the strength of a long line is thus expected to be lower than the average strength of the components that make up the line. This effect is captured in the definition of characteristic capacity of the mooring line, written as:

$$S_C = \mu_S \cdot (1 - COV_S \cdot (3 - 6 \cdot COV_S))\,; \mathrm{COV_S} < 0.10 \tag{4.37}$$

where μ_S is the mean value of the breaking strength of the component and COV_S is the coefficient of variation of the breaking strength of the component. This formulation can be used for mooring lines consisting of chain, steel wire rope and synthetic fibre rope.

The characteristic capacity of the body of the mooring line may be obtained through the minimum breaking strength S_{mbs} of a new component if the statistics of the breaking strength of a component are not available, this is written as:

$$S_C = 0.95 \cdot S_{mbs} \tag{4.38}$$

Due to uncertainty in the test statistics of the strength distribution, a cautious estimate of the statistically uncertain characteristic capacity shall be taken as:

$$S_C{}^* = S_C \cdot \left(1 - 2 \cdot \frac{COV_S}{n}\right) \tag{4.39}$$

where n is the number of tests and shall not be less than 5.

4.6.4 Design Criterion

After establishing the design tension and characteristic capacity of the mooring lines the design criterion is controlled. For the ULS and ALS the design criterion is defined as

$$S_C > T_d \tag{4.40}$$

S_C is to be replaced by $S_C{}^*$ when the strength distribution for the mooring line components is based on test statistics.

Equation 4.40 may conveniently be reformulated to introduce the utilization factor, UF:

$$UF = \frac{T_d}{S_C}, \qquad UF \leq 1 \tag{4.41}$$

4.6.5 Anchor Foundations

The anchor is defined as a load-bearing structure and shall be designed against geotechnical anchor failure in the ULS and ALS cases. The design force, T_d, acting on the anchor due to tension in the mooring line shall be taken as equal to the design line tension found during calculations in accordance with the description in Section 4.6.2. In the case of multiple lines being connected to one anchor, T_d shall be calculated considering contributions from all connected lines.

The design anchor resistance is given as:

$$R_d = \frac{R_c}{\gamma_m} \tag{4.42}$$

where R_c is the characteristic geotechnical anchor resistance estimated from site-specific soil data and γ_m is a soil material factor. The design criterion is then given as:

$$T_d \leq R_d \tag{4.43}$$

Values for the soil material factor to be applied in the calculation of the characteristic resistance are given in Table 4.3.

Table 4.3: Values for the soil material factor for different anchor types.

Anchor type	γ_m	
	ULS	ALS
Pile anchor	1.3	1.0
Gravity anchor	1.3	1.0
Suction anchor	1.2	1.0
Free fall anchor	1.3	1.0

4.6.6 Design Load Cases

So far it is assumed that the 50-year value of the line tension is to occur during a sea state along the 50-year environmental contour line. However, this may not be the case in the design of a FWT. This is due to the high thrust force generated by the turbine at rated wind speed due to aerodynamic loading. This may cause the largest drift and the highest loads in the mooring system. It is therefore of importance to also control such conditions in the estimation of $T_{c,mean}$ and $T_{c,dyn}$. The DNV standard for FWTs, DNVGL-ST-0119 [6], gives a Design Load Case (DLC) matrix that shall be investigated during the design of FWTs. Thus, conditions proposed in this standard shall be further investigated at later stages to determine if one of the given design load cases will be the governing ULS and ALS load cases. Further, design load cases given in DNVGL-ST-0437 [40] and IEC TS 61400-3-2 [41] are considered for the relevance in mooring design. Design load cases that are found to be of importance for mooring design are presented in Table 4.4.

Table 4.4: Additional design load cases for the mooring analysis.

Design situation	DLC	Wind condition	Waves	Wind and wave directionality	Sea currents	Water level	Other Conditions
1) Power production	1.1	NTM $V_{in} < V_{hub} < V_{out}$	NSS $H_s = E[H_s \vert V_{hub}]$	COD, UNI	NCM	MSL	
	1.6	NTM $V_{in} < V_{hub} < V_{out}$	SSS $H_s = H_{s,SSS}$	COD, UNI	NCM	NWLR	
6) Parked (standing still or idling)	6.1	EWM $V_{hub} = V_{ref}$	ESS $H_s = H_{s,50}$	MIS, MUL	ECM $U = U_{50}$	EWLR	Yaw misalignment of 8 deg Possible yaw slippage

Both standards consider load cases of similar construction. Load cases from DNVGL-ST-0437 have thus been used in Table 4.4 in order to be consistent with the terminology used in the table. The numbering of the DLCs is equal to the cases found in the standard for easier recognition of each DLC when reading the DNV standard. Explanations of abbreviations are listed in Table 4.5

Table 4.5: Abbreviations and symbols for the design load cases.

Abbreviations		Symbols	
Short form	In full	Symbol	Explanation
COD	co-directional	H_s	significant wave height
ECM	extreme current model	$H_{s,SSS}$	significant wave height of severe sea state
ESS	extreme sea state	$H_{s,50}$	50-year value of the significant wave height
EWLR	extreme water level range	U	current velocity
EWM	extreme wind speed model	U_{50}	50-year value of the current velocity
MIS	misaligned	V_{hub}	10-minute average wind speed at hub height
MSL	mean sea level	V_{in}	cut-in wind speed
MUL	multi-directional	V_{out}	cut-out wind speed
NCM	normal current model	V_{ref}	50-year value of the wind speed
NSS	normal sea state		
NTM	normal turbulence model		
NWLR	normal water level range		
SSS	severe sea state		
UNI	uni-directional		

Description of design load cases

DLC 1.1: Considers environmental conditions through the operational range of the turbine with wave conditions corresponding to the wind velocity. Predominantly the wind speeds close to or at the rated wind speed shall be investigated in this load case. Additionally, wind speeds close to the cut-out speed shall be investigated.

DLC 1.6: Considers again wind speeds through the whole operational range of the turbine. Differently, the sea state used for each wind speed shall be the corresponding severe sea state, $H_{s,SSS}$, related to that wind speed. Wind speeds around rated wind speed and the cut-out speed shall again be investigated.

DLC 6.1: Investigates the 50-year site-specific condition with the wind turbine in parked or idling condition. The 50-year contour in (H_s, T_p, U)-space shall be used to identify the combination on the contour line that yields the highest line tension. This Combination shall then be further used in the simulations. In DLC 6.1 the 50-year ESS is associated with a 50-year current value. This is, according to DNV-ST-0119, a quite conservative assumption with respect to mooring design due to the typically low correlation between current and the values of wind and waves. As a result, the recommendation is to use a 5-year value for the current in this DLC. However, if this reduction is to be used, the DLC shall also be demonstrated by using a 50-year current in combination with wind and wave conditions of 5 year return period. The combination leading to the highest tensions shall be used for design.

4.7 Extreme Value Distribution

The most probable maximum value of the extreme value distribution for the line tension is used during the design of mooring systems to establish a design tension that is controlled according to relevant rules and regulations.

The extreme value of the line tension will vary from one simulation to the next, and thus, the extreme value is a stochastic variable. The extreme value distribution is established from a large number of samples where the largest maxima from each sample are collected and are used to identify the distribution, as shown in Figure 4.13.

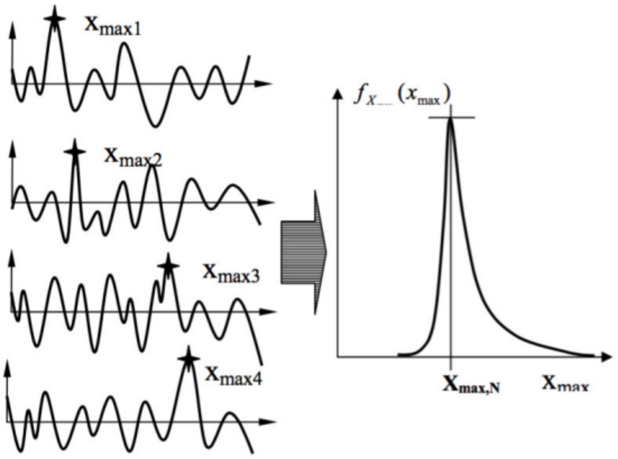

Figure 4.13: Illustration of data behind the extreme value distribution [30].

4.7.1 The Gumbel Distribution

According to DNV-OS-E301, the Gumbel distribution is often a well-suited model for the extreme value distribution of the mooring line tension. The cumulative distribution function and the probability density function for the Gumbel distribution are given in Equation 4.44 and 4.45 respectively.

$$F_y(y) = \exp\left\{-e^{-\tau(y-\gamma)}\right\}, -\infty \leq t \leq \infty \tag{4.44}$$

$$f_y(y) = \tau \exp\left\{-\tau(y-\gamma) - e^{-\tau(y-\gamma)}\right\} \tag{4.45}$$

Where y is the value of the largest maxima from each sample of mooring line tension, γ and τ are the location parameter and scale parameter of the Gumbel distribution, respectively. The parameters of the Gumbel distribution can be found through the parameter estimators given in Equation 4.46 and 4.47:

$$\hat{\tau} = \frac{c_1}{\hat{s}_y} \tag{4.46}$$

$$\hat{\gamma} = \hat{\mu}_y - \frac{c_2}{c_1}\hat{s}_y \tag{4.47}$$

Where $\hat{s}_y$ and $\hat{\mu}_y$ is the standard deviation and the mean value of the sample data and, c_1 and c_2 are functions of the number of sample values, N_y, given by the following set of equations:

$$c_1 = \sqrt{c_3 - c_2^2} \tag{4.48}$$

$$c_2 = \frac{1}{N_y} \sum_{i=1}^{N_y} - \ln \left[- \ln \left(\frac{i}{N_y + 1} \right) \right] \tag{4.49}$$

$$c_3 = \frac{1}{N_y} \sum_{i=1}^{N_y} \left[\ln \left[- \ln \left(\frac{i}{N_y + 1} \right) \right] \right]^2 \tag{4.50}$$

The location parameter indicates the location of the peak in the Gumbel distribution and corresponds to the value that is used in the calculation of the characteristic dynamic tension. The scale parameter controls the width of the distribution curve and gives an indication of the uncertainty in the distribution.

4.8 Time-Domain Analysis

The time-domain analysis gives the opportunity to include highly non-linear hydrodynamic load effects, which is not possible when working in the frequency domain where only linear contributions are considered. The advantage of the time domain analysis is hence, that it can capture non-linear hydrodynamic load effects and non-linear interaction effects between bodies. Furthermore, a time-domain analysis gives the response statistics without assumptions concerning the response distribution [42]. The following sections will describe the main methodology that is used to execute a time-domain analysis of a system with 6 Degrees Of Freedom (DOF).

4.8.1 Equation of Motion

The equation of motion is used to describe how a rigid body moves with respect to time and/or frequency. For the sinusoidal motion of a system with 6 degrees of freedom the equation of motion may be written as [43]:

$$(\mathbf{M} + \mathbf{A}(\omega))\ddot{\mathbf{x}} + \mathbf{C}(\omega)\dot{\mathbf{x}} + \mathbf{D_l}\dot{\mathbf{x}} + \mathbf{D_q}\dot{\mathbf{x}}|\dot{\mathbf{x}}| + \mathbf{K}(x)\mathbf{x} = \mathbf{Q}(\mathbf{t}, \mathbf{x}, \dot{\mathbf{x}}) \tag{4.51}$$

where:

$\mathbf{M}$ = Mass matrix

$\mathbf{A}(\omega)$ = Frequency-dependent mass matrix

$\mathbf{x}$ = Position vector

$\mathbf{C}(\omega)$ = Frequency-dependent potential damping matrix

$\mathbf{D_l}$ = Linear damping matrix

$\mathbf{D_q}$ = Quadratic damping matrix

$\mathbf{K}(x)$ = Stiffness matrix (non-linear)

$\mathbf{Q}(\mathbf{t}, \mathbf{x}, \dot{\mathbf{x}})$ = Excitation force vector

The excitation forces on the right-hand side of Equation 4.51 are given by

$$\mathbf{Q}(\mathbf{t}, \mathbf{x}, \dot{\mathbf{x}}) = q_{wi} + q_{wa}^{(1)} + q_{wa}^{(2)} + q_{cu} + q_{ext} \tag{4.52}$$

where:

q_{wi} = Wind drag force

$q_{wa}^{(1)}$ = First order wave excitation force

$q_{wa}^{(2)}$ = Second order wave excitation force

q_{cu} = Current drag force

q_{ext} = Any other forces (e.g. wave drift damping, specified forces and forces from station-keeping and coupling elements, etc.)

To better understand Equation 4.51 a damped single degree of freedom system is considered. Equation 4.51 can be rewritten to the simplified system as follows

$$m\ddot{x} + c\dot{x} + kx = \Re\{\tilde{R}e^{i(\omega t)}\} = R_0 cos(\omega t) \tag{4.53}$$

Where m is the mass, c is the damping, and k is the stiffness of the system. R_0 is the excitation force, and ω is the excitation frequency.

The particular harmonic solution to Equation 4.53 can be written as

$$x_p = \Re\{\tilde{x}e^{i(\omega t)}\} = |\tilde{x}|cos(\omega t + \phi) \tag{4.54}$$

where

$$|x| = \frac{R_0}{k} \cdot DLF \tag{4.55}$$

$$\phi = tan^{-1}\left(\frac{-2\zeta\beta}{1-\beta^2}\right) \tag{4.56}$$

where:

DLF = Dynamic load factor

ϕ = Phase angle between load and response

β = Frequency ratio, given by; $\beta = \frac{\omega}{\omega_0}$

ζ = Damping ratio, given by; $\zeta = \frac{c}{2m\omega_0}$

The DLF is the ratio between the dynamic and static response for the relevant load. The value of the DLF is dependent on the frequency ratio β and can both be larger and less than 1.0. Implying that we can have both a dynamic amplification and a reduction of dynamic response relative to the static solution, u_{st} [30]. The dynamic load factor is given by

$$DLF = \left|\frac{x_{max}}{u_{st}}\right| = \frac{1}{\sqrt{(1-\beta^2)^2 + (2\zeta\beta)^2}} \tag{4.57}$$

Figure 4.14 shows the DLF and phase angle between load and response as a function of the damping ratio, ζ, and frequency ratio, β.

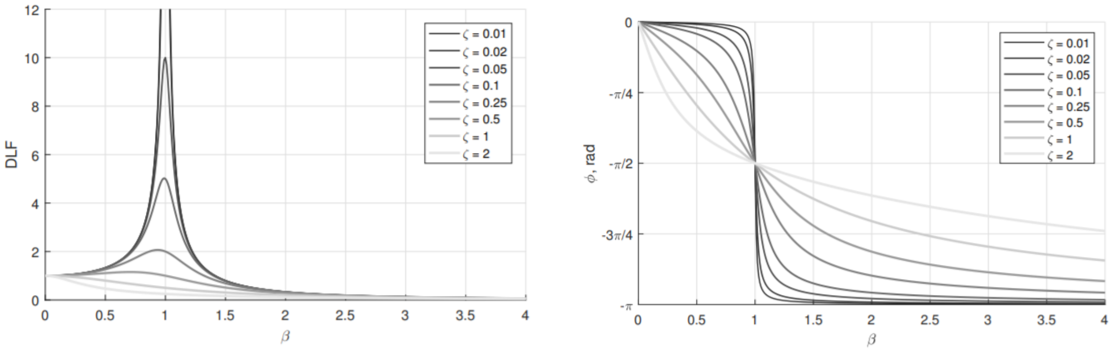

(a) (b)

Figure 4.14: Dynamic load factor (a) and phase angle between load and response (b) as a function of frequency ratio for given values of the damping ratio [30].

Figure 4.14b shows that the phase angle between load and response is in the range 0° to −180°, meaning that the system always responds after the external load in time. From Figure 4.14a the dynamic response can be grouped into three characteristic regions, these regions are:

- Stiffness dominated:
  The load frequency is distinctly lower than the eigenfrequency, $\beta < 1$.
- Resonance:
  The load frequency is equal to or close to the eigenfrequency, $\beta \approx 1$.
- Inertia dominated:
  The load frequency is distinctly higher than the eigenfrequency, $\beta > 1$.

For a stiffness dominated system the loading frequency is experienced as slow, and no significant inertia forces are mobilised. The phase angle between the load and response is zero, as seen in Figure 4.14b. A structure in this regime is said to have a quasi-static behaviour i.e. the external and restoring forces are in equilibrium. A value of the DLF higher than 1 in this regime can be explained by the inertia forces in the structure acting in the same direction as the excitation forces [30].

At resonance the load frequency is equal or in close proximity of the eigenfrequency of the system. The dynamic equilibrium is given by:

$$m\ddot{x} + c\dot{x} + kx = R_0 \Re\{e^{i(\omega t)}\} \tag{4.58}$$

The phase angle is now equal to $-\frac{\pi}{2}$, as seen from Figure 4.14b. Looking now at the time instant with maximum load, i.e. $\omega t = 0$ we have that:

External force $R = R_0$
Displacement $x = 0$
Velocity $\dot{x} = \omega|\tilde{x}|$
Acceleration $\ddot{x} = 0$

From this it becomes clear that there is an equilibrium between the external forces and the damping forces of the system:

$$\omega|\tilde{x}|c = R_0 \tag{4.59}$$

If the damping, c, is small the system will experience large motions due to the external forces.

For the inertia dominated system the inertia of the system is too large for the displacements to become large enough to activate the restoring forces. Equilibrium is thus given by inertia forces. Dynamic equilibrium is again given by Equation 4.58, with the phase angle now being equal to $-\pi$. At the time instant for maximum loading, $\omega t = 0$, we have the following:

External force $R = R_0$
Displacement $x = -|\tilde{x}|$
Velocity $\dot{x} = 0$
Acceleration $\ddot{x} = |\tilde{x}|\omega^2$

This gives us the following equilibrium between external forces, restoring forces, and the inertia forces:

$$\omega^2|\tilde{x}|m = R_0 + k|\tilde{x}| \tag{4.60}$$

In Equation 4.60 the dominating terms are inertia and external force. Hence, the external forces are balanced by the inertia forces of the system, while the restoring forces in fact increase the response [30]. This means that a moored structure has larger dynamic motion in waves compared to what the same structure would have while floating freely, due to the increased stiffness imposed by the mooring system.

4.8.2 Solving the Equation of Motion

The equation of motion in the time domain can be solved in different ways. In SIMO two different solution methods are available, solution by convolution integral and separation of motion. Solution by convolution integral is the default approach and will be described in the following section. The description of the approach is based on the SIMO Theory Manual [36].

Solution by convolution integral

Equation 4.51 contains terms that are both frequency and time-dependent. The intention of solving the equation of motion with the convolution integral is to transform all the frequency-dependent terms to the time domain.

The method starts with assuming that the equations of motion can be written as:

$$\mathbf{M} + \mathbf{A}(\omega)\ddot{\mathbf{x}} + \mathbf{C}(\omega)\dot{\mathbf{x}} + \mathbf{K}\mathbf{x} = \mathbf{f}'(t) = \mathbf{Q} - \mathbf{D_q}\mathbf{f}(\dot{\mathbf{x}}) - \mathbf{D_l}\dot{\mathbf{x}} \tag{4.61}$$

where $\mathbf{f}(\dot{\mathbf{x}}) = \dot{\mathbf{x}}_\mathbf{i}|\dot{\mathbf{x}}_\mathbf{i}|$. Concentrating on the frequency-dependent coefficients only, the equation of dynamic equilibrium can be written as:

$$\mathbf{A}(\omega)\ddot{\mathbf{x}} + \mathbf{C}(\omega)\dot{\mathbf{x}} = \mathbf{f}(t) = \mathbf{f}'(t) - \mathbf{K}\mathbf{x} - \mathbf{M}\ddot{\mathbf{x}} \tag{4.62}$$

Assuming that the force varies sinusoidally at one single frequency, ω, we can write Equation 4.61 in the frequency domain as:

$$(i\omega\mathbf{A}(\omega) + \mathbf{C}(\omega))i\omega\mathbf{X}(\omega) = \mathbf{F}(\omega) \tag{4.63}$$

Using that

$$\mathbf{A}(\omega) = \mathbf{A}_\infty + \mathbf{a}(w) \tag{4.64}$$

$$\mathbf{C}(\omega) = \mathbf{C}_\infty + \mathbf{c}(w) \tag{4.65}$$

Where $\mathbf{A}_\infty = \mathbf{A}(\omega = \infty)$ and $\mathbf{C}_\infty = \mathbf{C}(\omega = \infty) \equiv 0$. Equation 4.63 can thus be written as:

$$-\omega^2\mathbf{A}_\infty\mathbf{X}(\omega) + (i\omega\mathbf{a}(\omega) + \mathbf{c}(\omega))i\omega\mathbf{X}(\omega) = \mathbf{F}(\omega) \tag{4.66}$$

Using the inverse Fourier transform and stating that values of $\mathbf{h}(t-\tau)$ for $t < 0$ are zero, which implies that $\mathbf{h}(t-\tau) \equiv 0$ for $\tau > t$, gives the following relation:

$$\mathbf{A}_\infty\ddot{\mathbf{x}}(t) + \int_0^t \mathbf{h}(t-\tau)\dot{x}(\tau)d\tau = \mathbf{f}(t) \tag{4.67}$$

Substituting $\mathbf{f}'(t)$ from Equation 4.61 and $\mathbf{f}(t)$ from Equation 4.62 gives the equation of motion in time domain:

$$(\mathbf{M} + \mathbf{A}_\infty)\ddot{\mathbf{x}} + \mathbf{D_l}\dot{\mathbf{x}} + \mathbf{D_q}\mathbf{f}(\dot{\mathbf{x}}) + \mathbf{K}\mathbf{x} + \int_0^t \mathbf{h}(t-\tau)\dot{\mathbf{x}}(\tau)d\tau = \mathbf{Q}(t, \mathbf{x}, \dot{\mathbf{x}}) \tag{4.68}$$

$\mathbf{h}(\tau)$ is called the retardation function, and is a result of the memory effects of the fluid [44]. It is computed by a transform of the frequency-dependent added mass and damping. The retardation function for $\tau > 0$ is given as:

$$\mathbf{h}(\tau) = \frac{2}{\pi}\int_0^\infty \mathbf{c}(\omega)cos(\omega\tau)d\omega = -\frac{2}{\pi}\int_0^\infty \omega\mathbf{a}(\omega)sin(\omega\tau)d\omega \tag{4.69}$$

This gives the opportunity to calculate the frequency-dependent added mass and damping through the retardation function:

$$\mathbf{a}(\omega) = -\frac{1}{\omega}\int_0^\infty \mathbf{h}(\tau) sin(\omega\tau) d\tau \tag{4.70}$$

$$\mathbf{c}(\omega) = -\int_0^\infty \mathbf{h}(\tau) cos(\omega\tau) d\tau \tag{4.71}$$

The retardation term represents the radiation force without the added mass force at infinite frequency. It indicates a memory effect of the radiation force meaning that the motion of the floating body will create outgoing waves so that the body has induced wave pressure loads [45]. SIMO uses the potential damping to estimate the retardation function. Figure 4.15 shows the retardation function in surge for the SIMO model used in the analysis

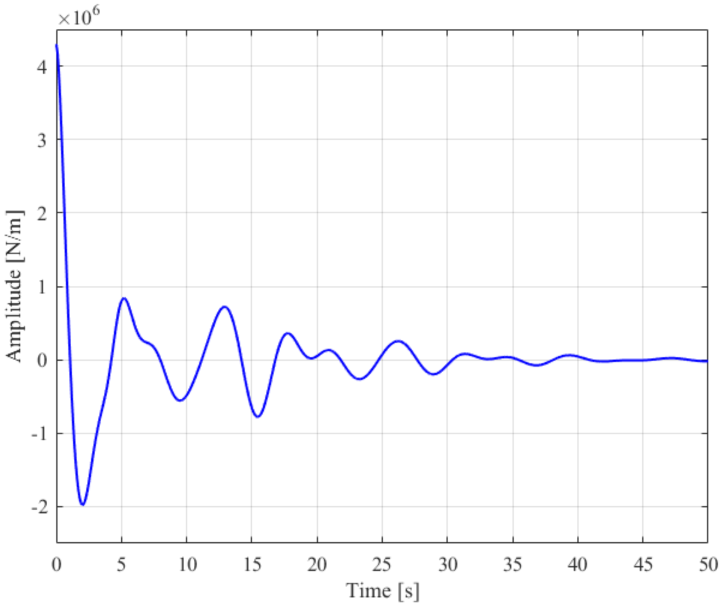

Figure 4.15: Retardation function in surge for the INO WINDMOOR SIMO-model used in SIMA.

4.9 SIMA Workbench

The SIMA workbench is a computer simulation and analysis program for marine operations and floating systems [46]. SIMA supports several physics engines which can operate separately or coupled, some of which are [47]:

- SIMO - Used to model marine operations.
- RIFLEX - Used to model a system consisting of slender elements.
- RIFLEX Coupled - SIMO and RIFLEX coupled. Used to model slender, elastic structures within a marine operation.

The various physics engines are herein described with the main focus on the implementation of mooring systems. The theory presented is based on the SIMO and RIFLEX theory manuals [36] [48].

4.9.1 SIMO

SIMO is a time-domain physics engine used for the simulation of motions and station-keeping behaviour of complex systems of floating vessels and suspended loads. SIMO includes flexible modelling of station-keeping forces and connecting force mechanisms such as anchor lines, ropes, thrusters, fenders, bumpers and docking guide piles. Results provided from the program are presented as time series, statistics and spectral analysis of all forces and motions of all bodies in the analysed system.

In SIMO the implementation of a catenary mooring line model is based on a similar model as used in the mooring analysis program MIMOSA, developed by MARINTEK. This model includes both a quasi-static analysis used for the calculation of tension due to LF motions and a simplified dynamic analysis that accounts for tension due to WF motions and the velocity and acceleration of the line. Originally, this program works in the frequency domain and is therefore a linear solver, in SIMO however, this has been extended to the time domain. The mooring lines are presumed to be of a catenary shape, described by the catenary equations. The quasi-static analysis calculates a two-dimensional line characteristics table by use of the location of the upper end relative to the anchor. Then, at any later stage in the analysis the line forces acting on the structure can be found through the following procedure:

1. The fairlead coordinate is transformed into the line plane.
2. The total tension and direction are found by interpolation from the line characteristics table.
3. The resulting force is transformed back into the body coordinate system.

Dynamic effects, i.e. effects due to velocity and acceleration of the line, may cause the line tension to deviate from the quasi-static analysis. Especially transverse drag contributions will tend to increase the line tension relative to the quasi-static analysis. A simplified dynamic model developed by Larsen and Sandvik [49] may thus be used in addition to the quasi-static analysis in SIMO to capture this effect to some extent. The model assumes that only the tangential component of the top end motion of the line has any influence on the dynamic tension and the shape of the dynamic motion due to this top-end motion is equal to the change in static line geometry. The model can be represented by an equivalent geometric model as shown in Figure 4.16, where $x(t)$ represents the imposed tangential motion of the upper line end and $u(t)$ is the part of this upper-end motion that is compensated by geometric change of the line. The difference between x and u will thus represent the axial stretching of the line. k_G and k_E represent the geometric catenary stiffness and the axial line stiffness of the line respectfully, and c^* is the generalised line damping. This method however, requires that the wave frequency motion of the FWT is calculated in the frequency domain, and thus, does not include contributions from non-linear effects in vessel motions. Non-linear effects are particularly relevant for load cases with severe sea states and large vessel motions. Hence, this dynamic model has not been utilised during simulations done in this work.

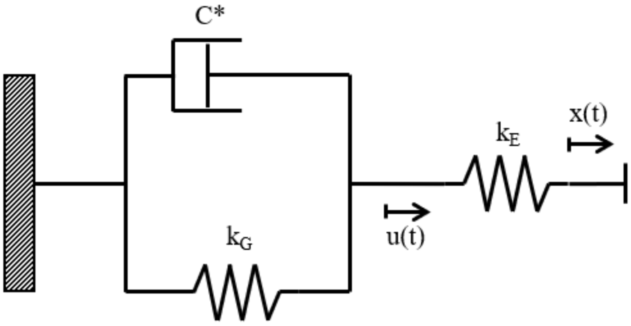

Figure 4.16: Equivalent geometric model for dynamic mooring line effects in SIMO.

4.9.2 RIFLEX Coupled

RIFLEX was initially designed for solving problems involving risers but has proven to be well suited for analyses of other types of slender elements such as mooring lines. RIFLEX is based on the non-linear finite element analysis method. When RIFLEX is incorporated into the analysis, a separated or coupled approach of the time domain analysis may be used in SIMA.

Separated analysis

The computational process of the separated approach is described in Figure 4.17.

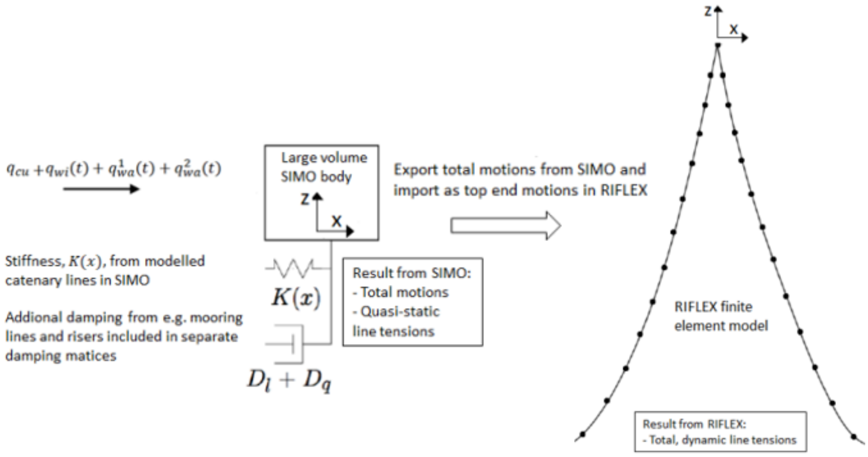

Figure 4.17: Seperated analysis of large volume SIMO body and slender RIFLEX model [50].

In the separated analysis, the total motions of the SIMO-body are calculated. Restoring stiffness for the mooring system is given as input along with a separate damping matrix. The total motion of the structure is calculated as an effect of the external forces along with the quasi-static line tensions. Results from these calculations are then given as input to the RIFLEX analysis which then calculates the total dynamic line tensions due to top end motions of the lines.

Coupled analysis

The computational process of the coupled approach is described in Figure 4.18.

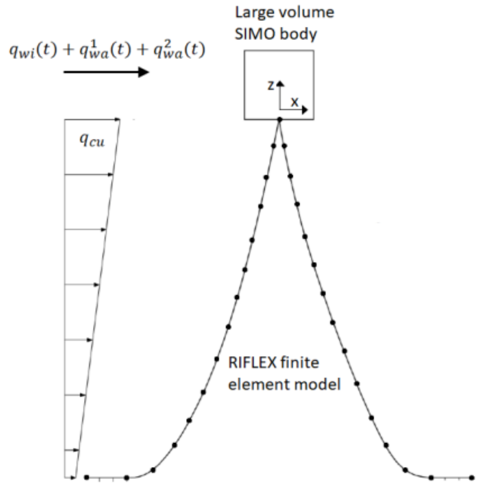

Figure 4.18: Coupled analysis of large volume SIMO body and slender RIFLEX model [50].

In the coupled analysis the SIMO and RIFLEX simulations are done simultaneously using a non-linear time-domain approach for dynamic analyses. Motions of the SIMO-body are given as direct input to the RIFLEX model of the mooring system. Dynamic equilibrium is reached at each time step, and thus, ensures consistent treatment of the coupling effects between floater and mooring system. This means that the coupling effects are automatically included in the analysis scheme.

Coupling effects from the mooring system are restoring, damping, and inertia forces where the main contributors are [39]:

Restoring:

- Static restoring force
- Current loading and its effects on the restoring force
- Seafloor friction

Damping:

- Damping from mooring lines motions and current
- Friction forces due to hull contact

Inertia:

- Additional inertia forces due to the mooring system

The quasi-static approach can only accurately account for the static restoring force, whereas the fully coupled analysis can account for all the effects listed above.

4.9.3 RIFLEX Mooring System Formulation

In RIFLEX the mooring system is modelled as a slender system with the use of bar elements. A simple definition of the modelling of one mooring line is given in Figure 4.19.

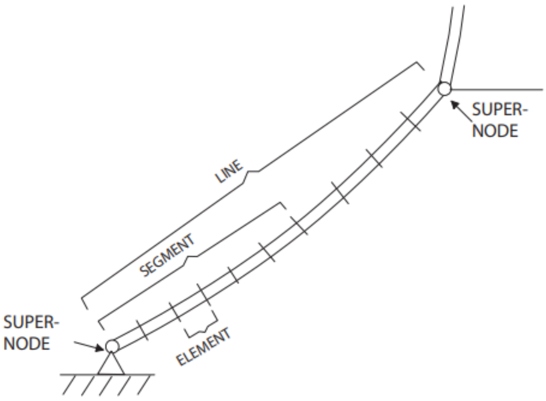

Figure 4.19: System definition terms in RIFLEX [51].

A line is a linear structural element between super nodes built up by a sequence of segments which have homogeneous cross-sectional properties. Each segment can have a separate specification for the cross-sectional component, length, and number of elements to be used for finite element discretization. A line can be modelled as one segment if the line has the same structural proprieties for its entire length.

As mentioned, the elements used to model the mooring lines are bar elements which have one node at each end of the element with three translational degrees of freedom. This means that the elements can move in x-, y-, and z-direction in the global coordinate system but they do not support rotational motion. RIFLEX calculates the dynamic equilibrium for the finite element system model in the general form as [48]:

$$\boldsymbol{R}^I(\boldsymbol{r},\ddot{\boldsymbol{r}},\boldsymbol{t}) + \boldsymbol{R}^D(\boldsymbol{r},\dot{\boldsymbol{r}},\boldsymbol{t}) + \boldsymbol{R}^S(\boldsymbol{r},\boldsymbol{t}) = \boldsymbol{R}^E(\boldsymbol{r},\dot{\boldsymbol{r}},\boldsymbol{t}) \tag{4.72}$$

where

$\boldsymbol{R}^I$ - Inertia force vector
$\boldsymbol{R}^D$ - Damping force vector
$\boldsymbol{R}^S$ - Internal structural reaction force vector
$\boldsymbol{R}^E$ - External force vector
$\boldsymbol{r},\dot{\boldsymbol{r}},\ddot{\boldsymbol{r}}$ - Structural displacement, velocity and acceleration vector

All force vectors in Equation 4.72 are established by the assembly of contributions from element and nodal forces in the element model. Relevant contributions to mooring design are included in the various vectors. The inertia force vector accounts for added mass contributions in local directions for the elements while the damping force vector includes the hydrodynamic damping contribution. The external force vector includes contributions from drag and wave-particle acceleration terms in the Morison equation and forced displacements due to top-end motions. Equation 4.72 is a highly nonlinear system of differential equations which is solved through a nonlinear time-domain analysis this results in a quite accurate solution of the behaviour of the mooring lines.

4.10 Differences Between Quasi-Static and Dynamic Analysis

During a quasi-static analysis, the hydrodynamic and inertial forces acting on the mooring line are neglected, and hence, the shape and tension distribution along the mooring line are only dependent on the top end position. This can influence the FWT response and mooring line loads. Furthermore, a situation as illustrated in Figure 4.20 may occur, where the top part of the mooring line follows the FWT motion and the bottom part has a delayed response due to mooring line drag and inertia. Figure 4.20 shows that the mooring line in a dynamic model may not follow a catenary profile as assumed in the quasi-static model, indicating a possible large deviation in the calculated loads between the two models. Yang et al. [52], found large discrepancies in the top end tension between the results found from a dynamic and quasi-static analysis with the dynamic analysis resulting in significantly larger tension. Further, in the work done in the comparison of time domain, frequency domain, and quasi-static analysis by Kwan and Bruen [53], it is concluded that a quasi-static analysis should not be used for fatigue design or final design of permanent mooring systems. The quasi-static analysis has the advantage of simplicity and therefore a shorter computational time, however, with modern computing capability, the time saving becomes negligible.

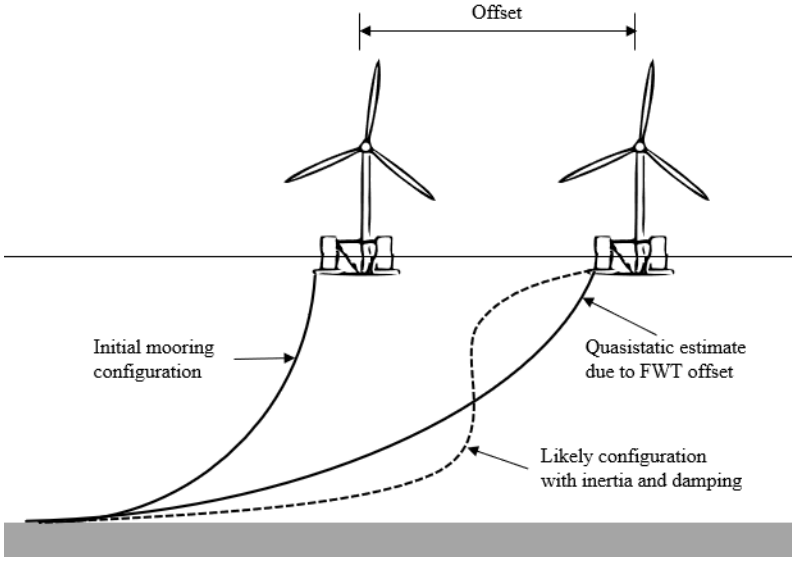

Figure 4.20: Differences between the quasi-static and dynamic mooring models (adapted from [16]).

4.11 Instability Phenomena for Floating Wind Turbines

Floating wind technology is, compared to floating oil and gas installations, a new technology which still is in its juvenile years. Due to this, new findings regarding the behaviour of FWTs are frequently being made, some of which may result in large unwanted motions in one or several degrees of freedom called motion instability phenomenon. The mooring system of the FWT may help in preventing or limiting such motions. This section will discuss two of these phenomena.

4.11.1 Aerodynamic Roll-Yaw Instability

In the study done by Haslum et al. [54] a recently discovered instability phenomenon excited by anti-symmetric coupling terms in roll and yaw caused by the turbine thrust force is investigated. This may result in rigid body roll and yaw oscillations, particularly for floaters with a small separation between the uncoupled roll and yaw natural periods.

In the study, a 2 DOF system including the roll and yaw components is established and the eigenvalues for that system are found analytically. It was found that the stability limit depends on the frequency separation between roll and yaw, in addition to the magnitude of the thrust force relative to the system inertia. The system is stable if the uncoupled natural period in yaw is adequately smaller or larger than the natural period in roll. For cases where the eigenfrequency in roll is smaller than the eigenfrequency in yaw the following criteria were found:

$$\frac{\omega_{66}}{\omega_{44}} = \sqrt{\frac{K_{66}M_{44}}{M_{66}K_{44}}} \geq \sqrt{1 + \frac{2h}{K_{44}}\sqrt{\frac{M_{44}}{M_{66}}}F_t} \tag{4.73}$$

where ω_{ii} are the uncoupled eigenfrequencies, K_{44} is the hydrostatic stiffness in roll, while K_{66} is the mooring stiffness in yaw. M_{44} and M_{66} are the total inertia in roll and yaw respectively. h is the distance from the reference origin to the rotor hub and F_t is the thrust force from the turbine.

Using Equation4.73 a criterion for the mooring line yaw stiffness can be written as:

$$K_{66} \geqslant \frac{K_{44} \cdot M_{66}}{M_{44}} + 2 \cdot F_t \cdot h \cdot \sqrt{\frac{M_{66}}{M_{44}}} \tag{4.74}$$

It was also found, quite counter-intuitively, that damping forces reduce the stability margin.

4.11.2 Yaw Moment Instability

This instability is mainly caused by an aerodynamic yaw moment, but for FWTs with a semi-submersible substructure, additional moments from wind, currents, and waves may also contribute to this behaviour.

Figure 4.21 gives an illustration of the mechanics behind a possible instability in yaw moment. The green line in the figure represents the restoring in yaw provided by the mooring system, while the blue line is the yaw moment created by external forces acting in the opposite direction compared to the restoring moment. The resulting moment in yaw is illustrated by the red line. Due to the behaviour of the restoring moment and external moment, the resulting moment will have a relatively low value at lower yaw angles, illustrated as a flat line in the resulting yaw moment. This allows for the FWT to quite easily rotate in yaw until it reaches a new equilibrium point between the two sources of moments. If the maximum point of the resulting moment is low, a wind gust or large wave may push the yaw angle of the FWT over the maximum point in the resulting moment and back towards zero degrees and potentially over to the opposite side.

To mitigate this a potential solution may be to give the RNA of the turbine a yaw angle away from the incoming wind. This will result in an increased resulting yaw moment on one side of the graph which acts as a barrier for the FWT yaw angle and prevents it from experiencing large variations in yaw angle during extreme load cases where the turbine is parked.

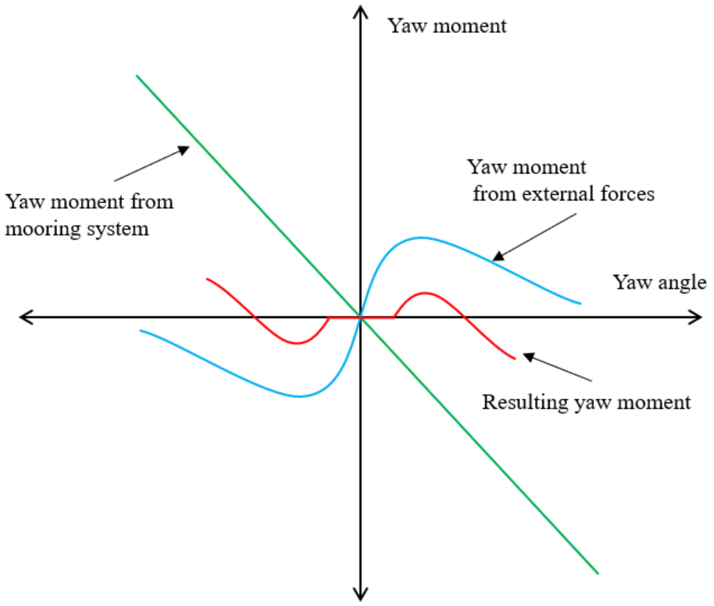

Figure 4.21: Illustration of yaw instability mechanics.

5 Site and Load Case Description

This section will give a brief description of the selected site for use as a base case location in the calculations and design of the mooring system. Further, the design load cases considered to be relevant for mooring design are presented and described.

5.1 The Jupiter Site

For work done in this project, the relevant site-specific data is taken from the metocean data for the Jupiter site off the coast of Brittany, northern France [55]. Figure 5.1 shows the position of the area.

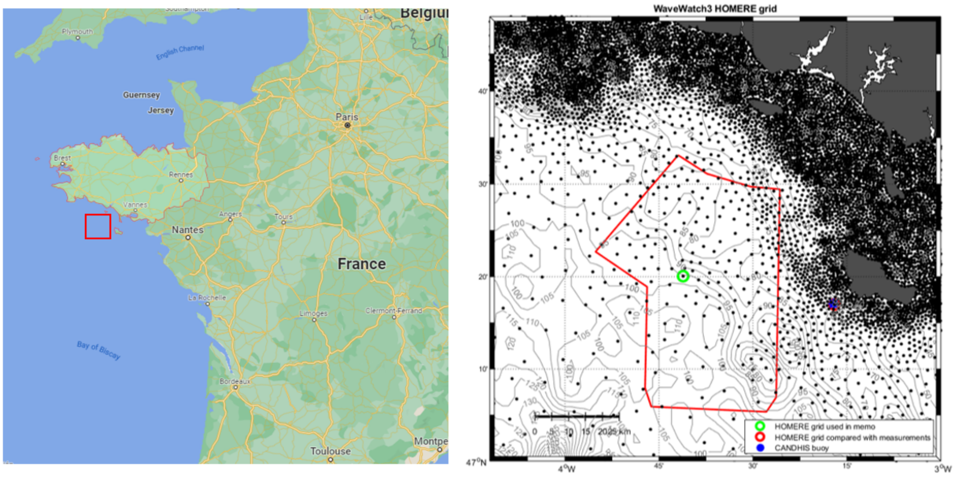

Figure 5.1: Map showing the location of the Jupiter area [56] [55].

The water depth in the area ranges from 60 to 110 m, a depth of 100 m is chosen for the work done in this project. Wave data is extracted from the CANDHIS buoy network around 50 km east of the Jupiter site. The wind speed data is generated based on hindcast data at 10 m above the mean sea level, the wind power law (Equation 4.13) with an exponent of 0.095 is used to estimate wind at 145 m above the mean sea level. The same power law is used to find the appropriate value for wind speed at hub height. A summary of the calculated extreme wind and wave conditions is provided in Figure 5.2.

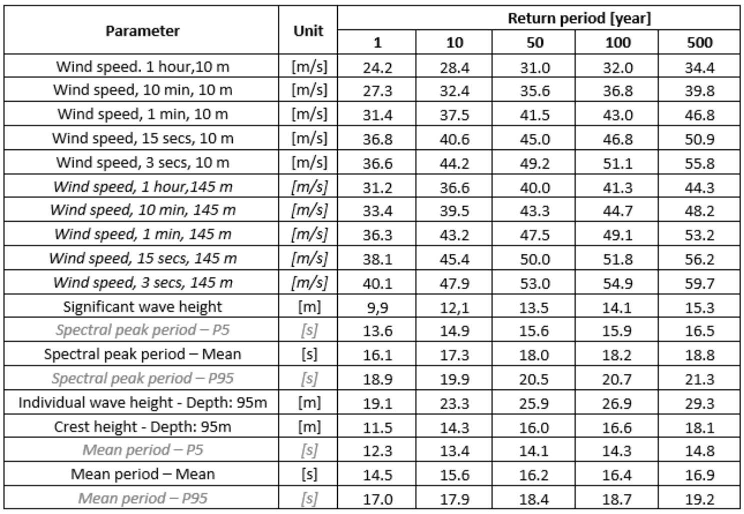

Parameter	Unit	Return period [year]				
		1	10	50	100	500
Wind speed. 1 hour,10 m	[m/s]	24.2	28.4	31.0	32.0	34.4
Wind speed, 10 min, 10 m	[m/s]	27.3	32.4	35.6	36.8	39.8
Wind speed, 1 min, 10 m	[m/s]	31.4	37.5	41.5	43.0	46.8
Wind speed, 15 secs, 10 m	[m/s]	36.8	40.6	45.0	46.8	50.9
Wind speed, 3 secs, 10 m	[m/s]	36.6	44.2	49.2	51.1	55.8
Wind speed, 1 hour,145 m	*[m/s]*	31.2	36.6	40.0	41.3	44.3
Wind speed, 10 min, 145 m	*[m/s]*	33.4	39.5	43.3	44.7	48.2
Wind speed, 1 min, 145 m	*[m/s]*	36.3	43.2	47.5	49.1	53.2
Wind speed, 15 secs, 145 m	*[m/s]*	38.1	45.4	50.0	51.8	56.2
Wind speed, 3 secs, 145 m	*[m/s]*	40.1	47.9	53.0	54.9	59.7
Significant wave height	[m]	9,9	12,1	13.5	14.1	15.3
Spectral peak period – P5	*[s]*	13.6	14.9	15.6	15.9	16.5
Spectral peak period – Mean	[s]	16.1	17.3	18.0	18.2	18.8
Spectral peak period – P95	*[s]*	18.9	19.9	20.5	20.7	21.3
Individual wave height - Depth: 95m	[m]	19.1	23.3	25.9	26.9	29.3
Crest height - Depth: 95m	[m]	11.5	14.3	16.0	16.6	18.1
Mean period – P5	*[s]*	12.3	13.4	14.1	14.3	14.8
Mean period – Mean	[s]	14.5	15.6	16.2	16.4	16.9
Mean period – P95	*[s]*	17.0	17.9	18.4	18.7	19.2

Figure 5.2: Summary of estimated wind and wave extremes at Jupiter [55].

Further, the contour lines of significant wave height H_s and spectral peak period T_p with return period 1, 10, 50, 100 and 500 years for Omni-directional waves for the Jupiter site are given in Figure 5.3. For calculations of extreme conditions for wind turbines, the 50-year contour lines are used.

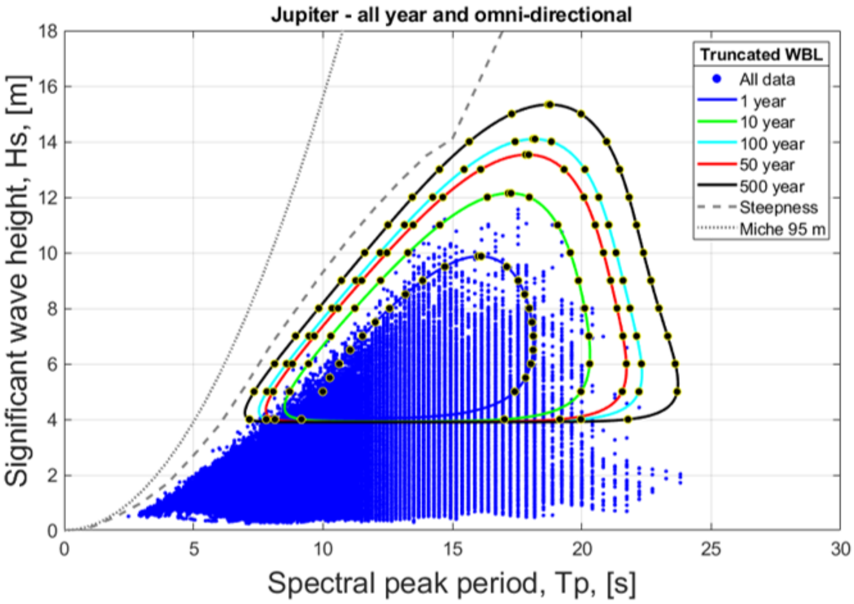

Figure 5.3: Contour lines of $H_s - T_p$ with return periods 1, 10, 50, 100 and 500 years for Omni-directional waves at Jupiter. The duration of sea state is 3 hours. Dashed and dotted lines represent steepness criteria and upper limits of H_s [55].

5.2 Design Load Cases for Mooring Design

Based on recommendations and requirements given in relevant design standards for FWTs presented in Section 4.6.6, a load case matrix has been established in order to define the governing design load cases relevant for the Jupiter site. Three main load cases are used which are based on the load cases presented in Table 4.4, these are:

- DLC 1.1: Investigates specified combinations of environmental parameters at the cut-out wind speed of the turbine.
- DLC 1.6: Investigates specified combinations of environmental parameters at the rated wind speed of the turbine.
- DlC 6.1: Investigates specified combinations of environmental parameters along the 50-year contour line for the Jupiter site.

Both in-line and in-between directions have been analysed for all load cases with wind, wave and current acting in the same direction. In addition, a non-collinear environment has been analysed for both the in-line and in-between directions. According to DNV-OS-E301 the non-collinear environment can be applied as follows:

- Wave towards the units bow
- Wind 30°relative to the waves
- Current 45°relative to the waves

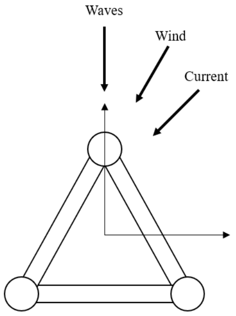

The environmental parameters for the design load cases are summarised in Table 5.1 for DLC 1.1 and 1.6 and in Table 5.2 for DLC 6.1 and are extracted from the Jupiter metocean design basis [55]. As stated in Section 4.6.6 a 50-year current value for DLC 6.1 is regarded as quite conservative. Thus, this value has been changed with the 5-year value for the current speed. For DLC 1.1 and 1.6 a current speed with a 1-year return period is used.

Figure 5.4 illustrates how the total surface currents at the Jupiter site are composed of tidal and residual currents.

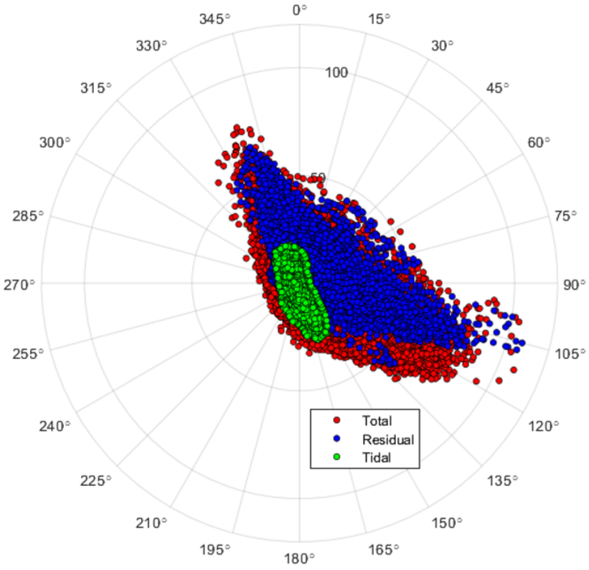

Figure 5.4: Illustration of how the total surface current is composed of tidal and residual currents. Values in cm/s and direction is towards [55].

As shown in Figure 5.4, the total surface current is mainly governed by the residual component which is assumed to be dominated by the wind-generated current. Hence, the variation of the current is modelled as a wind-generated current with a linear profile from still water level to z = -50 m as shown in Equation 5.1. The current is assumed to die out at water depths deeper than 50 m.

$$u_c(z) = u_c(z=0)\left(\frac{50+z}{50}\right) \qquad \text{for} \qquad -50 \leq z \leq 0 \tag{5.1}$$

Table 5.1: Environmental parameters for DLC 1.1 and 1.6.

DLC	Mean wind speed at hub height [m/s]	H_s [m]	T_p [s]	Current speed at $z = 0$ [m/s]
1.1	24	6.2	14	0.73
1.6	10.5	8.2	15.3	0.73

H_s and T_p values for DLC 6.1 in Table 5.2 are the 50-year contour values from the contour lines in Figure 5.3. All six combinations of H_s and T_p in this table are relevant for DLC 6.1. However, only the combination that yields the highest design tension value for the chain mooring system is further considered during the analysis of synthetic mooring lines.

Table 5.2: Environmental parameters for DLC 6.1.

H_s and T_p countour parameters with 50-year return period			Mean wind speed at hub height [m/s]	Current speed at $z = 0$ [m/s]
H_s [m]	T_{p-Low} [s]	T_{p-High} [s]		
13.5	18	18	42.9	0.89
13	16.1	19.3		
12	14.6	20.1		

Additionally to the above-mentioned DLCs, a DLC with the expected wave height at rated wind speed is also considered. The main purpose of this DLC is to control for any unwanted behaviour of the FWT when moored with the investigated mooring systems at a less severe environmental condition. As DLC 1.1 is the load case that investigates conditions with the expected wave height at a given wind speed the last DLC is called 1.1R. Parameters for DLC 1.1R is given in Table 5.3

Table 5.3: Environmental parameters for DLC 1.1R.

DLC	Mean wind speed at hub height [m/s]	H_s [m]	T_p [s]	Current speed at $z = 0$ [m/s]
1.1R	10.5	2.1	11.1	0.73

6 Numerical Modelling

The following sections will discuss possible modelling solutions for the INO WINDMOOR FWT and present the modelling procedure used in the SIMA workbench to execute the simulations. The parameters of the preliminary chain mooring system is also presented followed by a brief description on how the SyROPE-model is implemented in SIMA.

6.1 Model Selection

The SIMA workbench gives the opportunity to model the INO WINDMOOR FWT in several ways where one model setup may be more advantageous than others depending on what the focus area of the simulations is. Possible modellings solutions are summarised in Figure 6.1, a description of the models is given in the following sections along with pros and cons for the different model setups. Work done in this project is focused on the SIMO and RIFLEX-coupled models.

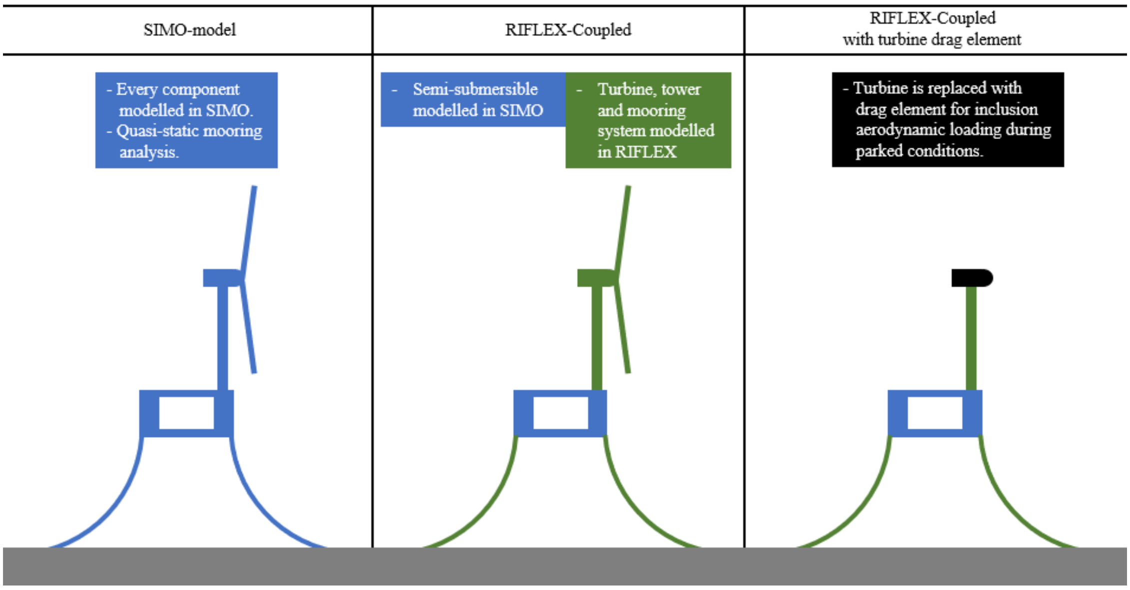

Figure 6.1: Modelling solutions in SIMA for the INO WINDMOOR 12 MW FWT.

6.1.1 SIMO-Model

For the SIMO-model every containing element is modelled within a SIMO-task. This also includes the mooring lines and wind turbine with belonging components. The turbine tower is modelled with drag elements for the inclusion of aerodynamic forces but does not include any bending of the tower. The bending of turbine blades is also not included in this model. Mooring line tension and reaction forces are calculated through a quasi-static approach as described in Section 4.9. The main advantage when using this model setup is a reduction in calculation time for the simulations. A quasi-static approach for the mooring calculations is suitable for mean offset and LF motions of the floater and is believed to be suitable for a system of this configuration in shallow waters where drag contributions on the mooring lines are of lower importance. However, mooring line response due to WF motions may be significant also in shallow waters due to dynamic effects as discussed in Section 4.10. The SIMO-model may thus not be sufficient for ULS design.

6.1.2 RIFLEX-Coupled

In the RIFLEX-coupled model, the semi-submersible is modelled as a SIMO-body while the remaining components are modelled thru RIFLEX. This model setup is an aero-hydro-servo-elastic analysis which includes contributions from aerodynamics, wind turbine control, hydrodynamics, and structural dynamics simultaneously. This implies that contributions from tower and turbine blade bending are included, and thus, change the dynamic behaviour of the system. Further, the mooring lines are modelled in a fully dynamic model that includes both inertia and drag contributions from the lines. This model setup captures the coupled dynamic effects better than the SIMO-model and is hence believed to give more accurate results of the mooring line tension. The RIFLEX-coupled model is more computational heavy than the SIMO-model, however, the difference in computational time between the two is not of a substantial manner. The RIFLEX-model has on average a computational time that is ten minutes longer than the SIMO-model for a simulation length of 4000 seconds. RIFLEX has, unlike SIMO, the capability of modelling synthetic mooring lines with the SyROPE-model and is thus needed for analyses of mooring systems of such configuration.

6.1.3 RIFLEX-Coupled - Turbine Drag Element

This model is suggested as a possible simplification of the full RIFLEX-coupled model, where the Rotor and Nacelle Assembly (RNA) is interchanged with a corresponding drag element. This model setup is thought to be beneficial in load cases where the turbine is parked, i.e. not rotating, due to a reduction in computational time. In parked conditions the turbine mainly acts as a drag element, capturing the forces from wind over the blades and nacelle. This could also be done thru a drag element with appropriate drag coefficients and thereby avoiding the needed BEM-calculations that are done when the turbine is included. Typical ULS load cases for the design of FWTs mooring systems are the 50-year condition where the turbine is parked. Hence, a simplified model as suggested here could ease the design process of mooring systems for FWTs. Work done in this project has not looked further into this model concept due to time limitations, the model is only presented as a possible modelling solution.

6.2 Model Parameters

The concept for the floating platform used in the INO WINDMOOR model was designed jointly by Equinor and Inocean. The structure is of a semi-submersible design and consists of three columns supported by pontoons and deck beams. The 12 MW wind turbine and tower are installed on top of one of the columns, Figure 6.2a gives an illustration of the concept while Figure 6.2b and 6.2c shows the SIMO- and RIFLEX-model respectively that was introduced in Section 6.1. Generally, the modelling approach for the two models is quite similar, where the largest difference is found in the modelling of turbine tower, RNA, and mooring system. Both models employ the same SIMO-body for the semi-submersible platform with equal hydrodynamic coefficients established thru a hydrodynamic diffraction-radiation analysis in WAMIT carried out by SINTEF for the work done in [57].

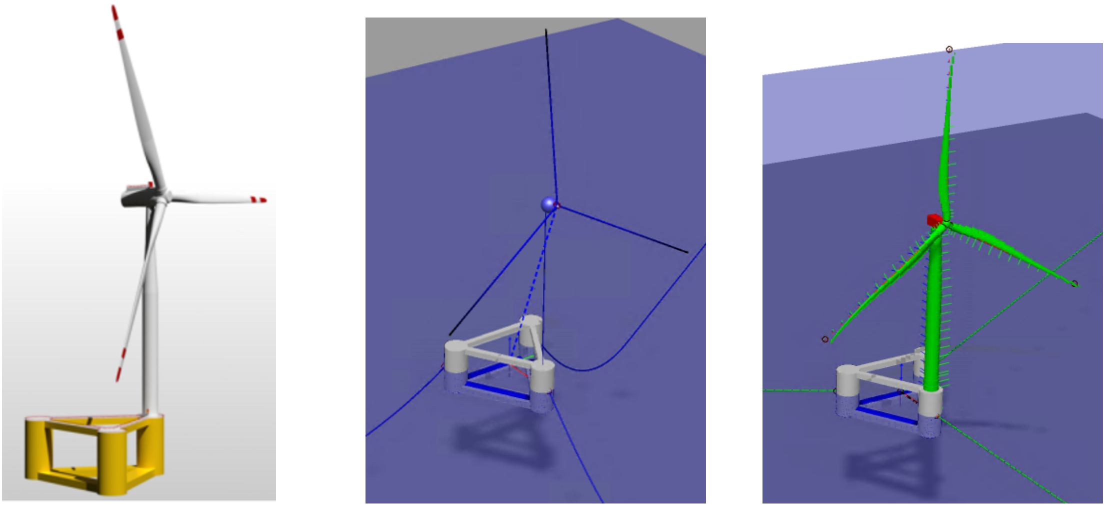
(a) (b) (c)

Figure 6.2: The INO WINDMOOR concept (a), SIMO-model (b), and RIFLEX-model (c).

The main particulars for the floating platform and the complete FWT are given in Table 6.1. The radii of gyration for the platform refer to the platform centre of gravity (CoG), while the radii of gyration for the full model refer to the FWT CoG. The following sections will describe the main input parameters specified for the two SIMA-models.

Table 6.1: Floating platform main dimensions and inertia properties and the full FWT main properties.

Platform		Full FWT	
Property	Value	Property	Value
Column diameter (m)	15.0	Displacement (t)	14176.1
Column height (m)	31.0	Draft (m)	15.5
Pontoon width (m)	10.0	CG_x^* (m)	[-0.37,0.37]
Pontoon height(m)	4.0	CG_y^* (m)	[-0.37,0.37]
Center-center distance (m)	61.0	CG_z (m)	4.23
Deck beam width (m)	3.5	R_{xx} (m)	43.67
Deck beam height (m)	3.5	R_{yy} (m)	44.18
Total substructure mass (t)	11974.0	R_{zz} (m)	30.26
Total substructure CG_x (m)	-5.91	Static heel angle at rated thrust (deg)	6.4
Total substructure CG_z (m)	-9.7	Still water airgap to column top (m)	15.5
Total substructure R_{xx} (m)	23.66	Still water airgap to deck beam bottom (m)	12.0
Total substructure R_{yy} (m)	18.63	Still water airgap to blade tip (m)	21.7
Total substructure R_{zz} (m)	28.10		

* CG_x and CG_y are dependent on the nacelle orientation.
For 0°orientation , $CG_x = 0.37$ m and $CG_y = 0$ m.
For 90°orientation, $CG_x = 0$ m and $CG_y = 0.37$ m.

6.2.1 Kinetics

Two SIMO bodies are used to construct the full SIMA-model, one used for defining the horizontal axis wind turbine and one for the semi-submersible substructure. This section will describe the main kinetic properties given to the respective SIMO bodies. The coordinate system for the complete model is given in Figure 6.3, where the origin of the system is placed at the geometric centre of the structure in the x-and y-direction and at the waterline in the z-direction.

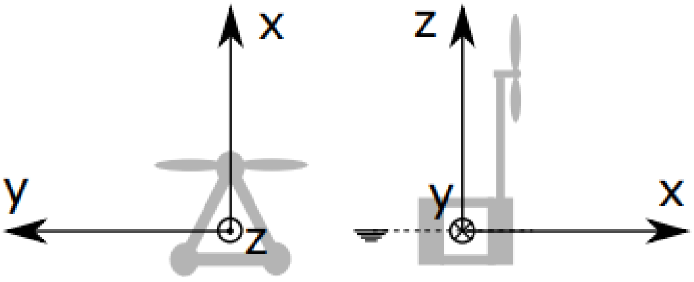

Figure 6.3: Local (body-fixed) coordinate system [57].

Mass and inertia

Table 6.2 summarises the mass and mass moment of inertia specified for the two SIMO-bodies for each model. The coordinates given in the table refer to the global coordinate system of the model, as illustrated in Figure 6.3.

Table 6.2: Mass properties assigned to SIMO-bodies.

	SIMO-model		RIFLEX-model	
Property	Rotor	Semi	Nacelle	Semi
Mass (t)	249.07	13139	600	11974
X-pos (m)	46.158	-2.262	35.128	-5.91
Y-pos (m)	0	0	0	0
Z-pos (m)	131.7	-3.815	125.7	-9.7
I_{xx} (kgmˆ2)	3.27e+08	1.7425e+10	8.183e+06	7.8296e+09
I_{yy} (kgmˆ2)	2.33e+08	1.6741e+10	2.0717e+07	5.7008e+09
I_{zz} (kgmˆ2)	1.13e+08	1.1323e+10	1.3534e+07	9.873e+09
I_{zx} (kgmˆ2)	0	-3.01e+09	-6.8508e+06	-6.8643e+08

For the SIMO-model the Rotor-body represents the rotating parts of the RNA which is the combined mass of the rotor hub and blades. This is due to how the turbine is modelled in the SIMO-model, and the mass applied to this body will be a rotating mass during the analyses. Due to this, the remaining mass of the RNA is moved to a time-dependent point mass on the semi-body. Values for the time-dependent point mass are given in Table 6.3.

For the RIFLEX-model the corresponding SIMO-body is called Nacelle, where only the weight of the nacelle assembly is included. The remaining RNA mass is included through RIFLEX modelling of the turbine blades and shaft. The turbine tower is modelled as slender elements through RIFLEX modelling which is the reason for the difference in mass for the Semi-body compared to the SIMO-model where the tower mass is included in the mass of the Semi-body.

Table 6.3: Specification of the time-dependent point mass applied to the Semi-body.

Body	Mass (t)	X-pos (m)	Y-pos (m)	Z-pos (m)
Semi	789.07	40.898	0	129.83

For SIMO-bodies the moment of inertia is given with respect to the body-fixed origin and not the CoG of the body. When the moments of inertia and negative products of inertia are known at the centre of gravity they transform to the body-fixed origin by the following expressions provided by the SIMO user manual[58]:

$$\mathrm{I_{XX}} = I_{xx}^{cog} + \mathrm{M} \cdot \left(\mathrm{YCOG}^2 + \mathrm{ZCOG}^2\right) \tag{6.1}$$

$$\mathrm{I_{YY}} = I_{yy}^{cog} + \mathrm{M} \cdot \left(\mathrm{XCOG}^2 + \mathrm{ZCOG}^2\right) \tag{6.2}$$

$$\mathrm{I_{ZZ}} = I_{zz}^{\mathrm{cog}} + \mathrm{M} \cdot \left(\mathrm{XCOG}^2 + \mathrm{YCOG}^2\right) \tag{6.3}$$

$$\mathrm{I_{ZX}} = I_{zx}^{cog} - \mathrm{M} \cdot \mathrm{XCOG} \cdot \mathrm{ZCOG} \tag{6.4}$$

Hydrostatic stiffness

The hydrostatic restoring matrix contains only contributions from the volume variation caused by small motions around the equilibrium position since the mass and buoyancy are included separately. This provides stiffness in the heave, roll, and pitch motions of the structure. The mooring system provides stiffness for the remaining degrees of freedom.

The hydrostatic restoring matrix can be written as:

$$\mathbf{K} = \begin{bmatrix} 0 & 0 & 0 & 0 & 0 & 0 \\ 0 & 0 & 0 & 0 & 0 & 0 \\ 0 & 0 & C'_{33} & 0 & 0 & 0 \\ 0 & 0 & 0 & C'_{44} & 0 & 0 \\ 0 & 0 & 0 & 0 & C'_{55} & 0 \\ 0 & 0 & 0 & 0 & 0 & 0 \end{bmatrix} \tag{6.5}$$

where the restoring coefficients C'_{ii} can be found through [18]:

$$C'_{33} = \rho g A_{wp} \tag{6.6}$$

$$C'_{44} = \rho g \iint_{A_{wp}} y^2 ds = \rho g V \overline{GM}_T \tag{6.7}$$

$$C'_{55} = \rho g \iint_{A_{wp}} x^2 ds = \rho g V \overline{GM}_L \tag{6.8}$$

where A_{wp} is the waterplane area, ρ is the water density, g is the acceleration of gravity, $\overline{GM}_T$ is the transverse metacentric height and $\overline{GM}_L$ is the longitudinal metacentric height. Values for the restoring coefficients are given in Table 6.4.

Table 6.4: Restoring coefficients.

C'_{33} (N/m)	C'_{44} (Nm/rad)	C'_{55} (Nm/rad)
5.33e+06	3.38e+09	3.38e+09

The buoyancy force of the structure is included as a specified force, applied at the centre of buoyancy to the platform acting in the positive direction of the global Z-axis. The buoyancy force is calculated as:

$$F_b = \rho g V_{sub} \tag{6.9}$$

where V_{sub} is the submerged volume of the floating substructure.

Linear and quadratic damping

When including hydrodynamic coefficients from a WAMIT-analysis to a SIMO-body, the retardation function is calculated through frequency-dependent radiation damping according to Equation 4.69. During these calculations, a damping residue occurs which is saved to a linear damping matrix and is treated as linear radiation damping. This damping matrix can also be used for user-defined linear damping contributions such as linear mooring line damping. This has not been done for the models used in this work, hence, the only damping defined in the linear damping matrix is the damping residue from the retardation function calculations shown in Equation 6.10 with units [Ns/m].

$$\begin{bmatrix} 1442.2 & 0 & 0 & 0 & 0 & 0 \\ 0 & 1442.2 & 0 & 0 & 0 & 0 \\ 0 & 0 & 1.5018e+06 & 0 & 0 & 0 \\ 0 & 0 & 0 & 7.0073e+08 & 0 & 0 \\ 0 & 0 & 0 & 0 & 7.0073e+08 & 0 \\ 0 & 0 & 0 & 0 & 0 & 2.61e+06 \end{bmatrix} \tag{6.10}$$

Slender elements is incorporated in the model to include damping contributions due to viscous effects from the substructure pontoons and columns, as shown in Figure 6.4.

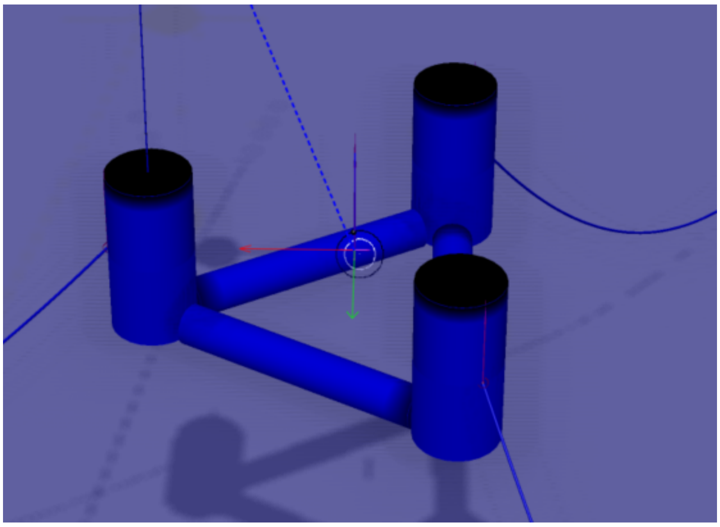

Figure 6.4: Viscous drag elements for inclusion of Morison drag to the substructure.

The quadratic drag contributions are based on the Morison formulation, where the force per unit length is given by:

$$f = \frac{1}{2}\rho C_d D u_r |u_r| \tag{6.11}$$

where D is the characteristic length, here the column diameter or pontoon width/height is given as input. u_r accounts for the platform motions and wave-particle kinematics, only velocity contributions are assigned for the elements. C_d is the non-dimensional drag coefficient and is defined in accordance with DNVGL-RP-C205 Appendix E[29].

The cases used to define the non-dimensional drag coefficients are given in Figure 6.5.

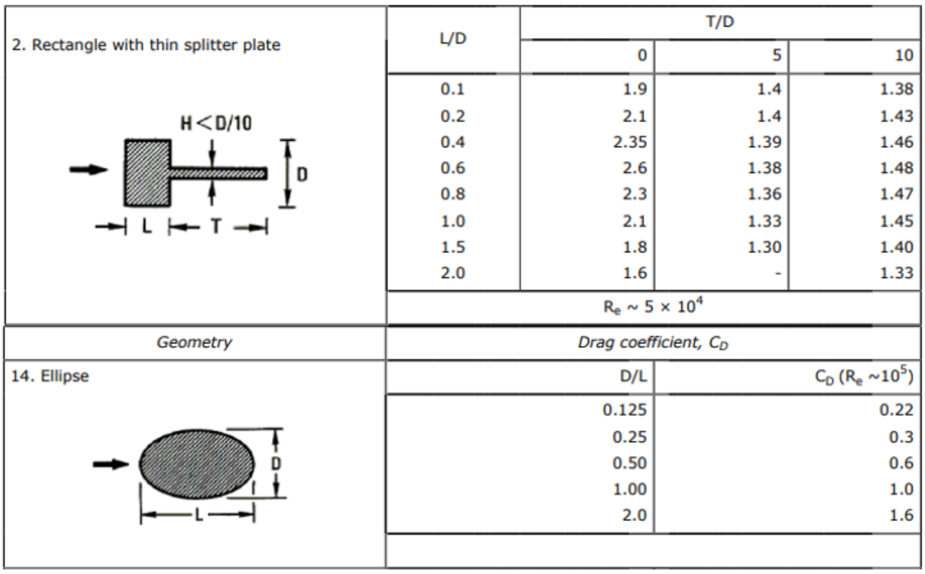

2. Rectangle with thin splitter plate	L/D	T/D		
		0	5	10
	0.1	1.9	1.4	1.38
	0.2	2.1	1.4	1.43
	0.4	2.35	1.39	1.46
	0.6	2.6	1.38	1.48
	0.8	2.3	1.36	1.47
	1.0	2.1	1.33	1.45
	1.5	1.8	1.30	1.40
	2.0	1.6	-	1.33
	$R_e \sim 5 \times 10^4$			

Geometry	*Drag coefficient, C_D*	
14. Ellipse	D/L	C_D ($R_e \sim 10^5$)
	0.125	0.22
	0.25	0.3
	0.50	0.6
	1.00	1.0
	2.0	1.6

Figure 6.5: Drag coefficients for cross-sections applicable for columns and pontoons on the floating substructure [29].

For the pontoons a T/D-value of zero is used along with a L/D-value of 0,4 and 2.5 for the $C_{d,y}$ and $C_{d,z}$ values respectively. The $C_{d,z}$-value for the pontoons has been extrapolated for the $L/D = 2.5$. For the columns a D/L-value of 1 is used, yielding an equal value for both $C_{d,y}$ and $C_{d,z}$. Values for $C_{d,y}$ and $C_{d,z}$ for the respective cross-section are given in Table

Table 6.5

	$C_{d,y}$	$C_{d,z}$
Pontoon	2.3	1.4
Column	1.0	1.0

Slender elements have also been used to include wind forces acting on the tower for the SIMO-model. The tower has been divided into 11 segments to account for the change in tower diameter. The tower diameter is used when defining the quadratic drag coefficient. This coefficient is established in the same manner as described in Equation 6.11, with the air density inserted for ρ. Dimensions for the tower diameter are taken from [57]. For the RIFLEX-model a nondimensional quadratic aerodynamic drag force coefficient is defined for each tower cross-section.

Wave drift force

The wave drift force is due to the structure's ability to diffract and radiate waves. For low frequencies these effects are small and the wave drift force should go to zero. The wave drift force has peaks associated with interference effects between the columns for semi-submersible structures [29]. Wave drift force for surge is shown in Figure 6.6. The behaviour of the wave drift force in Figure 6.6 confirms the anticipations with the largest contributions occurring at higher frequencies and a value of zero at lower frequencies.

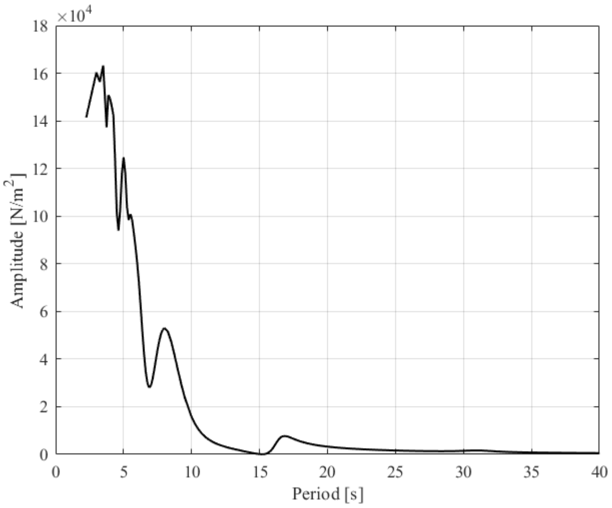

Figure 6.6: Wave drift force in surge for the SIMA-models.

6.2.2 Preliminary Mooring System

A base case mooring system is defined and shall be used as a measure of comparison when new mooring systems of taut configuration with synthetic fibre ropes are analysed. The base case mooring system is of a spread catenary design with three mooring lines, one connected to each column of the floating substructure, with a 120° separation between the lines. An overview of the mooring system is provided in Figure 6.7.

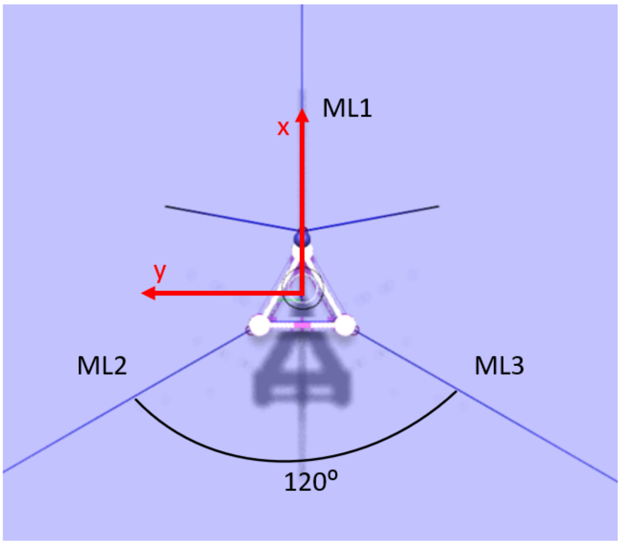

Figure 6.7: Overview of the mooring system.

The water depth is set to 100 m, as described in Section 5. The base case mooring system consists of only studless chain mooring lines with one dimension from the anchor to the fairlead connection point on the floater. The position of the connection points on the floating substructure is given in Table 6.6. All the mooring lines are connected at the water line in still water.

Table 6.6: Placement of the fairleads on the Semi-body in the SIMA models.

	X (m)	Y (m)	Z (m)
Fairlead1	42.72	0	0
Fairlead2	-21.36	37	0
Fairlead3	-21.36	-37	0

Drag coefficients for the mooring lines are assigned in accordance with DNV-OS-E301 [39]. This also applies to the effective elastic modulus of the mooring lines, for preliminary design, this is given by Equation 6.12 [39]:

$$(6.00 - 0.0033d) \cdot 10^{10} N/m^2 \tag{6.12}$$

where d is the chain diameter in mm.

Dimensions and characteristic properties for the mooring chain are taken from the hardware catalogues by Ramnäs [59]. Here the suggested ratio of weight in air to weight in water is also given with a value of 0.87, this account for the buoyancy of the chain. An initial mooring line length of 700 m has been used in the base case mooring system.

The pretension of the system was decided by balancing a desired natural period of the system in surge between 90-100 seconds and the maximal offset of the system during extreme load. The extreme load was calculated as an overestimate of the mean load combination from the thrust force generated by the turbine and the 50-year value from the current velocity. The force from the current was calculated as a Morison drag force with contributions from the pontoons and columns. The calculated mean force was then multiplied by a factor of 1.5 to ensure consideration of sufficient loads which resulted in an estimated load of 3500 kN.

The Properties of the base case mooring lines are given in Table 6.7

Table 6.7: Preliminary mooring system properties.

Property		
Line type	Studless chain	R5
Chain diameter	167	[mm]
Breaking strength	19 056	[kN]
Weight in air	558	[kg/m]
Elastic modulud, EA	5.5396e+10	[N/mˆ2]
Length	700	[m]
Transverse drag coefficient	2.4	[-]
Friction coefficient	1.0	[-]
Pretension	1400	kN

For the RIFLEX-model the desired pretension is achieved by adjusting the position of the super node representing the anchor positions. The anchor positions are found through the catenary equations as described in Section 3.3 and are given in Table 6.8.

Table 6.8: Base case anchor positions for the RIFLEX-model.

	X (m)	Y (m)	Z (m)
Anchor 1	742.72	0	-100
Anchor 2	-371.36	643.22	-100
Anchor 3	-371.36	-643.22	-100

The external area used in cross-section properties defined in the RIFLEX-model is found through the following relation:

$$Ext.Area = \frac{w_{air}(1 - 0 - 87)}{\rho g} \tag{6.13}$$

where w_{air} is the weight in air of the mooring chain. The restoring curves for the two models with the preliminary mooring system is found through a load-displacement study and are presented in Section 7.2.

6.3 Implementation of the SyROPE-Model in SIMA

SIMA supports the use of non-linear fibre rope models such as the SyROPE-model which models both the static and dynamic elastic stiffness of the fibre ropes. It is assumed that the fibre ropes are sufficiently pre-stretched such that work is done along the working curve during simulations. Due to the behaviour of the fibre ropes, the simulation procedure needs to be separated into two parts, as follows:

1. Mean non-linear static tension in all mooring lines is calculated during the static analysis. Hence, it is required that all mean environmental forces are included in the static analysis in SIMA.
2. The dynamic analysis can then be executed using the mean non-linear static tension as the basis for the linear dynamic tension applied in the dynamic analysis.

The mean aerodynamic thrust force from the turbine during production or idling is included as a body force acting in the centre of the nacelle body in line with the wind direction. This force contribution is ramped down during the first 100 seconds of the dynamic analysis, during the start-up of the wind turbine.

7 Quality Analysis - Model Verification

A range of simulations has been run to assure that the models with the preliminary mooring system behave as expected for a system of such configuration. This has been verified through decay tests, constant wind tests, and regular wave responses. The following sections will present and discuss various results obtained from the simulations. Results presented in *"Definition of the INO WINDMOOR 12 MW base case floating wind turbine"* [57] are used for comparison and is referred to as the reference model.

Further, a parameter convergence check for the Gumbel distribution has also been performed to establish the required number of simulations needed to reach convergence in the statistical parameters for the distribution of maximum line tension.

7.1 Decay Simulations

Decay simulations have been performed to document the natural periods of the system. The initial displacement of the system is achieved by applying a ramp force, followed by a constant force, which is then released as illustrated in Figure 7.1. The setup specifications for each decay simulation are given in Table 7.1. During the decay simulations, the wind turbine is set to parked condition, meaning that the turbine blades are pitched 90°. This ensures that the rotor does not start to rotate during the simulations which may have an influence on the results.

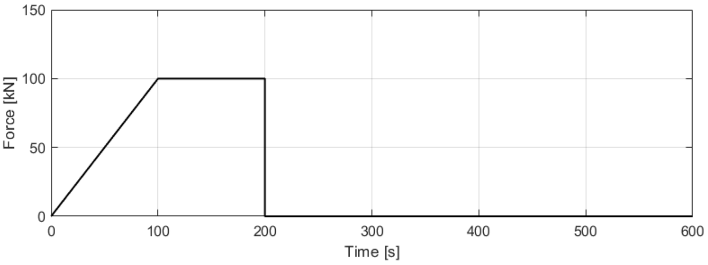

Figure 7.1: Example of decay force with a ramp duration of 100 s and a constant force duration of 100 s.

Table 7.1: Simulation parameters for the decay simulations.

Motion	Force/Moment	Simulation length (s)	Ramp duration (s)	Constant force duration (s)
Surge and Sway	1700 kN	1400	100	200
Heave	10 000 kN	600	50	100
Pitch and Roll	220 000 kNm	800	100	100
Yaw	10 000 kNm	1200	100	100

Time-series of the decay simulations for each degree of freedom for both the SIMO- and RIFLEX-model is presented in Figure 7.2. Calculated natural periods from the corresponding time series are given in Table 7.2

Table 7.2: Rigid-body natural periods, obtained from decay simulations with the SIMO- and RIFLEX-models.

	Surge	Sway	Heave	Roll	Pitch	Yaw
Reference model nat. period [s]	97.3	98.0	16.3	29.5	31.4	88.0
SIMO-model nat. period [s]	93.6	94.6	16.2	31.7	32.1	82.0
RIFLEX-model nat.period [s]	94.2	95.2	16.3	28.4	30.7	84.9

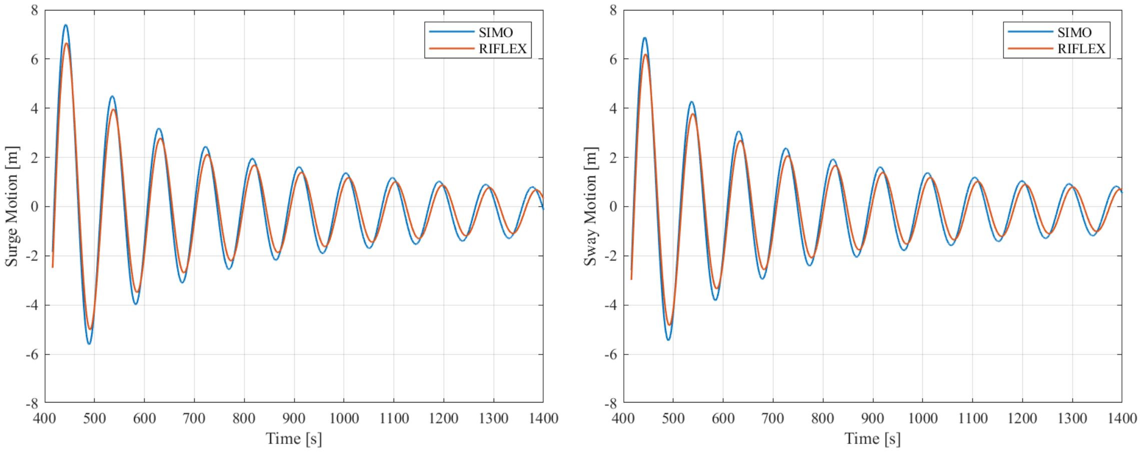

(a) Surge (b) Sway

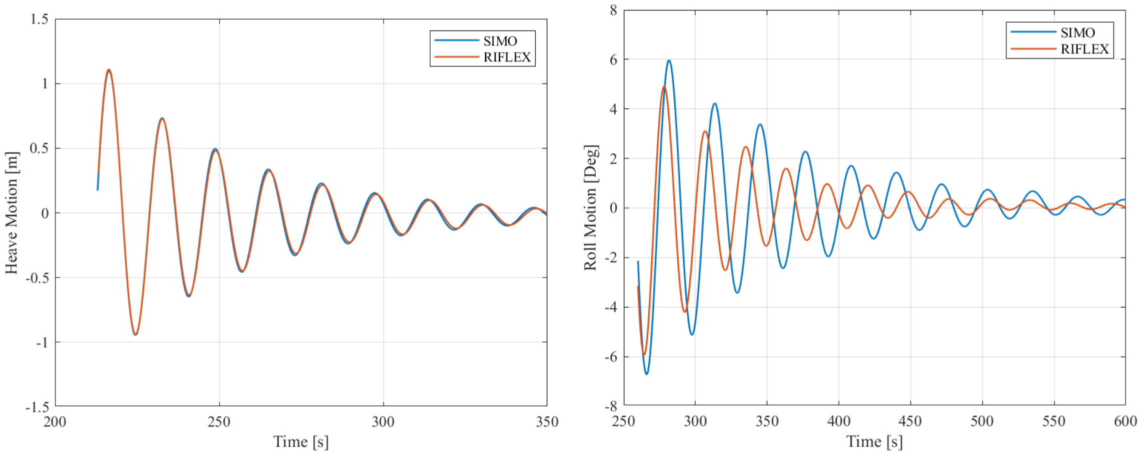

(c) Heave (d) Roll

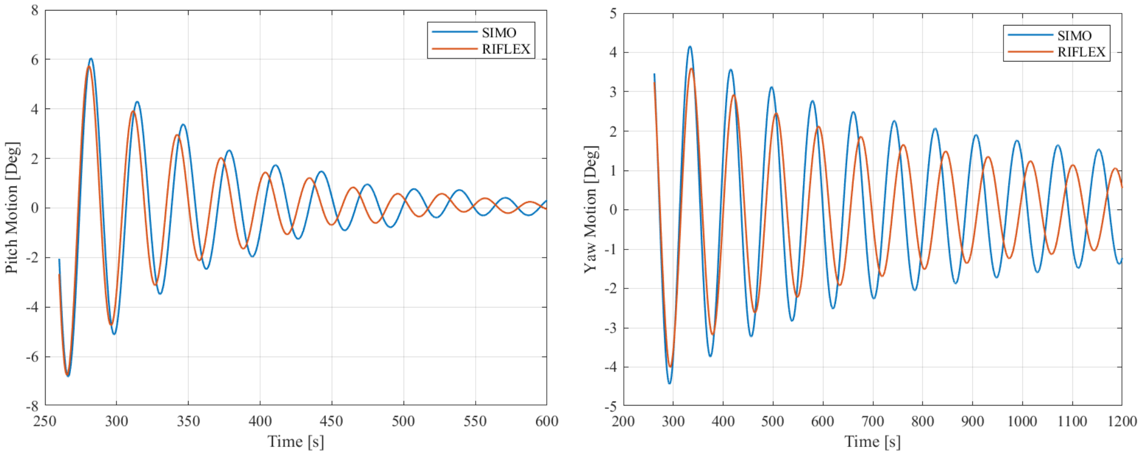

(e) Pitch (f) Yaw

Figure 7.2: Time series of decay simulations for all FWT rigid body motions.

The obtained natural periods for the structure are in the expected range for a structure of this size and configuration. The natural periods in surge, sway, and yaw are dependent on the configuration of the mooring system and is in the desired range between 90-100 seconds. These periods may be changed by altering the parameters of the mooring system. However, this may compromise the maximum offset or make the system too stiff.

The natural period in heave is almost identical for the two models and is also identical to the heave natural period of the reference model. This indicates that the catenary mooring system has a low influence on the vertical motion of the system. This is consistent with the expected behaviour, as the mooring system is designed to provide stiffness in the horizontal plane. Figure 7.2c of the heave decay shows that the heave motion is damped out in a relatively short period indicating a reasonable amount of damping of the heave motion.

Some difference between the natural periods in surge and sway is found for the SIMO- and RIFLEX-model. The main reason for this is believed to be differences in the definition of the mooring system. For the SIMO-model the anchor positions are calculated by SIMA with the desired pretension as input parameter, while in RIFLEX the anchor positions are given directly as input. This may result in a small difference in the anchor positions, and consequently, the pretension and stiffness of the system. This is further confirmed by the mooring system restoring curves discussed in Section 7.2. Furthermore, the added mass contributions from mooring lines will give a larger mass to the system which generally results in an increase in the natural period. The difference between the two models is quite marginal and an equal behaviour of the motions can be observed for the two models. The time series of the surge and sway decays in Figure 7.2a and 7.2b shows that the RIFLEX-model obtains a smaller motion amplitude than the SIMO-model. This is due to contributions from drag and inertia forces acting on the mooring lines. However, the difference in amplitude is not significant and it becomes less prominent further out in the time series. This can be explained by the relatively low velocity of the FWT resulting in low drag contributions.

A larger difference between the two models can be observed for the roll and pitch motions, both in the calculated natural periods and in the decay time series. Starting with the roll motion, a 10% difference in the natural period is found between the two models. One explanation for this may be in the modelling of the two models as described in Section 6.2.1 in the mass and inertia input values. Due to the added inertia from mooring lines in the RIFLEX-model it would be expected that this model should have a higher natural period. However, this is not the case which indicates a possible difference in the mass-moment of inertia or stiffness. Further, from Figure 7.2d the effects of drag forces acting on the mooring lines are clearly visible from the faster decrease in roll amplitude for the RIFLEX-model. For the pitch motion, the difference in the natural period is down to 5%, again believed to be due to modelling differences. The natural period in roll and pitch for the RIFLEX-model are both lower than the periods given for the reference model, this is mainly caused by a higher mooring weight in the RIFLEX-model resulting in a higher stiffness.

For the yaw motion, some deviation is observed between the two models. However, this is in compliance with the difference observed for the surge and sway motion and is believed to be caused by small differences in mooring stiffness and the inertia forces from the mooring system. Again the RIFLEX-model shows signs of higher damping indicated by the lower motion amplitudes in the time series in Figure 7.2f. The calculated natural period for yaw is in the expected range for both models.

7.2 Mooring System Load-Displacement Study

A load-displacement study, also known as pull-out tests, is done to establish the restoring curves of the preliminary mooring system in the surge direction. Due to the arrangement of the mooring lines, the restoring curve is expected to be dependent on the direction of the environmental loading. Thus, the restoring curve is established for forces acting in both in-line and in-between directions. The simulation procedure is similar to the one used during the decay simulations, however, without the release of the constant force. The mean position of the FWT throughout the duration of the constant force represents the offset of the FWT for that force magnitude. The resulting restoring curves are presented in Figure 7.3.

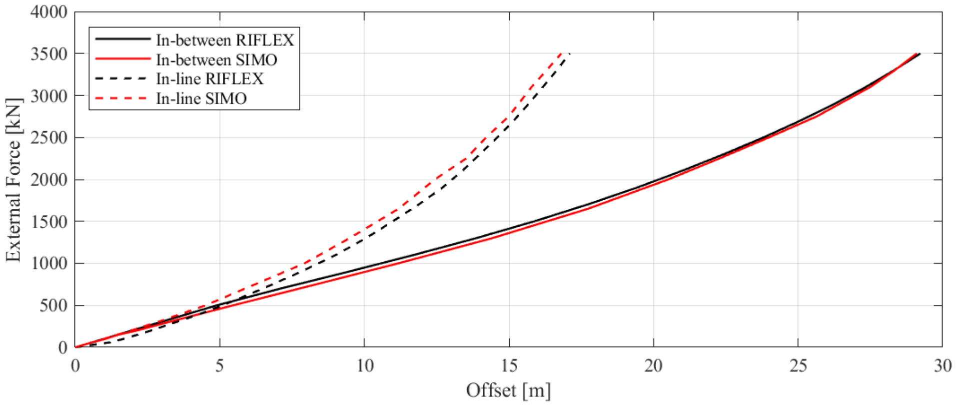

Figure 7.3: Restoring curves for external loading acting in-line and in-between mooring lines.

Figure 7.3 shows that the mooring system has, as expected, a softer behaviour for forces acting in positive x-direction according to the defined coordinate system in Figure 6.3. The FWT attain an offset just above 29 m when exposed to an external load of 3500 kN acting in the in-between direction. A mean load of this magnitude is regarded as a conservative estimate implying that an offset larger than 30 m is an unlikely event for a system of this configuration. Current offshore rules and standards for FWTs do not prescribe compulsory values for maximum allowable displacements, only that the mooring system should keep the wind turbine in position such that it can generate electricity and maintain the transfer of that electricity to a receiver. Data regarding admissible offset is available in several sources of literature. In the work done by Benassai et al. [60] during design optimisation of a catenary mooring system for FWTs, an admissible offset of 10 m is used for various water depths, between 50 and 300 m. While in the optimisation study done by Brommundt et al. [61] a much larger value is found with an admissible offset of 32.01 in 75 m water depth. This variation of admissible offset suggests that an offset between 20 to 40 % of the water depth should be a reasonable operational range for a FWT in European waters. Hence, the restoring capabilities of the preliminary mooring system for in-between loading are regarded as adequate. This also applies to the restoring curve for in-line loading which is well below this range. Some differences in the restoring curve can be observed for the two models which are believed to be caused by a small difference in mooring line pretension. The two restoring curves in Figure 7.3 can be combined to generate a complete restoring curve in surge for the preliminary mooring system, as shown in Figure 7.4.

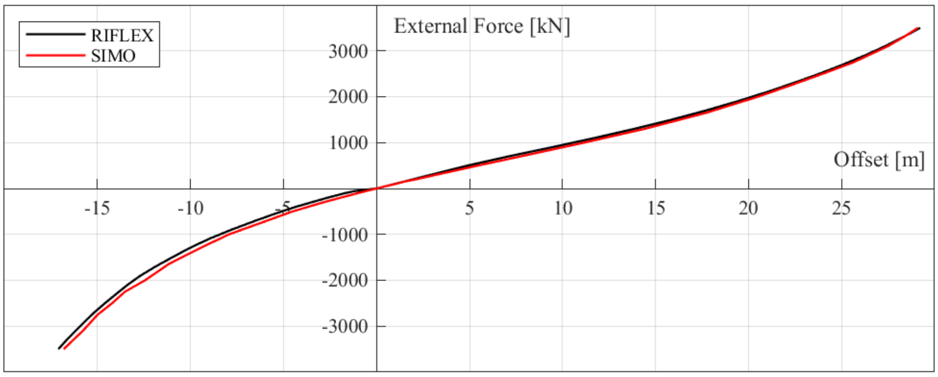

Figure 7.4: The complete restoring curve in surge for the preliminary mooring system.

7.3 Constant Wind Simulations

The constant wind simulations are used for assessing the performance and behaviour of the wind turbine at different wind speeds. In addition, the mean platform motions are investigated to ensure that the system has an expected behaviour at the various wind speeds. No waves or current is applied during the simulations, just a variation in mean wind speed. The variation in mean wind speed is given through a two-component wind file including the direction and speed of the wind. The mean wind speed in the file ranges from the cut-in speed up to the cut-out speed of the wind turbine, as illustrated in Figure 7.5. Each wind speed has a duration of 900 seconds to ensure a steady state of the turbine during each wind step. The wind turbine has to start from a standstill, hence, the duration of the first wind speed is 600 seconds longer to assure a proper start-up of the turbine.

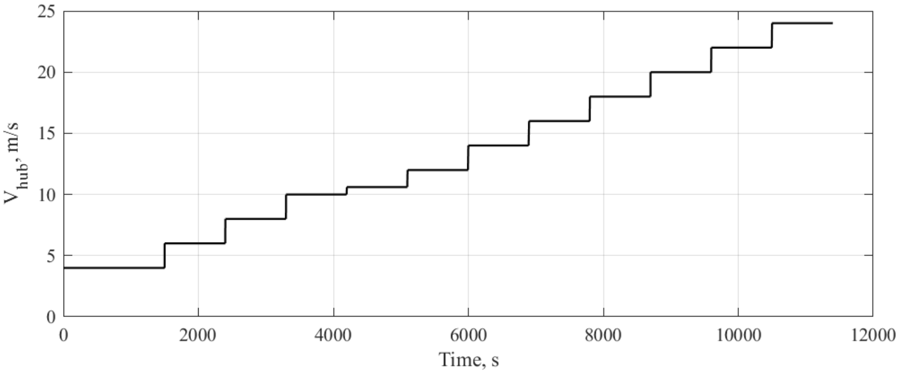

Figure 7.5: Illustration of the variance in mean wind speed given by the wind input file.

Mean value results for the wind turbine performance for both the SIMO- and RIFLEX-model are presented in Figure 7.6. Figure 7.6a shows the mean value for rotor RPM, blade pitch angle, and torque. The rotor RPM and generator torque develop as expected with the increasing wind speed. The rotor RPM remains at a constant value after the rated wind speed of 10.5 m/s is reached. After reaching the rated wind speed the controller is programmed to achieve constant torque through pitching of the turbine blades, this can be observed by the change in blade pitch angle after a wind speed of 10.5 m/s. At rated wind speed the relative wind speed experienced by the wind turbine will alter between the below rated and above rated regimes due to the motions of the FWT. This alteration in operation regimes may cause the turbine to underperform at rated wind speed, as observed in the performance curves between 10.5 m/s and 12 m/s. Some differences in the blade pitch angle are observed between the two models. The blade pitch angle for the RIFLEX-model has a lower value during the above rated wind speeds, assumed to be due to modelling differences in the turbine setup between the two models. This is also believed to be the reason for the difference in thrust force shown in Figure 7.6b. However, the thrust force at rated wind speed and up to the cut-out wind speed is nearly similar for both models. The DLCs listed in Section 5.2 is focused on this operational area where the two models have obtained equal results. Thus, it is assumed that the small difference in thrust force at below rated wind speeds will not have a significant influence on the results. The generator power follows the same shape as the torque in Figure 7.6a and flattens out at 12 MW which is the rated power of the wind turbine.

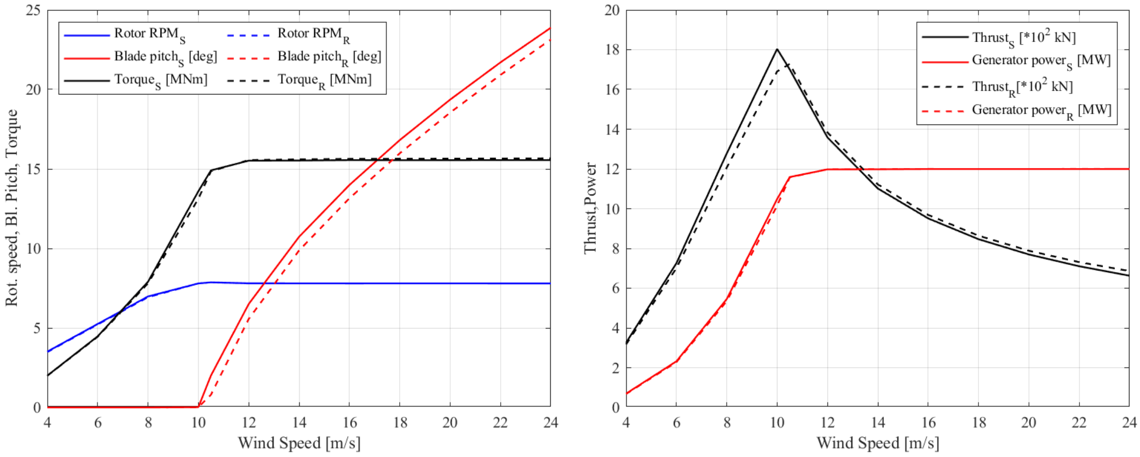

(a) (b)

Figure 7.6: Wind turbine performance plots for rotor RPM, blade pitch angle, and generator torque (a). Wind turbine thrust and generator power are given (b). Subscript S and R is for the SIMO- and RIFLEX-model respectively.

Figure 7.7 shows the mean surge, pitch and roll motion experienced by the FWT during the constant wind simulation for both the SIMO- and RIFLEX-model. As expected the surge and pitch motions follow the thrust curve in Figure 7.6b, with the largest displacement occurring at maximum thrust force. Further, Figure 7.7 shows that the FWT acquires a small roll angle during all wind speeds with the highest roll angle occurring at the rated wind speed. This roll angle is caused by the torque moment generated by the rotational motion of the rotor.

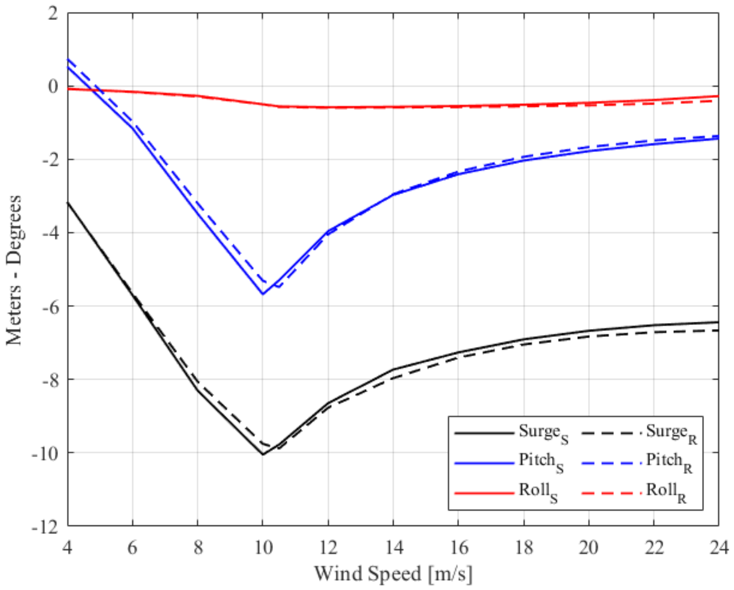

Figure 7.7: Mean surge, pitch, and roll motion during constant wind simulation. Subscript S and R is for the SIMO- and RIFLEX-model respectively.

7.4 Regular Wave Response

The hydrodynamic characteristics of the two models with the preliminary mooring system are documented through Response Amplitude Operators (RAO) which are established through a series of regular wave simulations. The regular wave simulations are done with a wave amplitude of 1 m with periods ranging from 2 s to 35 s to cover expected resonance periods. The reference point of the investigated motions is taken at the origin of the coordinate system as shown Figure 6.3. RAOs from the regular wave simulations for motions in surge, heave and pitch are presented in Figure 7.8 for both the SIMO- and RIFLEX-model. Additionally, for comparison, the figure contains the RAOs calculated from the WAMIT hydrodynamical analysis in [57].

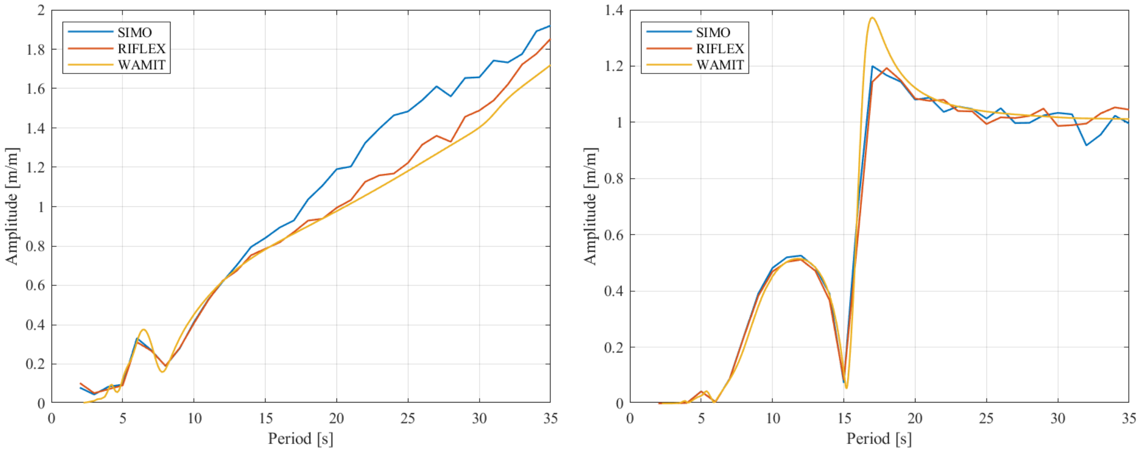

(a) Surge (b) Heave

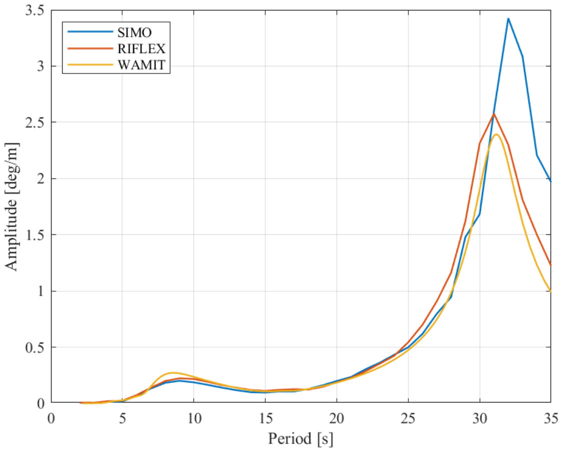

(c) Pitch

Figure 7.8: Response amplitude operators for surge (a), heave (b), and pitch motion (c) in regular waves for the SIMO- and RIFLEX-models compared with WAMIT results from [57].

The three graphs in Figure 7.8a generally show an equal behaviour for the surge motion. The curve for the RIFLEX-model follows the WAMIT curve quite well, particularly for periods lower than 20 seconds. Theoretically, the surge motion of a freely floating structure in long waves will tend to follow the elliptical trajectory of water particles at finite water depths. The amplitude of the water particle trajectory can be written as $\zeta_a/tanh(kh) \approx A/kh$, where ζ_a is wave amplitude, k is wave number and h is water depth [62]. Given that the wave amplitude stays the same, the motion amplitude will increase with decreased water depth. The water dept used in the WAMIT analysis is 50 m deeper than what is specified in the regular wave simulations, this may be the main cause of the observed difference in surge motion between the RIFLEX-model and the WAMIT curve at higher periods. Further, Figure 7.8 shows that the SIMO-model has a larger deviation from the WAMIT curve in surge motion. This is explained by both the difference in water depth and by the exclusion of hydrodynamic contributions from mooring lines in the quasistatic approach resulting in lower damping of floater motions.

For the heave motion in Figure 7.8b there is a very equal behaviour between the three graphs. A small difference in the peak value at a period of 16 seconds between the WAMIT-curve and the two models can be observed. This difference is believed to be caused by the damping contribution from the Morison drag elements included in the two models. WAMIT only accounts for potential flow and not viscous damping, hence, larger damping of the heave motion is achieved for the two SIMA-models. The SIMO- and RIFLEX model has close to equal behaviour in heave motion, an expected result since contributions from the mooring system generally has a low affect on the behaviour of a floating structure in heave. Finally, the heave RAO is observed to reach the theoretical value of unity at higher wave periods i.e. longer wavelengths. The natural period in heave is found to be 16.3 s which is in the typical wave period regime. This is not ideal due to a high possibility of waves exciting heave resonance response which may lead to substantial motions of the FWT. However, the RAO for the heave motions shows that the floater has quite an adequate damping in heave and thus justifies the unfavourable heave natural period.

Results for the pitch motion in Figure 7.8c shows no significant deviation between the three graphs for periods below 30 seconds. Above a wave period of 30 seconds, the SIMO-model is observed to reach a higher peak value at the pitch natural frequency. This is again believed to be connected with the distinct difference between the quasi-static and dynamic approaches. The RIFLEX-model obtains almost identical results to the WAMIT analysis.

The resulting RAOs from the regular wave simulations confirm the hydrodynamical proprieties for the two models generated in SIMA and show an expected behaviour for the investigated motions. Furthermore, peak values observed in the heave and pitch RAOs correspond well with the natural periods found in the decay simulations from Section 7.1.

7.5 Seed Convergence Study

A seed convergence study has been performed to ensure that the statistical properties of the Gumbel distribution have reached convergence. As stated in Section 4.6.2, it is recommended to run 10-20 3-hour realisations to attain adequate statistics for the MPM-value used in mooring design. However, due to time considerations, the simulations are done with 1-hour realisations for work done in this project. As a result of this, the total number of global maxima from one simulation will be reduced by approximately $\frac{1}{3}$. Figure 7.9 illustrates the effect the inclusion of larger sample size, N, has on the extreme value distribution. As N increases, the extreme distribution can be seen to move towards higher values and become more narrow. Assuming that the full process is Gaussian distributed, the most probable largest amplitude among N global maxima can be found by:

$$X_{max,N} = \sigma\sqrt{2ln(N)} \tag{7.1}$$

By investigation of acquired time series from performed simulations the number of global maxima from one 1 hour simulation is found to be in the range 10500 to 11000. The ratio between a 1 hour and a 3 hour simulation is hence:

$$\frac{X_{max,1-hour}}{X_{max,3-hour}} = \frac{\sqrt{ln(N)}}{\sqrt{ln(3N)}} = \frac{\sqrt{ln(11000)}}{\sqrt{ln(3 \cdot 11000)}} = 0.95 \tag{7.2}$$

The most probable largest response may thus be under predicted by 5% due to this reduction in simulation time and should be kept in mind when reviewing the results.

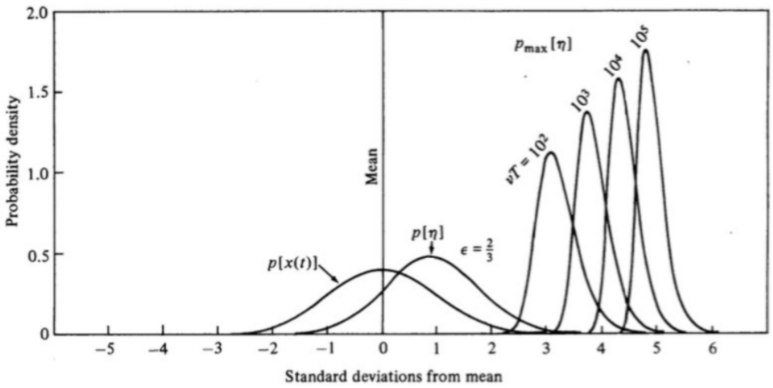

Figure 7.9: Gaussian distribution with Rice distribution of individual global maxima and extreme value distribution for an increasing number of global maxima [30].

DLC 6.1 with environmental forces acting in-line is used during the convergence study. This is due to larger variations in the observed maximum line tension during this condition, caused by the extreme environmental loading. To confirm that the Gumbel distribution is a well-suited model for the largest maxima a Gumbel probability paper has been constructed and is presented in Figure 7.10.

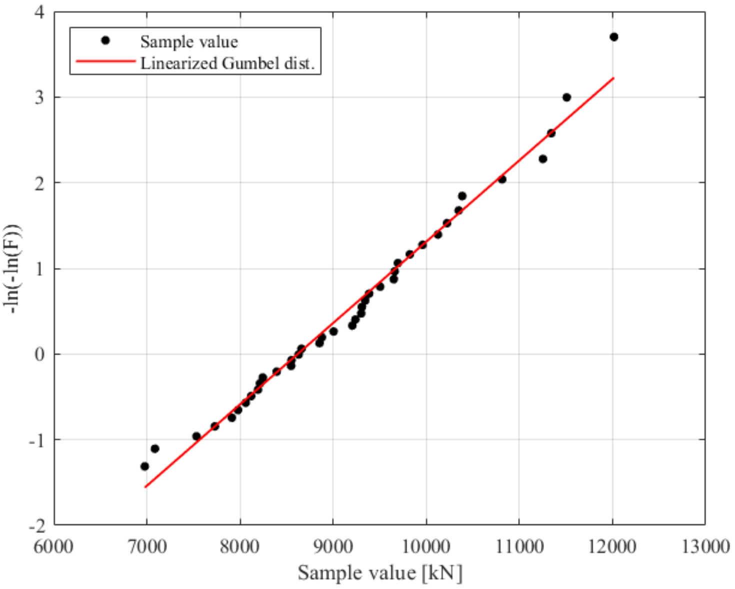

Figure 7.10: Gumbel probability paper for largest mooring line tension during DLC 6.1 in-line, using the SIMO-model.

The Gumbel probability paper presented in Figure 7.10 shows that the collected individual largest maxima of the mooring line tension largely follow the linearized Gumbel distribution. Hence, the Gumbel distribution is found to be a good statistical model for the largest maximum of the mooring line tension.

As stated in Section 4.7.1, the Gumbel distribution has two parameters. For the purpose of this convergence study, it is a convergence of the location parameter that is wanted. The location parameter is the same as the MPM-value which is directly used in the calculation of mooring design tension, hence, a convergence of this parameter is most significant for mooring design. A total number of 40 wave seeds has been run for the purpose of this study, giving 40 different realisations of the wave process. The resulting location parameter value and Gumbel distribution for an increasing number of seeds are presented in Figure 7.11a and 7.11b respectively.

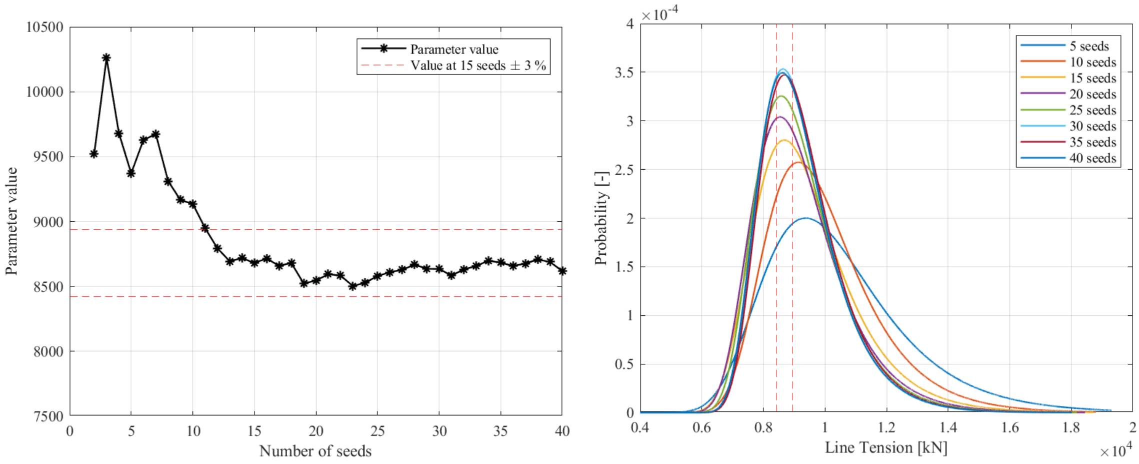

(a) (b)

Figure 7.11: Location parameter convergence plot (a) and Gumbel probability density function for increasing sample size (b).

Figure 7.11a shows a large fluctuation in the calculated parameter value for the first ten seeds of the simulation, indicating a large variance in the registered maximum line tension between the different seeds. Further, after the inclusion of 13 seeds the parameter value shows signs of converging and remains at approximately the same level after the inclusion of the remaining seeds. The red dashed lines in Figure 7.11a and 7.11b marks a 3 % positive and negative deviation from the parameter value at 15 seeds. This shows that the change in parameter value keeps within a 3 % window after 15 realisations of the load case. Furthermore, the Gumbel distribution in Figure 7.11b shows that the change in width of the distribution curve are small after 15 seeds. This indicates that also the shape parameter of the distribution has started to converge at the inclusion of 15 seeds. Hence, on the basis of the results presented in Figure 7.11 it is concluded that 15 realisations of the wave process are sufficient for ensuring convergence of the statistical properties used in the design tension calculations.

8 Investigated Mooring Configurations

The investigated mooring configurations covered in this thesis are illustrated in Figure 8.1 and briefly described in Table 8.1, while detailed properties for the mooring lines are given in Table 8.2. Five synthetic fibre rope mooring systems of tout configuration have been considered (System II-VI) in addition to the initial chain mooring system of catenary configuration (System I). Four of the synthetic systems consist of polyester lines while one system has lines made out of nylon. All the synthetic fibre rope systems are built up by three lines with a 120°spacing at 100 m water depth, equal to the catenary mooring system.

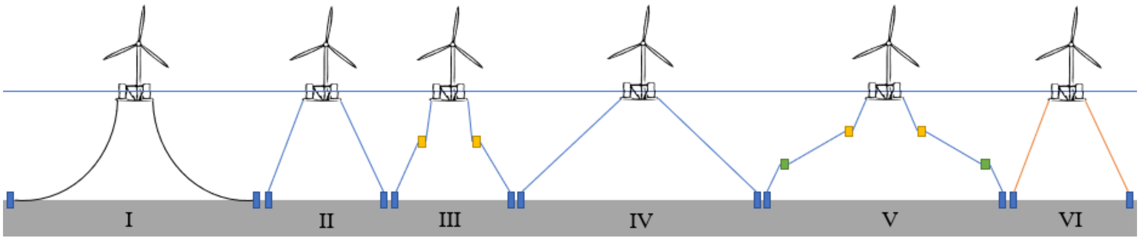

Figure 8.1: Illustration of the investigated mooring configurations.

System II is the initial synthetic mooring system and is mainly based on System I for the definition of line length and pretension. This system is however expected to be quite stiff due to the short line length and material properties of polyester. To reduce the horizontal stiffness of System II, the lines in Systems III have been fitted with clump weights with the intention of increasing the angle between the mooring line and the water surface, hence, changing the horizontal stiffness properties of the system. Furthermore, the pretension of the lines has been reduced to further reduce the stiffness. For System IV the line length is increased such that a surge natural period of around 50 seconds is achieved without the use of clump weights. The necessary line length for System IV was found by evaluating the required horizontal stiffness to obtain a natural period of 50 s. This stiffness was used in the linear relationship, $k = \frac{EA}{L}$ to find the needed line length, also taking into account the top angle of the line. This system is further developed into System V where weights are added for the same purpose as for System III, and buoys are included to prevent the fibre rope from touching the seabed. The Final system, System VI, is again based on System II but here the polyester fibre ropes are replaced with nylon ropes to investigate possible advantages the softer nylon ropes have.

Table 8.1: Brief description of the mooring system configurations.

System nr.	System description
I	Preliminary chain mooring system as described in Section 6.2.2.
II	Pure polyester fibre rope system without buoy or clump weight components.
III	Based on System II, with the inclusion of clump weights 200 m from the fairlead.
IV	Pure polyester fibre rope system with longer lines compared with System II.
V	Based on System IV, with the inclusion of clump weights 300 m from fairlead and buoys 300 m from anchor.
VI	Pure nylon fibre rope system without buoy or clump weight components.

Parameters for the synthetic fibre ropes are according to values found in Bridon hardware catalogue [24] for Superline Polyester and Superline Nylon OCIMF 2000. The parameters used for the nylon rope are linearly interpolated due to the limited MBS range for the nylon ropes, a MBS equal to the one used for the polyester lines is assumed to find appropriate values. The anchor radius is the distance between the centre of the platform and the anchors. The SyROPE-model, as described in Section 3.4, is implemented in SIMA to describe the static and dynamic stiffness properties of the synthetic fibre ropes.

Table 8.2: Mooring line main properties.

System nr.	Length (m)	Diameter (mm)	Anchor radius (m)	MBS (kN)	Mass in air (kg/m)	Clump (t)	Buoy (m^3)	Pretension (kN)
I	700	167	711.4	19056	558	-	-	1400
II	700	268	746	19620	46.4	-	-	1400
III	700	268	740.7	19620	46.4	25	-	1200
IV	1250	268	1305	19620	46.4	-	-	1250
V	1250	268	1305	19620	46.4	25	9.76	1600
VI	700	315	798.1	19620	65.4	-	-	1550

9 Results and Discussion

Results from the time-domain simulations will in the following sections be presented and discussed. Firstly, the results from the wave contour and spread weather analysis are presented to establish the environmental parameters which result in the highest mooring lines tension. Thereafter, the results are presented in two parts where results are first presented for the chain mooring system where the quasi-static and fully dynamic approach is compared. The next part presents results for all investigated mooring systems with the main focus being on the synthetic fibre rope mooring systems. Results are presented through statistics and dynamic responses of the FWT motion response and mooring line top tension, followed by design tension and utilization factor calculations.

9.1 Wave Contour and Non-Collinear Weather Analysis

Simulations for the wave contour and spread weather load cases were performed with the SIMO-model only with the chain mooring system. The objective of the simulations was to establish the environmental parameters that resulted in the highest mooring line design tension for use in DLCs for further simulations. Due to the configuration of the mooring system, the highest mooring tension is expected to occur when environmental forces are acting inline with one of the mooring lines. Hence, the wave contour simulations are performed with environmental forces acting towards 180° when referring to the FWT coordinate system i.e. inline with mooring line number one. For the spread weather analysis, both inline and in-between direction has been controlled. Figure 9.1 provides an illustration of the direction applied to the environmental forces in relation to the FWT mooring and coordinate system.

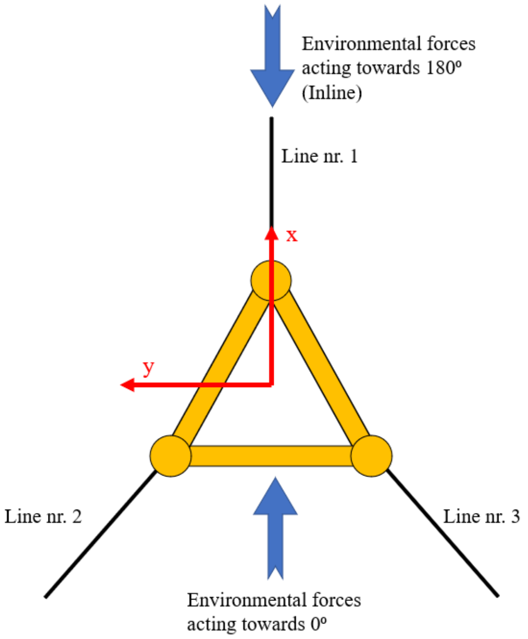

Figure 9.1: Illustration of the direction of the environmental forces in relation to the FWT coordinate and mooring system.

9.1.1 Wave Contour

Results for design tension and utilization factor from five H_s and T_p combinations are presented in Table 9.1. Results show that a higher T_p value is disadvantageous for the resulting design tension. A higher T_p value results in longer waves and consequently a larger dynamic motion of the FWT in surge direction which is the main contributor to increased tension in a catenary mooring system.

However, the largest design tension is found for the case with the highest H_s value, indicating the significance of the increased energy from the higher waves. The load case with a H_s and T_p value of 13.5 m and 18 s, respectively, is thus used further in the ULS simulations as input for DLC 6.1.

Table 9.1: Design tension and utilization factor for mooring line number 1 for various H_s and T_p values representing the 50-year contour line.

	Wave parameters									
	H_s	T_p	H_s	T_p	H_s	T_p	H_s	T_p	H_s	T_p
	12 m	14.6 s	13 m	16.1	13.5 m	18 s	13 m	19.3 s	12 m	20.1 s
T_d [kN]	9518		10771		13813		12155		11432	
UF	0.50		0.57		0.72		0.64		0.60	

The FWT motion response was also controlled during the wave contour analysis, in addition to tension and resulting design tension values. When studying the obtained yaw motion of the FWT a yaw instability was found, as shown in the time-series in Figure 9.2a taken from the condition with $H_s = 13.5$ m and $T_p = 18$ s for 40 different wave seeds. The time series shows that FWT reaches a mean yaw angle of around 18-20° with quite large fluctuations between 0° to just above 30°. Furthermore, at around 3000 seconds, a complete change of yaw angle position can be observed for some of the simulations of the condition. The mean yaw angle changes from positive 20° to negative 20° during a relatively short time window. The mechanics behind this behaviour are described in Section 4.11.2. To mitigate this behaviour of the FWT during extreme load cases the turbine RNA is given a yaw angle of -20°. This causes the aerodynamic yaw moment generated by the RNA to be consistent in one direction and thereby avoiding a large change in the FWT yaw angle. The large fluctuations in the yaw angle are also reduced when the yaw of the RNA is introduced. Figure 9.2b shows the resulting times series of the FWT yaw motion when the yaw angle of the RNA is incorporated. Due to these discoveries, a 20° yaw angle is given to the turbine RNA during extreme load cases.

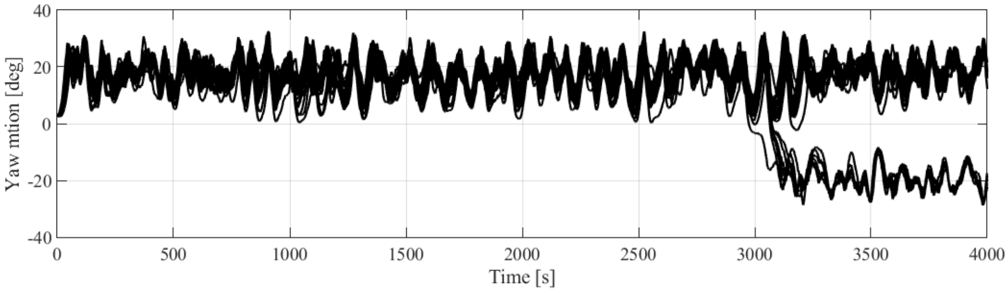

(a)

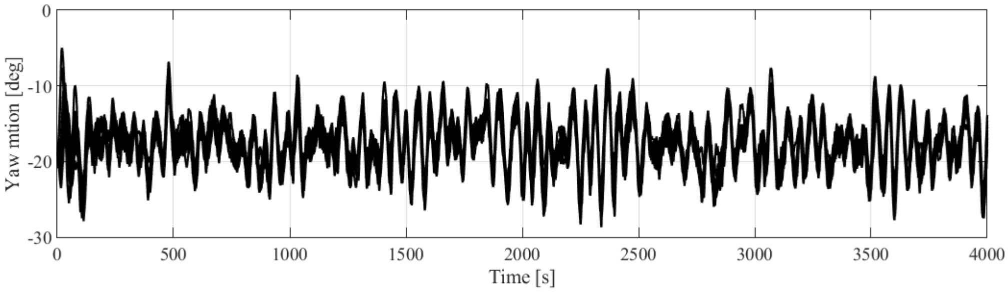

(b)

Figure 9.2: Observed yaw instability during wave contour analysis (a), and yaw motion of the FWT after a 20° yaw is assigned to the wind turbine RNA (b). Times series from simulation with $H_s = 13.5$ m and $T_p = 18$ s.

9.1.2 Non-Collinear Weather

Table 9.2 summarises the results for design tension obtained during collinear and non-collinear weather conditions. Directions given to the various environmental parameters are described in Section 5.2. Results show that a collinear environment gives a higher design tension for cases where the environmental forces act in a direction of 180° compared with a non-collinear environment in the same main direction. The opposite is found when the direction of the environmental forces is turned to 0°, acting in-between mooring lines 2 and 3. For the collinear case, the forces are more or less evenly distributed between the two mooring lines, thus obtaining a design tension of near equal magnitude. For the non-collinear case, the two lines obtain quite different design tension values, particularly during DLC 1.6 where mooring line 3 has nearly double the value found for mooring line 2. Both DLC 1.1 and 1.6 are load cases where the wind turbine is operational and thus generates thrust force, with the largest thrust force being generated during DLC 1.6 as this is at rated wind speed. This is reflected in the difference in calculated design tension between mooring lines 2 and 3 which is the largest for DLC 1.6. In DLC 6.1, when the wind turbine is in idle condition, the difference in design tension between the two lines is reduced. As the highest design tension value is found during the collinear condition with environmental forces acting towards 180° it is decided to use a collinear environment for further simulations for all DLCs. As the governing ULS load case will be one with environmental forces acting towards 180° the larger magnitude of the design tension value found during the non-collinear environment acting towards 0° is not regarded as critical.

Table 9.2: Design tension [kN] for windward lines during collinear and non-collinear conditions. The direction given for the non-collinear cases refers to the wave direction.

	Collinear - 180°	Non-collinear - 180°	Collinear - 0°		Non-collinear - 0°	
DLC	Line 1	Line 1	Line 2	Line 3	Line 2	Line 3
1.1	4533	4527	3380	3275	2699	3812
1.6	7511	6935	4810	4961	3074	5893
6.1	13813	11425	5868	5705	4757	6416

9.2 Chain Mooring System

The following sections will focus on results obtained for the chain mooring system, named system I. ULS load cases have been run for both the SIMO- and RIFLEX-model and results for both models will be presented and compared. DLC 1.1R is not considered in the results presented in this section as this has not been run for the SIMO-model. Firstly, response statistics are presented, followed by dynamic responses. Finlay, design tension and utilization factors are presented.

9.2.1 Motion Response Statistics

The motions that are the main contributors to the excitement of mooring line tension are surge, heave, and pitch. This, in addition to the symmetric configuration of the floater and environmental forces mainly acting in the symmetric plane which leads to negligible sway and roll motions, gives reasoning for largely focusing on surge, heave, and pitch motion in this section.

The mean value, standard deviation, and MPM-value of the surge motion are presented in Figure 9.3 for all relevant load cases for both 180° and 0°. Generally, it is not expected to observe large deviations between the motions obtained for the SIMO- and RIFLEX-model as the main difference between the two is the calculation procedure of the mooring system forces. This anticipation is reflected in the results shown for the surge motion in Figure 9.3.

Statistical properties of the surge motion are generally quite equal for the two models. A small exception is the statistical properties obtained for the surge motion during DLC 6.1. Here the RIFLEX-model is found to experience a larger mean offset in surge, particularly for DLC 6.1 acting in 0°. For this loading condition, the MPM-value of the surge motions is also found to be larger for the RIFLEX-model. One reason for this is that the mooring system for the RIFLEX-model is found to be somewhat softer. However, from the restoring curve in Figure 7.3 the difference in restoring force between two models is marginal for forces acting in 0°. When investigating the yaw motion of the two models during DLC 6.1 acting towards 0° the SIMO-models is observed to reach a larger positive mean yaw angle than the RIFLEX-model. This reduces the tension acting in line 2 which in turn allows for larger sway motions of the floater which is further confirmed from the time series of the FWT sway motion. The larger yaw motions of the SIMO-model may be the result of not including damping contributions from the mooring lines and differences in the modelling of the wind turbine. The time series of the above-mentioned motions are provided in Appendix A.

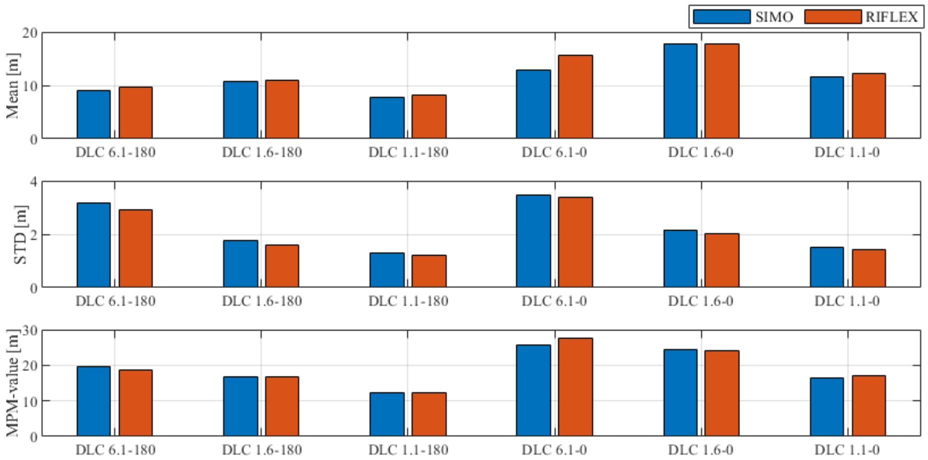

Figure 9.3: Mean, standard deviation, and most probable maximum value of the FWT surge motion. 180: Inline, 0: In-between.

Further, it should be noted that the mean surge motion is largest for DLC 1.6 for both 0° and 180°. This shows the significance of the contribution from the thrust force generated by the wind turbine at rated wind speeds. However, the largest standard deviation and MPM-value is found for DLC 6.1 where the highest H_s value is used. This shows that the wave high is a dominating component for FWT dynamic responses in surge as the waves become more severe.

Figure 9.4 presents the standard deviation and MPM-value of the FWT heave motion. Results show that the SIMO-model typically experiences larger variation in the heave motion and will have a larger maximum heave response compared to the RIFLEX-model in sea states with relatively high H_s values. The RIFLEX-model will have a smaller response in heave due to the inclusion of drag contributions from the mooring lines which provides damping of the FWT responses. For DLC 6.1 the difference in the estimated MPM-value between the two models is close to 1 m, which is quite substantial.

The heave response of the FWT can be observed to increase as the wave height increases and is only governed by the incoming waves.

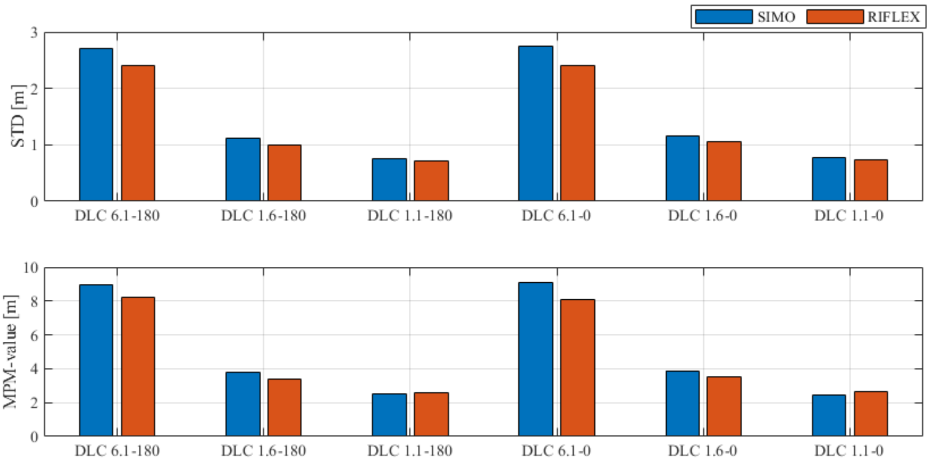

Figure 9.4: Standard deviation and most probable maximum value of the FWT heave motion. 180: Inline, 0: In-between.

Statistics for the FWT pitch motion are presented in Figure 9.5. Results show that the pitch motion of the FWT is dominated by the thrust force generated by the turbine, and thus, the largest mean pitch motion is found for DLC 1.6 which is at rated wind speed. The smallest mean pitch motion is found for DLC 6.1, although this is the load case that by far has the highest wind speed, emphasising the influence the thrust force has on the pitch motion. The relatively high H_s value assigned to the load cases is reflected in the standard deviation and MPM-value. The largest difference found between the two models is obtained during DLC 6.1 with environmental forces acting towards 180°. The results found for this DLC are not quite as expected as the RIFLEX-model is expected to have a lower dynamic pitch motion due to the damping contribution from the mooring lines, however, the results found for this DLC are quite opposite of this anticipation. The reason for this behaviour is explained by a larger mean yaw angle obtained by the SIMO-model which causes a larger portion of the forces to excite the roll motion of the floater, thus, resulting in a lower pitch motion. Time-series of the roll motion for both models are provided in Appendix A.3. Furthermore, as the mooring line is stretched out due to the surge offset, it will give a large moment acting at the fairlead connection. Due to the large motions of the FWT, the mooring line will also experience large dynamic motions which in turn will act as a dynamic moment on the FWT that excites the pitch motion of the floater. This effect will only be captured by the RIFLEX-model.

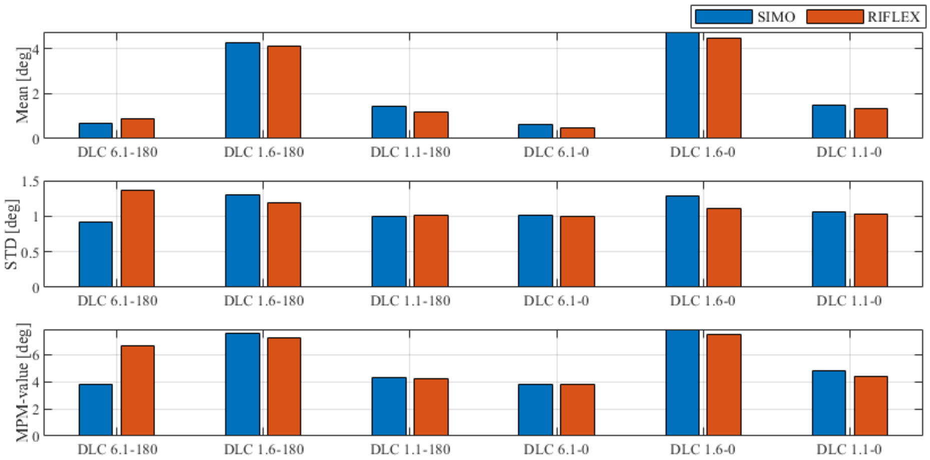

Figure 9.5: Mean, standard deviation, and most probable maximum value of the FWT pitch motion. 180: Inline, 0: In-between.

9.2.2 Mooring Line Top Tension Statistics

As for the FWT motions, the statistics of mooring line top tension are presented for the three load cases with environmental forces acting in both 180° and 0°. Results are presented for the most heavily loaded line. Due to the difference between a quasi-static and dynamic mooring analysis, it is expected to observe larger differences in mooring line tension between the two models than what is observed for the FWT motions.

Figure 9.6 presents the mean, standard deviation, and MPM-value of the mooring line top tension for mooring line number 1 with environmental forces acting towards 180°. Results for mean mooring line top tension show that the obtained mean tension is almost identical for the SIMO- and RIFLEX-model during DLC 1.6 and 1.1. While for DLC 6.1, the mean mooring line tension is somewhat higher for the RIFLEX-model. The equal mean tension is a result of the relatively equal mean surge offset for the two models and can be regarded as the static force obtained in the mooring line at that horizontal offset. The standard deviation and MPM-value in Figure 9.6 reflects the relatively large difference in dynamic tension between the two models for DLC 6.1. The standard deviation for the RIFLEX-model is more than double of the standard deviation for the SIMO-model, indicating much larger fluctuations and deviation from the mean static value for the RIFLEX-model. The large standard deviation means that the RIFLEX-model will obtain higher values for the largest maxima of the line tension which consequently leads to a higher MPM-value. This shows the importance of mooring line dynamics included in the RIFLEX-model. In operation conditions, the mooring line tension is highly dependent on surge motion of the FWT and is thus mainly dominated by the low-frequency turbulent wind-induced response.

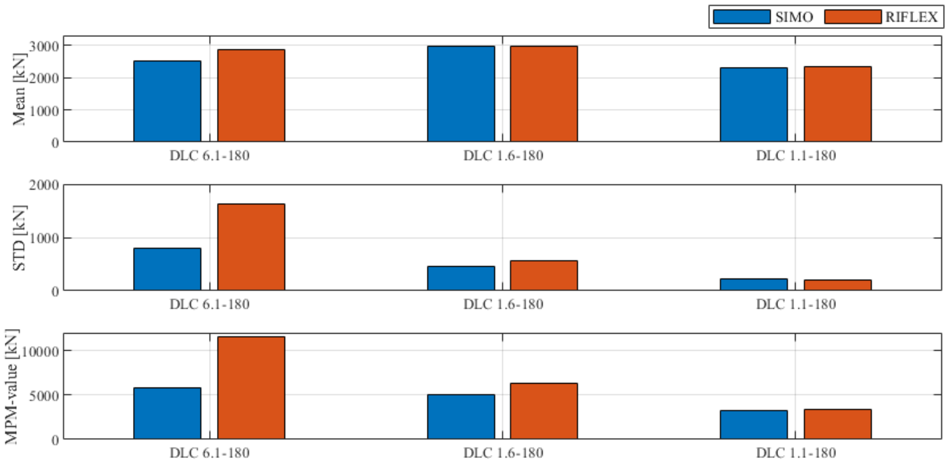

Figure 9.6: Mean, standard deviation, and most probable maximum value of the mooring line top tension for mooring line number 1 with environmental forces acting towards 180°.

Figure 9.7 presents the mean, standard deviation, and MPM-value of the mooring line top tension for mooring line number 3 with environmental forces acting towards 0°. As expected the results show to have an equal behaviour as for mooring line number 1 with environmental forces acting toward 180°. Quite equal results are acquired for the two models during operational load cases indicating that the mooring line tension is governed by aerodynamic forces during such load cases. In addition, the significant wave height is not of a critical value such as considerable mooring line dynamics are excited.

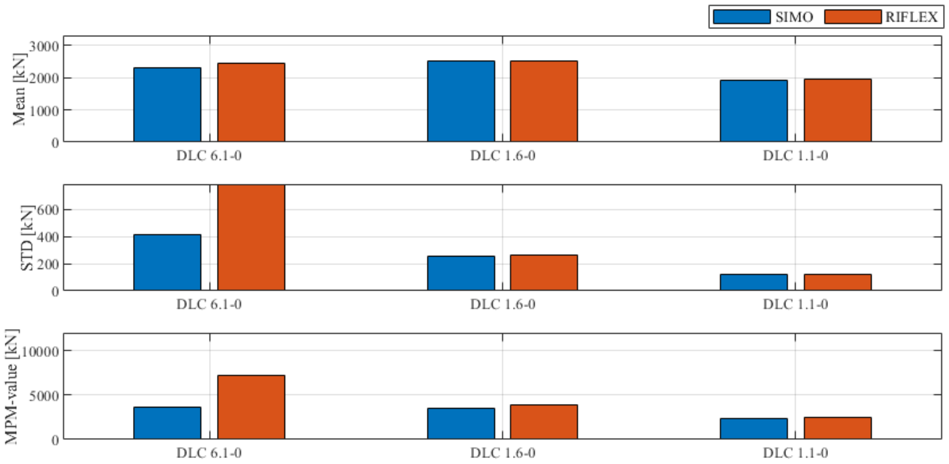

Figure 9.7: Mean, standard deviation, and most probable maximum value of the mooring line top tension for mooring line number 3 with environmental forces acting towards 0°.

9.2.3 Dynamic Motion Responses

This section will present dynamic results from simulations of the chain mooring system through time-series and power spectra of FWT motions. The presented power spectra are the mean spectra from the 15 different realisations from each load case. Results from several load cases will be presented and discussed, however, as the work done in this thesis is mainly focused on ULS design the results from the most severe load cases will be primarily focused on.

Figure 9.8 presents the surge, heave, and pitch motion during DLC 6.1 with environmental forces acting towards 180°, while the power spectra of the motions from the same load case are presented in Figure 9.9. Starting with the time series presented in Figure 9.8, the surge motion has a mean value close to 10 m in the negative x-direction. The mean surge motion is imposed by the mean environmental forces such as mean wind, current, and wave force. Large dynamic motions can be observed for the surge motion, which ranges from positive 3m to negative 20 m. The dynamic motions of the FWT are imposed by the incoming waves which for DLC 6.1 has a quite large H_s-value of 13.5 m. Interestingly, the RIFLEX-model can be observed to generally reach a larger surge offset and has also a marginal larger mean value, this is explained by the difference in yaw motion between the two models as described in Section 9.2.1.

The times series of the pitch motion can be observed to be quite different between the two models. The pitch motion for the RIFLEX-models has a larger dynamic motion which ranges between -5° to 5°. As mentioned, the dynamics of the mooring lines excited by the incoming waves act as a dynamic moment at the fairlead connection which excites the pitch motion of the floater. This can also be observed in the power spectra for the pitch motion in Figure 9.9, where the RIFLEX-model is found to have larger wave frequency responses. A mean pitch angle of just below 1° is imposed by the mean environmental force and is found to be relatively equal between the two models.

The time series of the heave motion is near identical for the two models which should be expected as the mooring system has little influence over the heave motion of a floating structure. The heave motion is mainly wave-induced and follows the surface elevation.

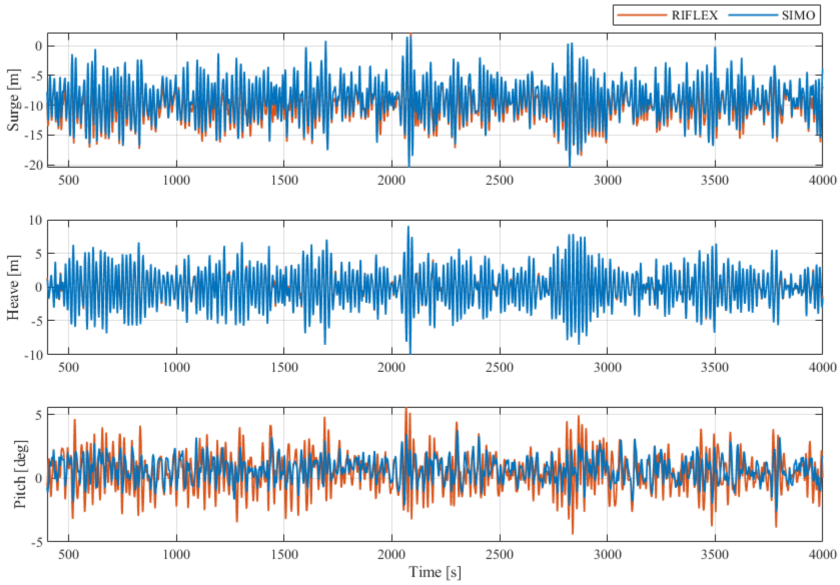

Figure 9.8: Time series of surge, heave, and pitch motion during DLC 6.1 with environmental forces acting towards 180° for both the SIMO- and RIFLEX-model.

The power spectra in Figure 9.9 shows that the surge and heave response mainly is wave frequency dominated with some low-frequency responses due to wind loads acting on the tower and turbine blades. However, since the heave resonance frequency is so close to the wave peak frequency some resonance response will be present for the heave motion. As for the pitch motion, there is some difference in the power spectra between the two models as expected due to the previously discussed differences. The SIMO-model mainly has resonance responses in pitch in addition to some wave frequency and low-frequency wind-induced response. However, for the RIFLEX-model the wave frequency response is dominant with a quite sizeable pitch resonance response as well. More wave frequency response in pitch for the RIFLEX-model is expected due to the contribution from mooring line dynamics.

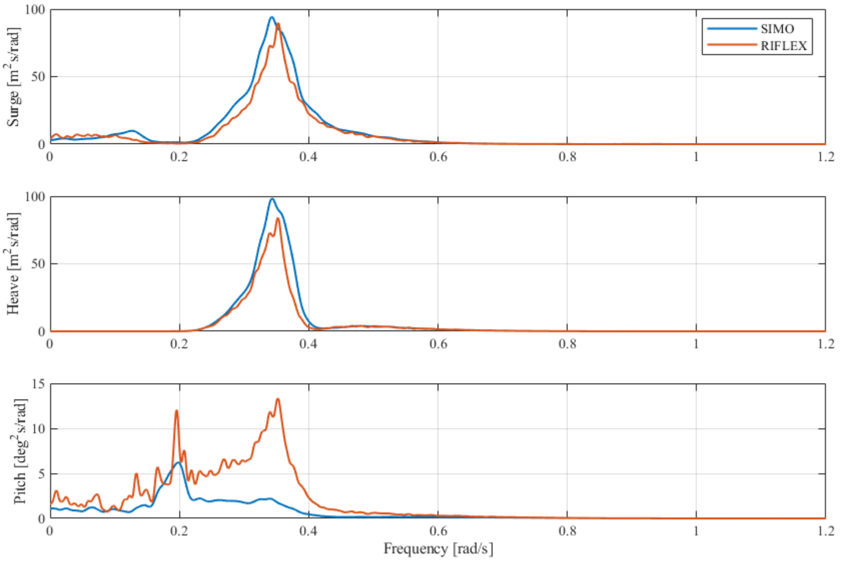

Figure 9.9: Power spectra of surge, heave, and pitch motion during DLC 6.1 with environmental forces acting towards 180° for both the SIMO- and RIFLEX-model.

Time-series and power spectra of the FWT surge, heave, and pitch motion during DLC 1.6 with environmental forces acting towards 0° are presented in Figure 9.10 and Figure 9.11, respectively. The time series of the surge motion shows that the surge motion has a smaller dynamic response when compared with results from DLC 6.1. As DLC 1.6 is an operational condition at rated wind speed the surge motion will be largely dominated by wind, which is further confirmed from the power spectra of the surge motion in Figure 9.11. Furthermore, the power spectra of the surge motion show that the FWT experiences surge resonance responses close to a frequency of 0.067 rad/s in addition to some wave frequency responses.

The heave response is, similar to DLC 6.1, dominated by the incoming waves. However, for DLC 1.6 the dominating heave responses are resonance responses at a frequency of 0.38 rad/s. The wave peak frequency is 0.41 rad/s which is fairly close to the heave resonance frequency and thus excites the heave resonance responses.

Time-series of the pitch motion show that the pitch response is, to a larger extent, equal for the two models during DLC 1.6. As this is an operational load case the wind turbine is facing upwind in both models, generating a more or less equal aerodynamic pitch and yaw moment for the two models. The mean pitch angle is close to 5° which is imposed by the large thrust force at rated wind speed. The power spectra of the Pitch motion show that the pitch response is mainly dominated by pitch resonance responses in addition to low-frequency wind responses. Furthermore, some responses with a frequency between 0.05-0.1 rad/s are observed which correlates well with responses observed in the surge power spectra indicating a possible surge-pitch coupling effect.

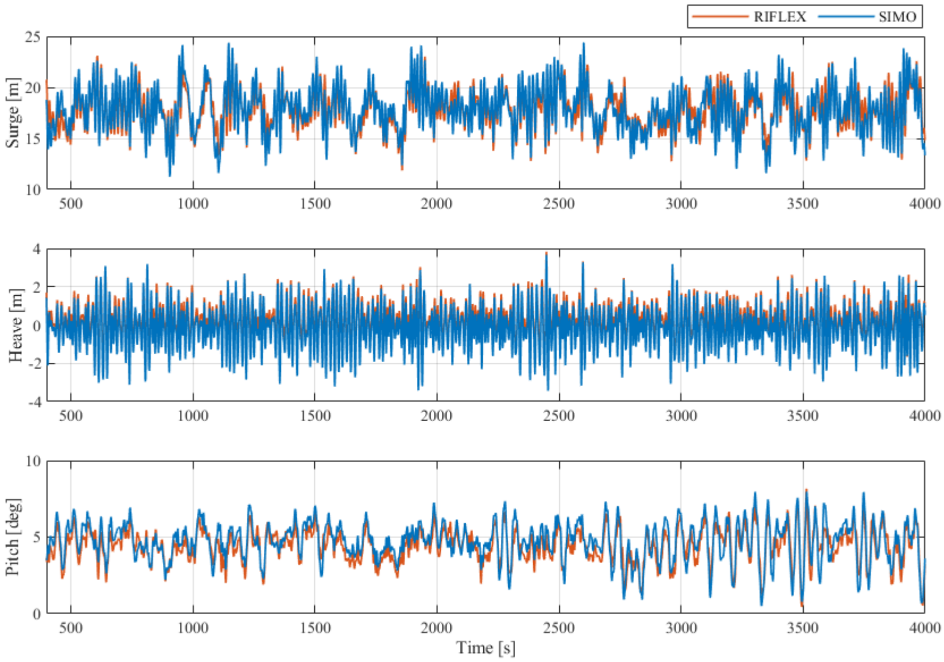

Figure 9.10: Time series of surge, heave, and pitch motion during DLC 1.6 with environmental forces acting towards 0° for both the SIMO- and RIFLEX-model.

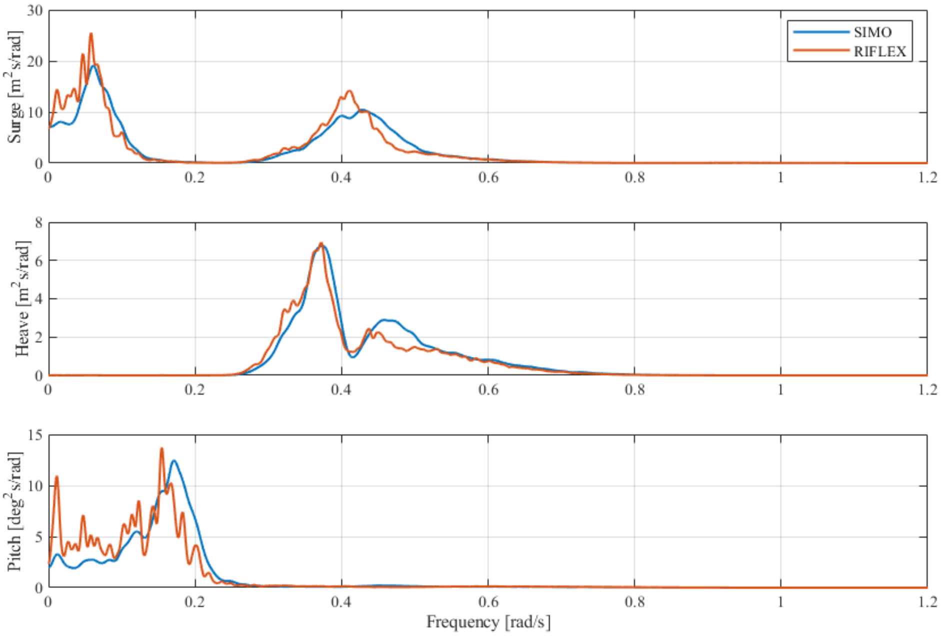

Figure 9.11: Power spectra of surge, heave, and pitch motion during DLC 1.6 with environmental forces acting towards 0° for both the SIMO- and RIFLEX-model.

9.2.4 Dynamic Mooring Line Tension Responses

This section will present dynamic results from simulations of the chain mooring system through time-series and power spectra of mooring line tension. As for the FWT motions, the power spectra are the mean spectra from the 15 different realisations from each load case.

Figure 9.12 presents the time-series and power spectra of mooring line tension in line number 1 during DLC 6.1 with environmental forces acting towards 180°. Quite distinctive differences can be observed in the mooring line tension between the two models. The quasi-static results provided from the SIMO-model rarely show a tension level below the pretension of 1400 kN. This is due to the quasi-static approach which does not consider dynamic effects in the mooring lines which may lead to slack mooring lines even at large horizontal offsets. Furthermore, the quasi-static approach gives lower values for the global maxima, and thus, underestimates the MPM-value of the mooring line tension. When studying the time series of the mooring line tension provided by the RIFLEX-model, a higher degree of dynamic behaviour is observed, with tension levels ranging from 0 to just below 14 000 kN. This shows that the mooring lines experience a slack condition before becoming heavily loaded again. Slack may cause the mooring line to entangle around components near or at the fairlead and consequently damage the structure. Hence, a high occurrence of slack line is not favourable. These results show that a fully dynamic model is needed to identify the occurrence of slack lines. Power spectra of the line tension show that mooring line responses mainly are dominated by wave frequency response. The power spectra emphasise the difference in line tension obtained by the two models with a significantly higher energy density found for the RIFLEX-model.

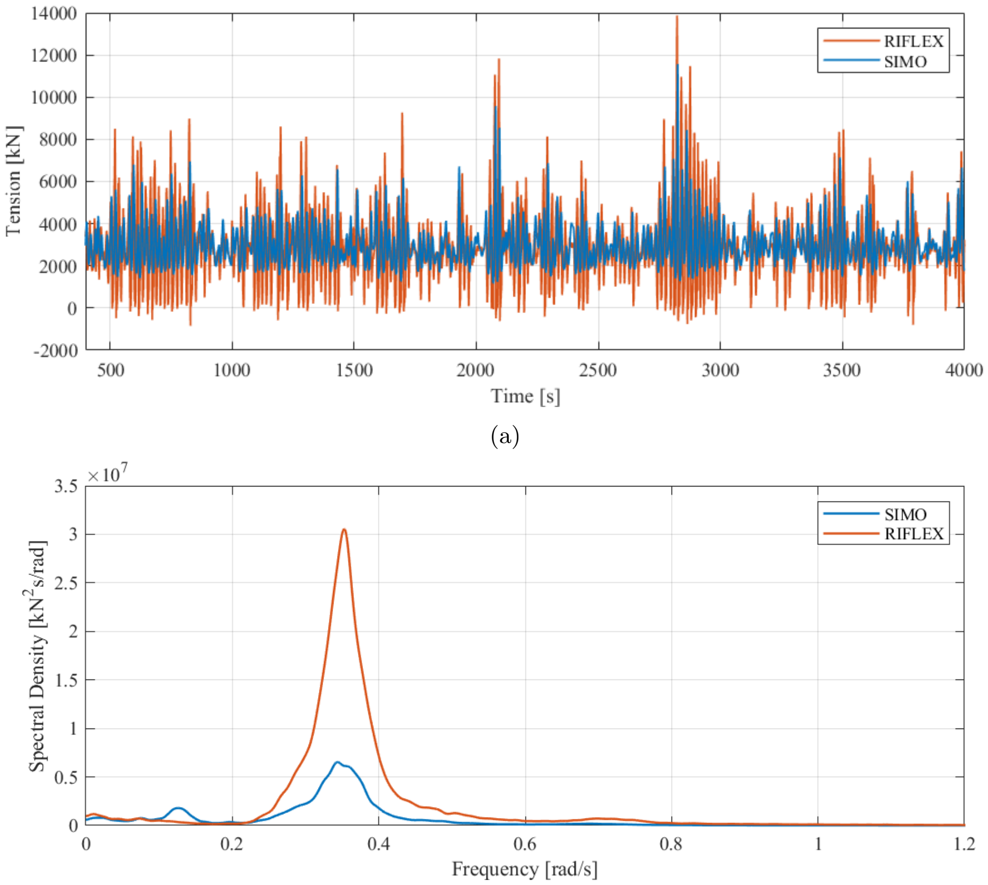

(a)

(b)

Figure 9.12: Time series (a) and power spectra (b) of mooring line tension in line number 1 during DLC 6.1 with environmental forces acting towards 180° for both the SIMO- and RIFLEX-model.

Time-series and spectral density of mooring line tension in line number 3 for DLC 1.6 with environmental forces acting towards 0° are presented in Figure 9.13. The time series of the mooring line tension shows that although the mean tension level is almost identical to the one obtained for mooring line number 1 during DLC 6.1, the dynamic variation in tension is considerable smaller during DLC 1.6. This is mainly due to a less severe sea state and large mean thrust force from the wind turbine which keeps the FWT at a more stable horizontal offset. Furthermore, the restoring forces are divided over two mooring lines which naturally will reduce the force needed to be retained by one line.

Due to fewer dynamics in the mooring line tension, the global maxima along the time series are at a lower level for this DLC. The power spectra in Figure 9.13b shows that the dominating response component varies between the two models. For the RIFLEX-model the dominating response component to the mooring line tension is wave frequency responses while surge resonance response comes second in line to the response contribution. For the SIMO-model the opposite can be observed. Typically for a quasi-static analysis, the wave frequency responses will be underestimated while resonance responses are overestimated due to mooring line drag forces not being included. Both models show effects from low-frequency wind responses.

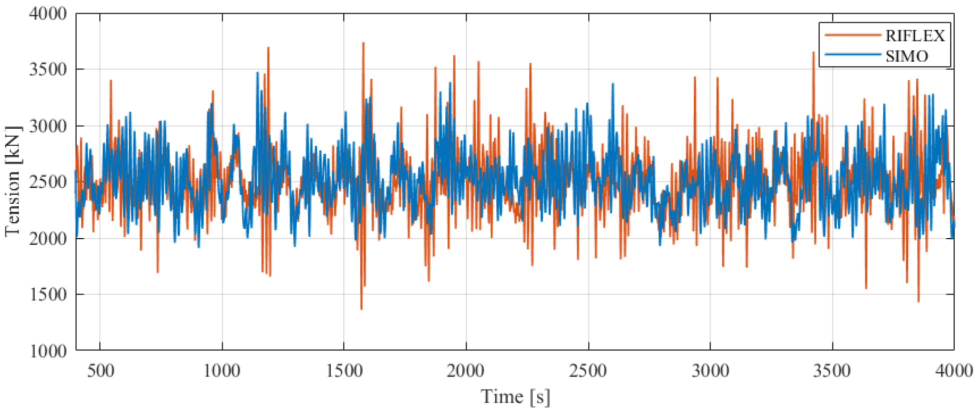

(a)

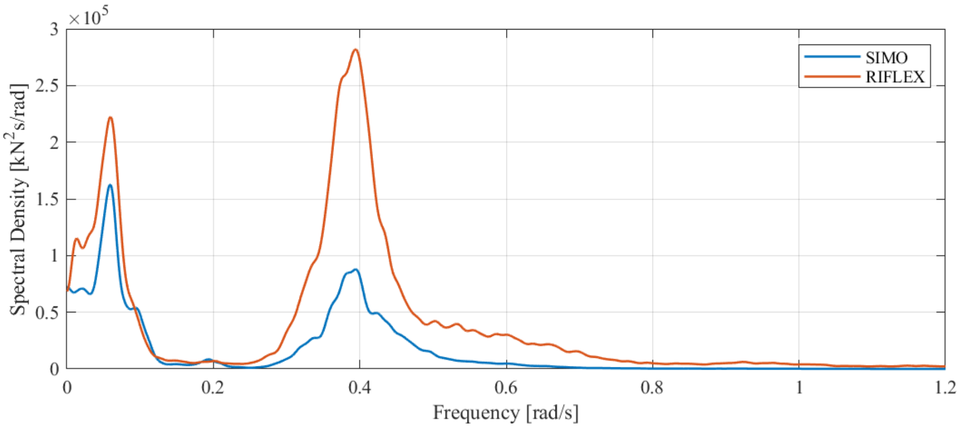

(b)

Figure 9.13: Time series (a) and power spectra (b) of mooring line tension in line number 3 during DLC 1.6 with environmental forces acting towards 0° for both the SIMO- and RIFLEX-model.

To further investigate the large difference in dynamic response between the quasi-static and dynamic approach the tension in mooring line number 1 and the corresponding offset in surge is studied. Figure 9.14 presents the mooring line tension as a function of surge offset for mooring line 1 during DLC 6.1 acting towards 180°. The figure clearly shows how different the two approaches calculate the tension at various surge offsets. The results for the SIMO-model can be observed to follow the typical shape of a restoring curve for a catenary mooring system, quite expected, as the quasi-static approach uses a precalculated line characteristics table for the determination of the resulting mooring line tension for a specific fairlead coordinate. Further, the figure gives a good understanding of the substantial amount of dynamics captures by the fully dynamic approach. Although the FWT has a surge offset well above 15 m the mooring line becomes slack at the fairlead, indicating large movements of the mooring line.

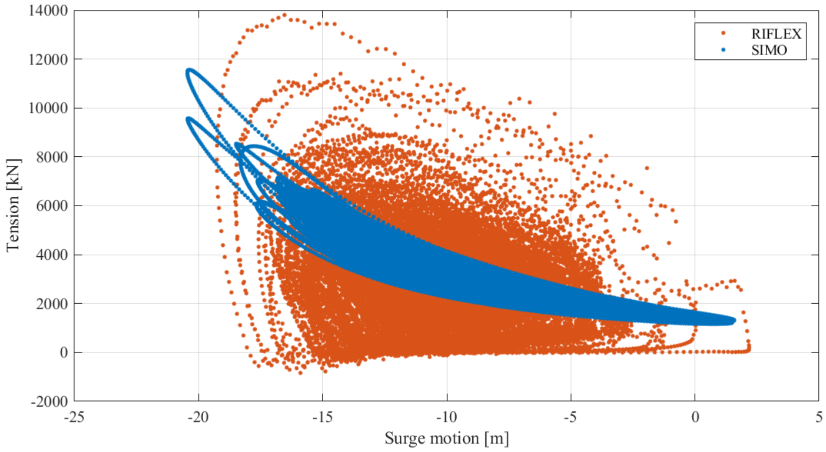

Figure 9.14: Mooring line tension as a function of the corresponding surge offset for mooring line 1 during DLC 6.1 with environmental parameters acting towards 180°.

9.2.5 Design Tension and Utilization Factor

As part of the ULS-mooring design process, the design tension value and utilization factor are calculated for each mooring line during all DLCs. The calculation procedure is as described in Section 4.6. The utilization factor gives a good perspective of tension responses compared to the material limit and makes it convenient to tell if the mooring line capacity is exceeded.

Table 9.3 and 9.4 provides design tension value and utilization factor for both the SIMO- and RIFLEX-model for all relevant load cases with environmental forces acting towards 180° and 0°, respectively. Results show that the largest design tension, and consequently utilization factor, is obtained during DLC 6.1 acting towards 180° in line number 1 which is the windward line during this load case.

The difference in line tension between the SIMO- and RIFLEX-model is again captured in the calculated values for the two models. As Table 9.3 shows the RIFLEX-model obtains a utilization factor above 1, indicating that the calculated design tension exceeds the characteristic capacity of the mooring line. For the SIMO-model however, the utilization factor is found to be well below 1. Results such as this underline the importance of performing a fully coupled dynamic analysis of the mooring system and moored structure when investigating ULS design of mooring systems. Using only the quasi-static approach would lead to a major underestimation of the mooring line forces which potentially could lead to a mooring line rupture. A difference of nearly the same magnitude is also observed for line number 3 during DLC 6.1 acting towards 0°, however, the characteristic capacity is not exceeded in this load case.

Table 9.3: Design tension and utilization factor for all three lines for the SIMO- and RIFLEX-model with environmental forces acting in a direction of 180°, largest design tension value and utilisation factor is marked in red.

	DLC 6.1 - 180 deg						DLC 1.6 - 180 deg					
Model	Line 1		Line 2		Line 3		Line 1		Line 2		Line 3	
	T_d	UF	T_d	UF	T_d	UF	T_d	UF	T_d	UF	T_d	UF
SIMO	14963	0.83	4275	0.24	1673	0.09	7455	0.41	1756	0.10	1744	0.10
RIFLEX	18992	1.05	3751	0.21	2067	0.11	9663	0.53	1828	0.10	1819	0.10

	DLC 1.1 - 180 deg					
Model	Line 1		Line 2		Line 3	
	T_d	UF	T_d	UF	T_d	UF
SIMO	4644	0.26	1933	0.11	2011	0.11
RIFLEX	5078	0.28	1872	0.10	2261	0.12

Further, the separation in utilization factor between the two models can be seen to decrease as the environmental parameters become less severe and the wind turbine is in an operational state. This is due to less dynamic responses in the mooring lines as a result of smaller waves which makes the quasi-static approach quite adequate for such load cases.

The consequence of giving the RNA a 20° yaw angle during DLC 6.1 should also be noticed. By doing so the FWT reach a yaw angle close to 10°, thus, reducing the tension in either mooring line number 1 or 2. However, forces are still retained by two lines and results show that the obtained design tension is well within the limits for the most heavily loaded line.

From the results presented in Table 9.3 and 9.4 it can be concluded that the governing ULS design load case is DLC 6.1 acting towards 180°.

Table 9.4: Design tension and utilization factor for all three lines for the SIMO- and RIFLEX-model with environmental forces acting in a direction of 0°, largest design tension value and utilisation factor is marked in red.

	DLC 6.1 - 0 deg						DLC 1.6 - 0 deg					
Model	Line 1		Line 2		Line 3		Line 1		Line 2		Line 3	
	T_d	UF	T_d	UF	T_d	UF	T_d	UF	T_d	UF	T_d	UF
SIMO	1761	0.10	4320	0.24	8200	0.45	1018	0.06	5226	0.29	5473	0.30
RIFLEX	2808	0.16	9453	0.52	11581	0.64	1289	0.07	5950	0.33	5998	0.33

	DLC 1.1 - 0 deg					
Model	Line 1		Line 2		Line 3	
	T_d	UF	T_d	UF	T_d	UF
SIMO	1415	0.08	3411	0.19	3295	0.18
RIFLEX	1495	0.08	3780	0.21	3692	0.20

9.3 Synthetic Fibre Rope Mooring Systems

The following sections will present results for the synthetic fibre rope mooring systems. Results from the chain mooring system obtained from the RIFLEX-model are included as a comparison. Decay simulations and restoring curves are first presented followed by statistics and dynamic analysis of motion and tension response. Thereafter, results for design tension and utilization factor is presented and discussed. For the synthetic fibre rope systems and RIFLEX-chain system, one additional DLC has been simulated called DLC 1.1R. As stated in Section 5.2, the intention of the DLC is to uncover possible unwanted behaviour of the FWT at rated wind speed with corresponding expected wave height. Power spectra and statistics presented in the following sections are mean values derived from the 15 realisations of each DLC.

9.3.1 Decay Simulations

Decay simulations for the synthetic mooring systems are carried out in the same procedure as for the chain mooring systems, as described in Section 7.1. time-series of the decay simulations are presented in Figure 9.15, while the calculated natural periods for all rigid body motions from the corresponding decay simulations are presented in Table 9.5.

Studying the time series of the decay simulations it becomes quite clear that the surge and sway motions have the larges variation between the systems. Also, the yaw motion is influenced, but to a smaller extent. Right away, it should be noticed that System II has a considerable low natural period of around 33 s in both surge and sway which indicates that the mooring system is too stiff. Normally, a surge and sway period of such low value would not be accepted due to the close proximity to the wave period range. Additionally, changes in the roll and pitch natural periods are signs of the mooring system being too stiff. This gives a good illustration of the challenge when designing polyester mooring systems in shallow waters. The material properties of polyester make the polyester fibre ropes relatively stiff when shorter lengths of ropes are used.

The effect of installing clump weights can be seen to be quite significant when observing the natural period in surge and sway for System III. System III has the same lines as System II, however, with clump weights installed 200 m from the fairlead. Results show that by installing the clump weights the horizontal stiffness of System II is reduced to an acceptable level.

Still, when the length of the polyester mooring lines is increased by 550 m, as they are for System IV, the natural periods in the horizontal plane are still relatively low. Due to the shallow water, the angle between the horizontal plane and the mooring line is quite sensitive to changes in mooring line length. A longer line length will make this angle smaller which consequently increases the horizontal restoring stiffness, and thus, works against the increased line length to some extent.

Disregarding the chain mooring system, the highest natural period for the surge and sway motions is found for the nylon system. The line length for this mooring system is equal to the one used in System II, giving a clear illustration of how the material properties of the lines change their restoring behaviour.

Using the obtained natural period in yaw to find the yaw stiffness, it is found that none of the mooring systems has an adequate stiffness in yaw when using the requirement to avoid a potential roll-yaw coupling phenomenon as described in Section 4.11.1. However, this requirement is derived for a system with a small difference between the uncoupled natural periods in roll and yaw which may result in a too conservative requirement for a system of this configuration. Furthermore, if this requirement was to be met the stiffness of the mooring systems would have to be increased. Putting this into context with System II, which already is too stiff, the requirement needs to be met through other means, by for example adding a bridle connection to the mooring lines.

Table 9.5: Natural periods for all investigated mooring systems.

System	Surge	Sway	Heave	Roll	Pitch	Yaw
I	94.2 s	95.2 s	16.3 s	28.4 s	30.7 s	84.9 s
II	33.3 s	33.5 s	16.2 s	26.6 s	29.0 s	67.4 s
III	70.2 s	70.2 s	16.3 s	28.7 s	30.9 s	74.6 s
IV	49.9 s	49.9 s	16.2 s	28.3 s	30.7 s	73.2 s
V	67.4 s	67.2 s	16.3 s	28.3 s	30.6 s	65.3 s
VI	81.1 s	81.2 s	16.3 s	28.4 s	30.6 s	65.2 s

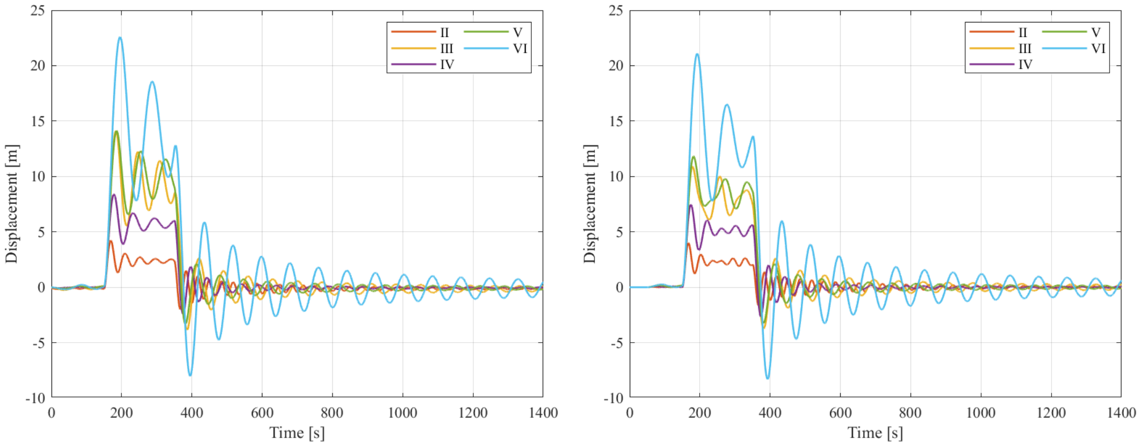

(a) Surge (b) Sway

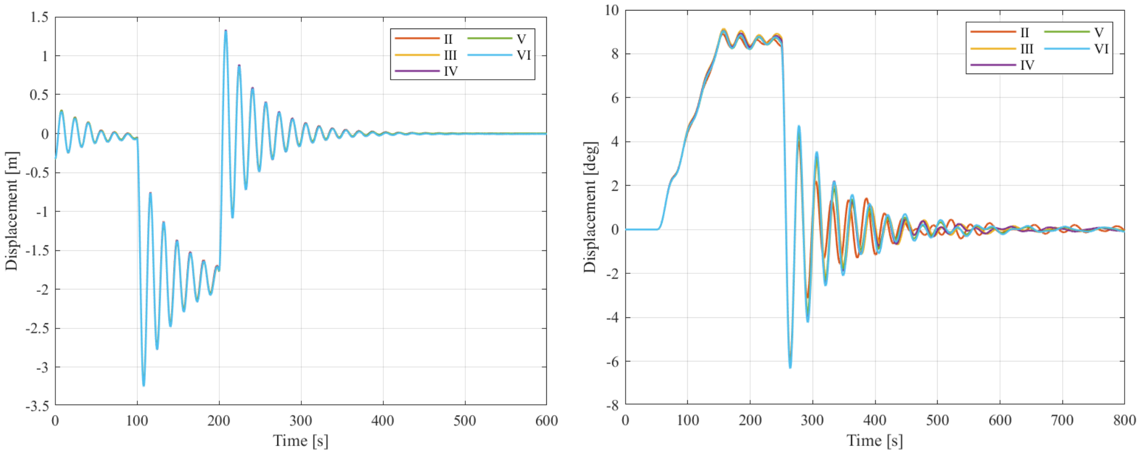

(c) Heave (d) Roll

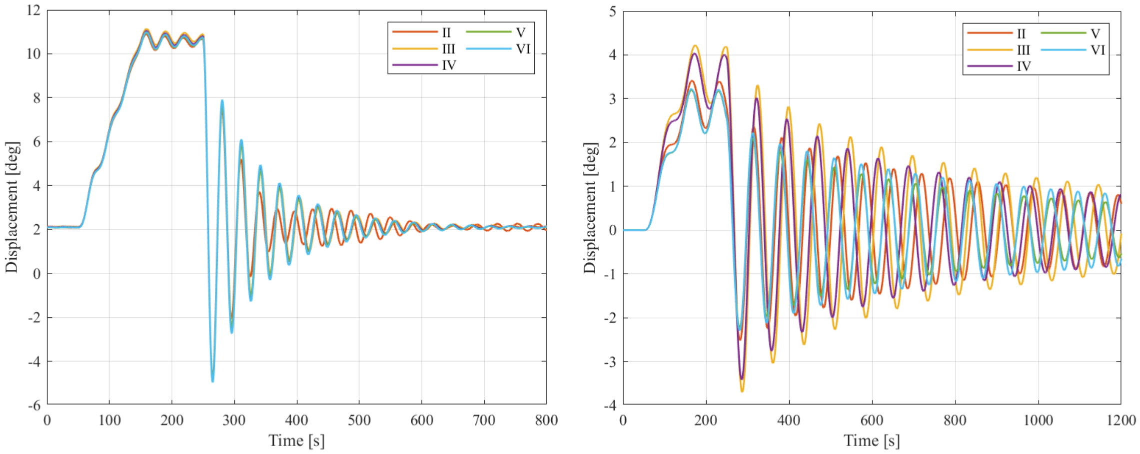

(e) Pitch (f) Yaw

Figure 9.15: Time series of decay simulations for all FWT rigid body motions.

9.3.2 Restoring Characteristics

Restoring curves in surge for all the synthetic fibre rope mooring systems are presented in Figure 9.16. The restoring curves are established through a series of static analyses with increasing external force applied to the FWT. The static analysis is used to capture the working curve from the SyROPE-model, as this sets the tension level for the dynamic analysis. As expected the restoring curve for System II is found to be the steepest curve while the least steepest curve is found for System VI. A curvature of the restoring curve can be observed for all the polyester systems, this can be recognised from the working curve in the SyrROPE-model. This curvature can however not be observed for the nylon system, this is due to the softness of the nylon rope and a larger elongation of the rope is needed to capture this curvature. Further, the restoring curves show that all of the mooring systems have a softer behaviour for forces acting towards 0°, i.e. in-between mooring lines 2 and 3. System III, IV, and V can is found to have fairly equal restoring curves in surge, with System III being to some degree stiffer in the negative x-direction.

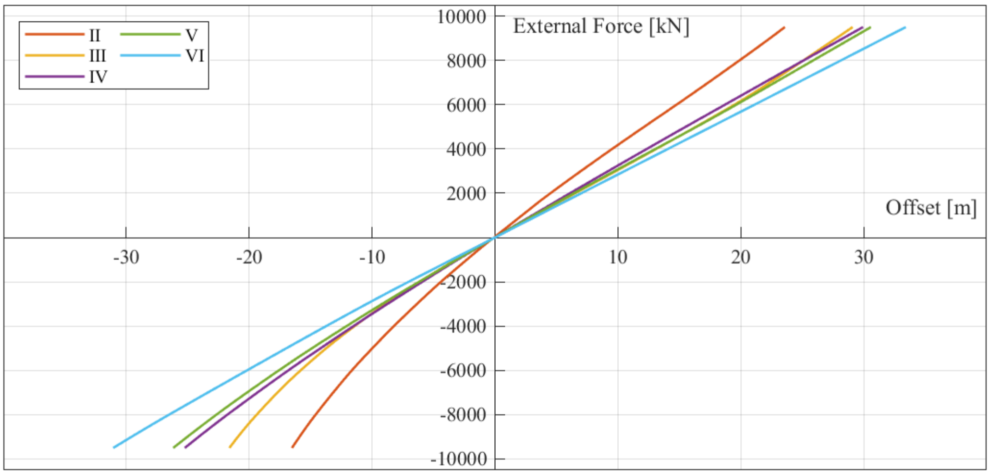

Figure 9.16: Restoring curves in surge for the synthetic fibre rope mooring systems. Negative and positive offset corresponds to inline and in-between loading, respectively.

9.3.3 Motion Response Statistics

As for the chain mooring system, statistical properties of the surge, heave, and pitch motion is presented and discussed within this section.

The mean value, standard deviation, and MPM-value of the surge motion are presented in Figure 9.17 for all relevant load cases for both 180° and 0°. The largest mean and MPM-value are found for System VI during all DLCs. For DLCs acting towards 0° the obtained mean and MPM-value for System I and VI are quite equal caused by the softer behaviour of the catenary system when forces are acting in-between lines. Further, another system that stands out with a low mean value compared to the other systems is System II. The stiffness from the short polyester lines results in a mean surge offset that rarely exceeds 5 m. Systems III, IV, and V can be observed to have relatively similar behaviour for the surge motion. The standard deviation and MPM-value of the surge motion can be seen to increase with the severity of the sea state.

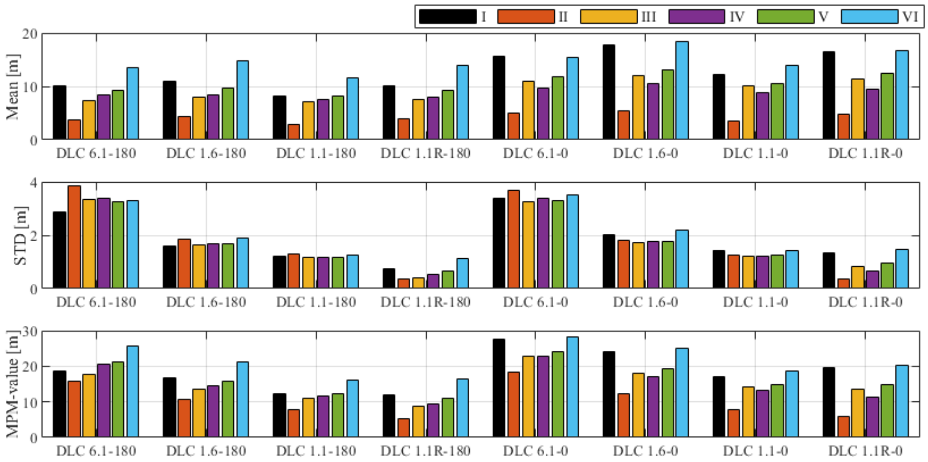

Figure 9.17: Mean, standard deviation, and most probable maximum value of the FWT surge motion for all investigated mooring systems.

Figure 9.18 presents standard deviation and MPM-value of the heave motion for all relevant load cases for both 180° and 0°. Results for the heave motions show that the standard deviation and MPM-value are heavily dependent on the sea state with increasing values for both parameters with increasing wave height. No significant difference is found for the different synthetic mooring systems. However, the chain mooring system is found to have a lower value for the standard deviation and MPM. This is due to damping contributions from the chain mooring lines, which due to the catenary configuration will have a larger vertical motion in the water as the FWT moves vertically.

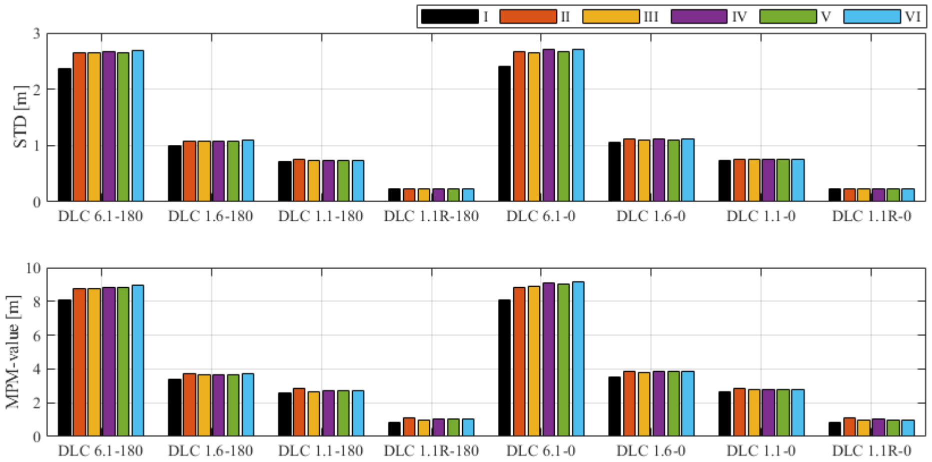

Figure 9.18: Standard deviation and most probable maximum value of the FWT heave motion for all investigated mooring systems.

Results for the pitch motion, presented in Figure 9.19, show that the mean and MPM-value are heavily dependent on the operational state of the wind turbine with the largest values occurring during conditions at rated wind speed. The mean pitch angle is found to be close to zero during the extreme load case, although the MPM-value is found to be quite large due to the severity of the sea state. Marginal differences are found between the systems for the standard deviation, and it is observed that the standard deviation is affected by both the severity of the sea state and aerodynamic forces.

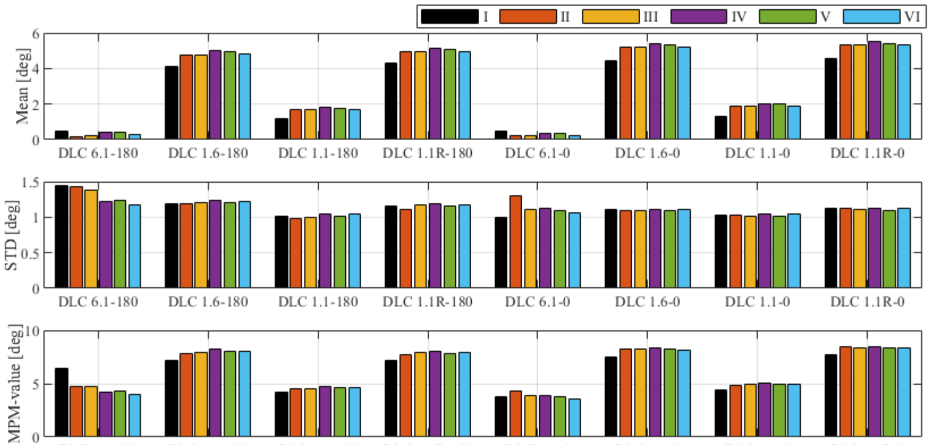

Figure 9.19: Mean, standard deviation, and most probable maximum value of the FWT pitch motion for all investigated mooring systems.

9.3.4 Mooring Line Top Tension Statistics

Statistics for the mooring line top tension for all the investigated mooring systems are presented within this section. Results are shown for the most heavily loaded line, as done for the chain mooring system.

Statistics of the mooring line tension in mooring line 1 with environmental parameters acting toward 180° is compared in Figure 9.20. Firstly, it is found that the mean tension level does not vary extensively between the systems during the various DLCs. However, when looking back at the mean surge motion in Figure 9.17, it is observed that this mean tension is attained at quite different surge offsets. This is an expected result and is reflected through the restoring curves of the systems. The standard deviation is found to be largest for System II during all DLCs, this is caused by the high stiffness in the lines which results in a rapid increase in tension for relatively small increases in elongation of the line. The standard deviation and MPM-value are found to follow the severity of the sea state and decrease with decreasing wave height. During DLC 6.1 the MPM-value is found to be largest for System I, caused by larger dynamic motions of the mooring line due to the catenary configuration.

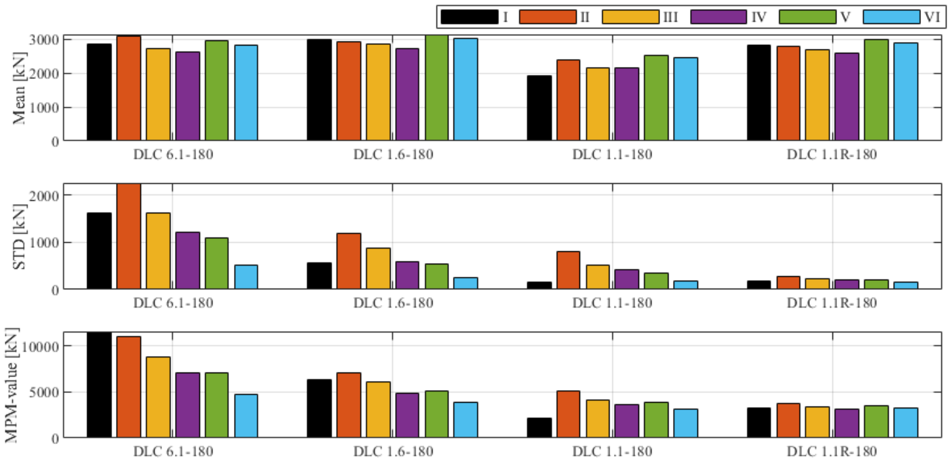

Figure 9.20: Mean, standard deviation, and most probable maximum value of the mooring line top tension for mooring line number 1 with environmental forces acting towards 180°.

Looking at the statistics of the mooring line tension in mooring line 3 with environmental parameters acting toward 0° in Figure 9.21 near identical results as for mooring line 1 are observed. Mean tension is, as expected, somewhat lower due to the direction of the environmental forces and is also here quite equal between the different systems.

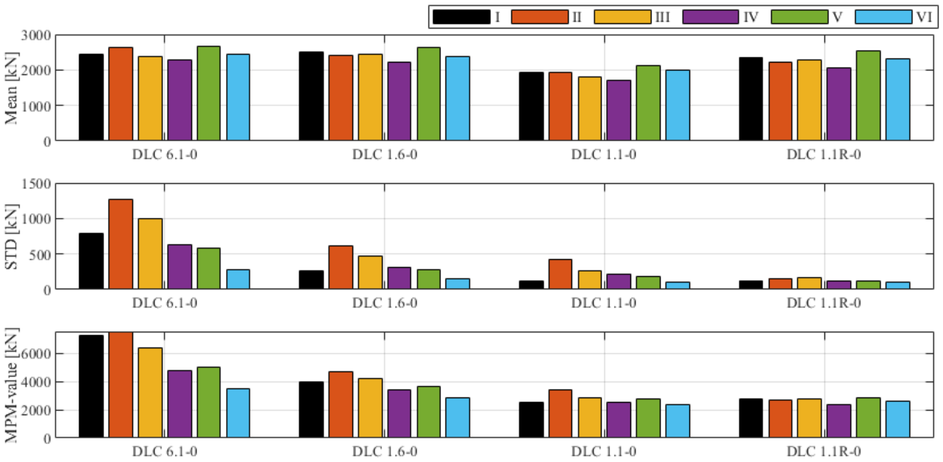

Figure 9.21: Mean, standard deviation, and most probable maximum value of the mooring line top tension for mooring line number 3 with environmental forces acting towards 0°.

9.3.5 Dynamic Motion Responses

Dynamic results for the FWT motions will within this section be presented and discussed. Results are presented for DLC 6.1 and 1.1R to investigate the behaviour of the mooring systems at such different load cases. Only Surge and pitch motion are presented as the heave motion is found to be more or less equal for all systems as described in Section 9.3.3.

Figure 9.22 presents the time-series of the FWT dynamic and total surge motion during DLC 6.1 acting towards 180°. From the full time series of the total surge motion in Figure 9.22a the difference in mean surge offset between the systems is clearly visible.

Quite interestingly, when removing the mean motion and the dynamic motion is investigated, it is found that the dynamic surge responses are fairly equal between the different systems. Two systems that slightly stand out are System II and VI, which can be observed to some extent obtain larger amplitudes in the dynamic motion. The larger amplitudes do however not occur at the same time intervals for the two Systems. Using the power spectra of the surge motion given in Figure 9.23 it is found that System II have the largest spectral density at the wave frequency while System IV is observed to have surge resonance responses in addition to low-frequency wind responses.

The remaining systems are found to have quite equal dynamic responses with wave frequency responses as the dominating component. The chain mooring system is observed to have the lowest spectral density of the systems, explained by a larger damping contribution from the mooring lines.

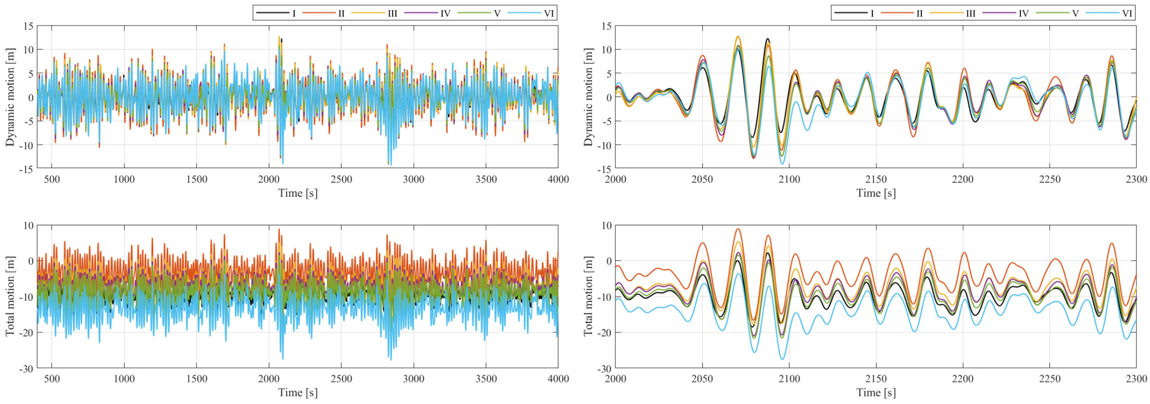

(a) (b)

Figure 9.22: Full time series (a) and time series window (b) of FWT dynamic and total surge motion during DLC 6.1 acting towards 180° for all investigated mooring systems.

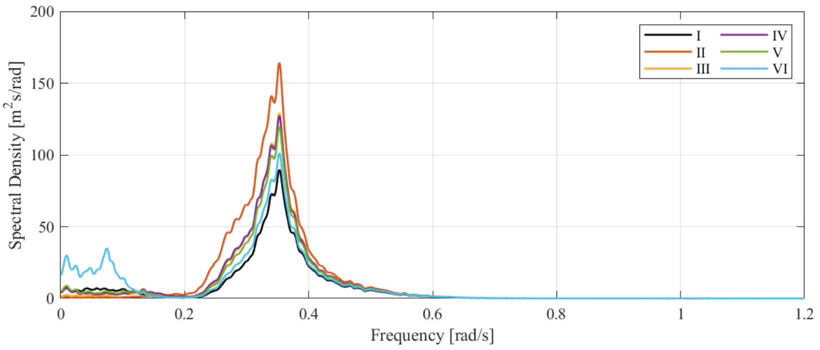

Figure 9.23: Power spectra of FWT surge motion during DLC 6.1 acting towards 180° for all investigated mooring systems.

Time series of the FWT dynamic and total pitch motion for the various systems during DLC 6.1 is presented in Figure 9.24. From the time series of the dynamic motion, it is found that the behaviour of the pitch motion generally is quite equal for the different systems. However, some differences in the magnitude of the pitch amplitudes are observed, with the chain mooring system reaching the largest amplitudes. This is explained by a larger amount of wave frequency responses for the chain mooring system, as shown in the power spectra of the pitch motion in Figure 9.24.

From the power spectra, it is observed that the synthetic fibre rope systems have a matching behaviour in terms of the dominating responses which are found to be pitch resonance responses, while wave frequency responses are somewhat less dominating. The opposite is found for the chain mooring system, here wave frequency responses are the dominating component of the pitch response. In addition, some low-frequency wind-induced response is observed.

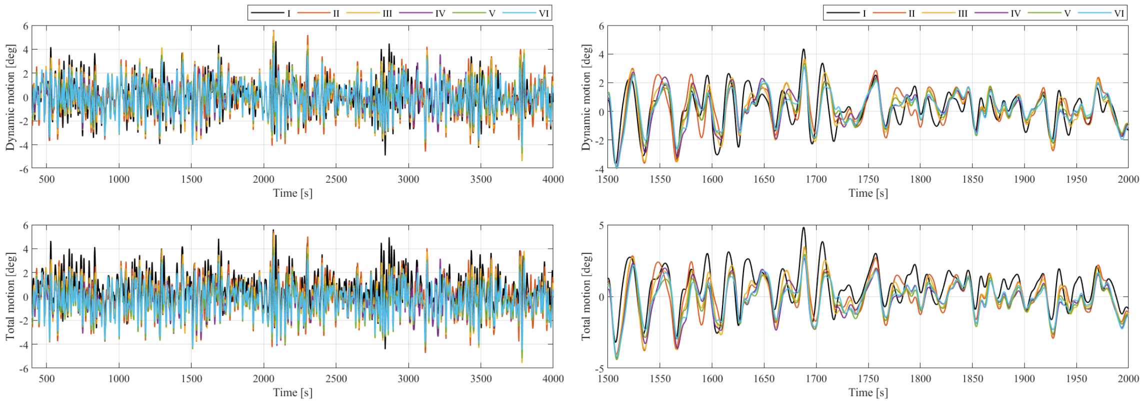

(a)

(b)

Figure 9.24: Full time series (a) and time series window (b) of FWT dynamic and total pitch motion during DLC 6.1 acting towards 180° for all investigated mooring systems.

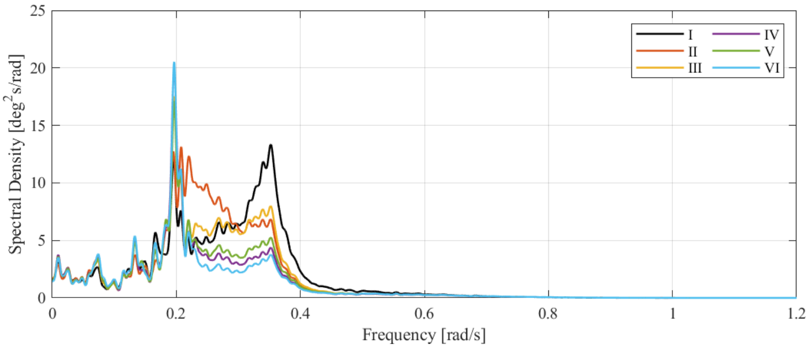

Figure 9.25: Power spectra of FWT pitch motion during DLC 6.1 acting towards 180° for all investigated mooring systems.

Figure 9.26 shows the FWT surge and pitch motion during DLC 1.1R acting towards 0°. The power spectra of the same motions are presented in Figure 9.27. Starting with the surge motion the significant difference in surge offset imposed by the wind turbine thrust force is well captured in the time series. System II is found to have the smallest offset as well as the smallest dynamic motion. When compared with the dynamic motion of System I and VI the dynamic motion of System II nearly appears to be zero, making System II come across as stiffness dominated. Systems III, IV, and V have quite equal behaviour in surge during DLC 1.1R, mainly separated by the mean offset.

The power spectra of the surge motion show that the surge response is mainly dominated by surge resonance responses in addition to some low-frequency wind excitation. Further, the spectra show a low amount of wave frequency response, although quite minor compared to the resonance responses.

Looking at the time series of the FWT pitch motion in Figure 9.26, little to no difference can be observed in the dynamic motion between the various systems. This is also reflected in the power spectra of the pitch motion. The pitch motion is mainly found to be dominated by pith resonance responses in addition to low-frequency wind responses.

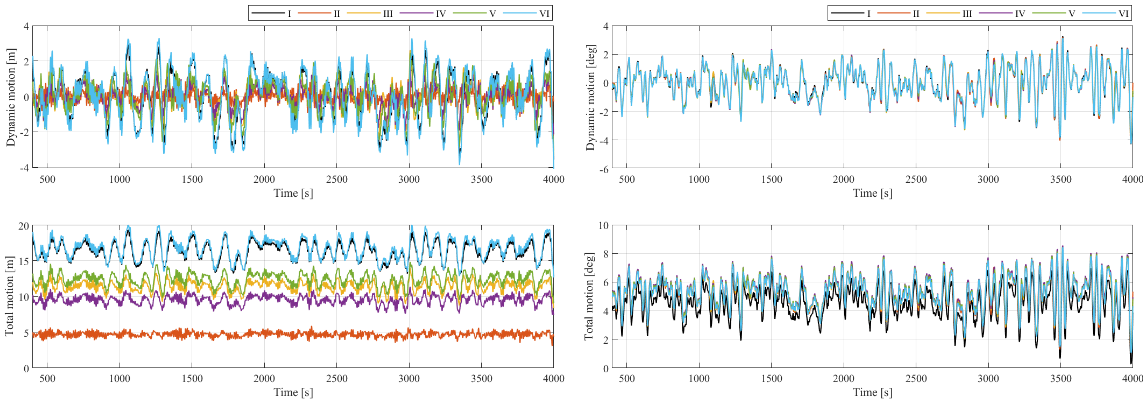

(a) (b)

Figure 9.26: Full time series of FWT dynamic and total surge (a) and pitch (b) motion during DLC 1.1R acting towards 0° for the investigated mooring systems.

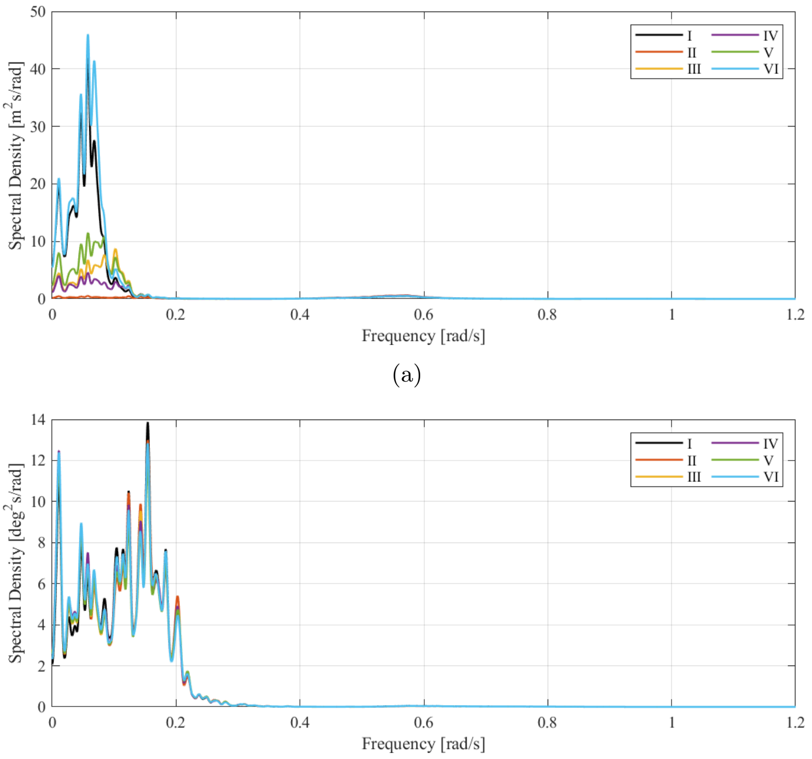

(a)

(b)

Figure 9.27: Power spectra of surge (a) and pitch (b) motion during DLC 1.1R acting towards 0°for the investigated mooring systems.

9.3.6 Dynamic Mooring Line Tension Responses

The dynamic mooring line tension responses will in this section be presented and discussed. Results are presented for the same load cases as for the dynamic motion responses in addition to DLC 1.6. Results are given for the most heavily loaded line during each load case.

Time-series and power spectra of the mooring line tension during DLC 6.1 acting towards 180° are presented in Figure 9.28. From the statistics of the mooring line tension, it is shown that the mean tension level is rather equal between the different systems. However, observing the time series of the line tension a sizeable difference in the dynamic behaviour of the systems is seen. Large dynamic variations are observed for System I, II, and III, while System IV, V, and VI have lower variations in the tension with System VI having the by far smallest.

A high degree of dynamic tension with large fluctuation is generally not ideal for the fatigue life of the mooring lines and may shorten the lifetime of the lines quite substantially.

Slack line can be observed to occur for the majority of the systems with the exception being Systems V and VI. Mooring line slack is normally not a significant problem for a chain mooring system other than the potential risk of entanglement of the mooring line around components near the fairlead. For lines constructed of only synthetic fibre ropes, however, a high occurrence of slack line should be avoided due to the risk of the mooring line touching the seabed and consequently having soil ingress in the fibre rope. Slack line is also observed to occur for the leeward lines for System II and IV, time-series of the mooring line tension in line number 3 is provided in Appendix B.1. However, this does not occur for the systems with clump weights, indicating that the wave excitations are absorbed by the additional weight in the line, as for the chain mooring system.

Generally, System II would not be acceptable for a FWT of this configuration and at this location, based on the high occurrence of slack line in addition to the high portion of mooring line dynamics. For system III, however, the inclusion of clump weights is observed to reduce the dynamic responses and number of slack line events. This arguably makes System III seem like a more feasible system.

The power spectra in Figure 9.28b show that the tension responses are dominated by wave frequency responses. The power spectra further show that System IV, V, and VI to a larger degree absorbs the wave frequency excitations, with system VI being superior to the rest. It should also be noticed that System III has quite equal responses as the chain mooring system

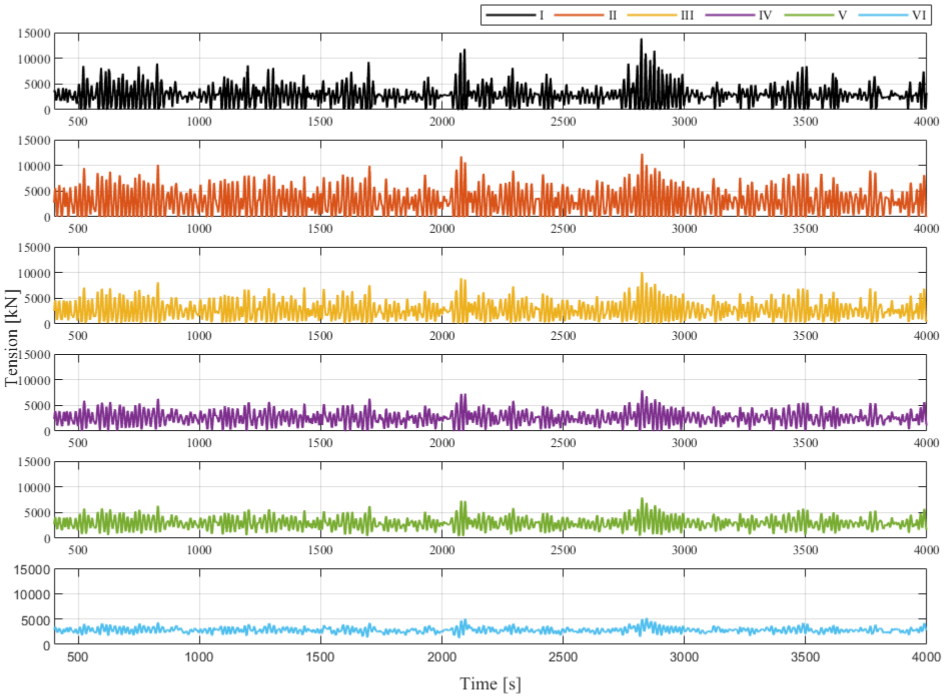

(a)

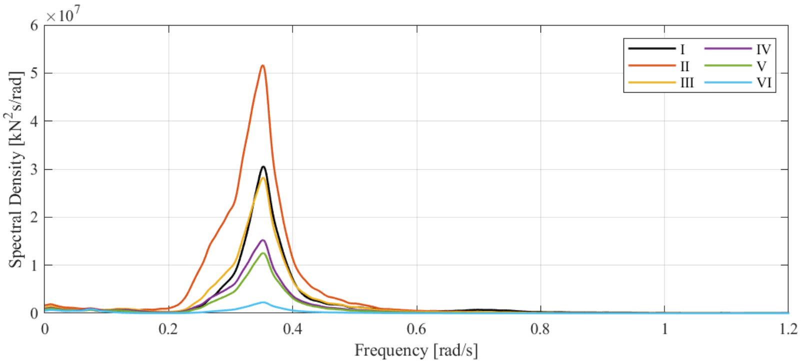

(b)

Figure 9.28: Time series (a) and power spectra (b) of mooring line tension in line number 1 during DLC 6.1 acting towards 180° for the investigated mooring systems.

Results presented for DLC 1.1R in Figure 9.29 show a relatively equal behaviour between the systems. Still, System II shows to be the system with the largest amount of tension dynamics caused by a larger degree of wave frequency responses as seen in Figure 9.29b. Furthermore, System II shows tension responses that are connected with pitch resonance in addition to some surge and low-frequency wind responses.

Responses during this operational case are directly influenced by floater surge motion and are mainly dominated by low-frequency turbulent wind-induced responses.

None of the systems is found to experience slack in mooring line 3 during DLC 1.1R. However, slack is detected when investigating the time series for the leeward line for System II given in Appendix B.2. Again, the polyester systems that have clump weights are found to have more stable tension responses in the leeward line.

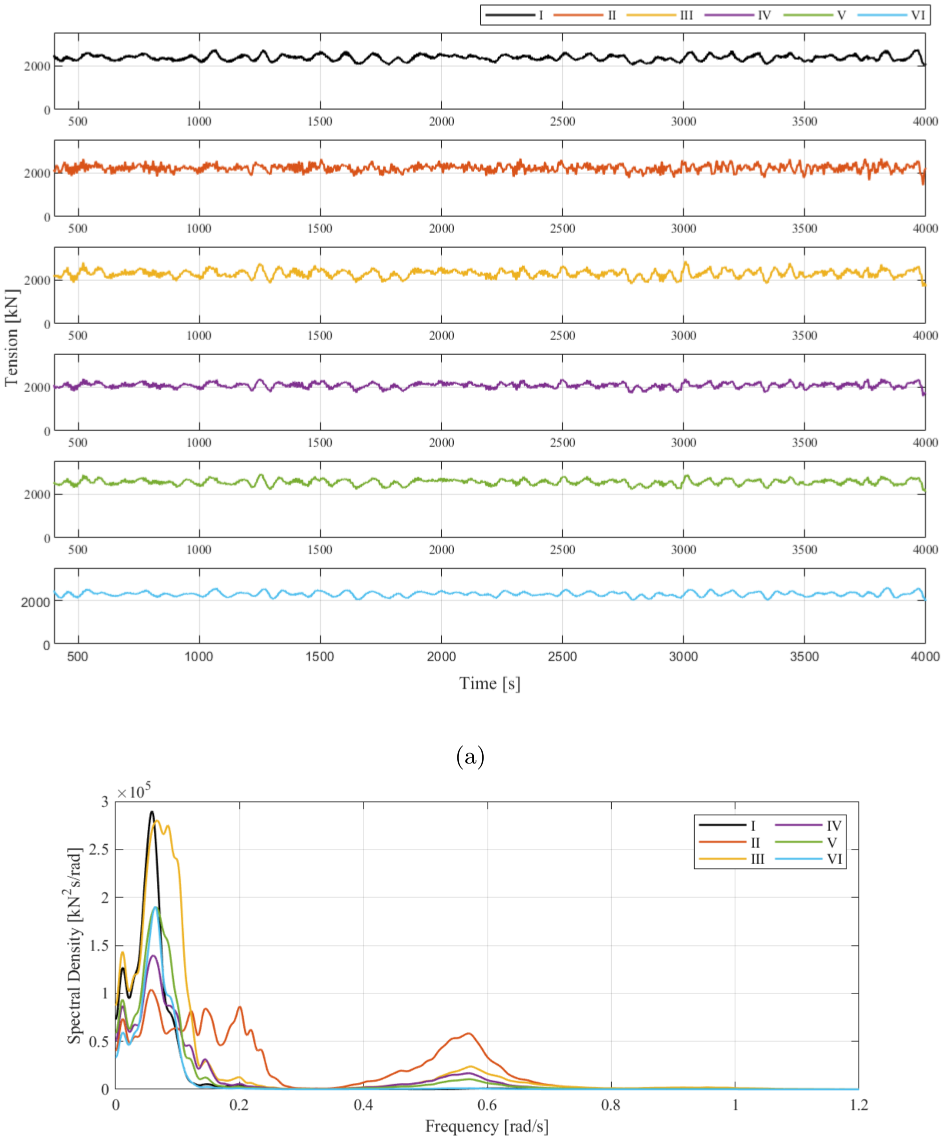

(a)

(b)

Figure 9.29: Time series (a) and power spectra (b) of mooring line tension in line number 3 during DLC 1.1R acting towards 0° for the investigated mooring systems.

The results for mooring line tension in line 1 during DLC 1.6 acting towards 180° are included to compare the tension responses between the two operational conditions at rated wind speed.

Time series and power spectra of the mooring line tension in line 1 during DLC 1.6 is presented in Figure 9.30. Once again System II is found to have a considerably larger amount of dynamic responses compared to the other systems. On the other side, the nylon system is found to absorb almost all of the wave frequency excitation due to the low stiffness in the mooring lines. System IV and V are found to have a relatively equal behaviour during DLC 1.6 with the largest amplitudes observed for System IV.

Power spectra in Figure 9.30b show that System II, in addition to wave frequency responses, also has some pitch resonance responses. Low-frequency wind-induced responses are observed for all systems. Comparing the spectra from DLC 1.1R with the one for DLC 1.6 shows a complete change in the dominating response contribution with wave frequency responses being dominant for DLC 1.6 due to the severe sea state.

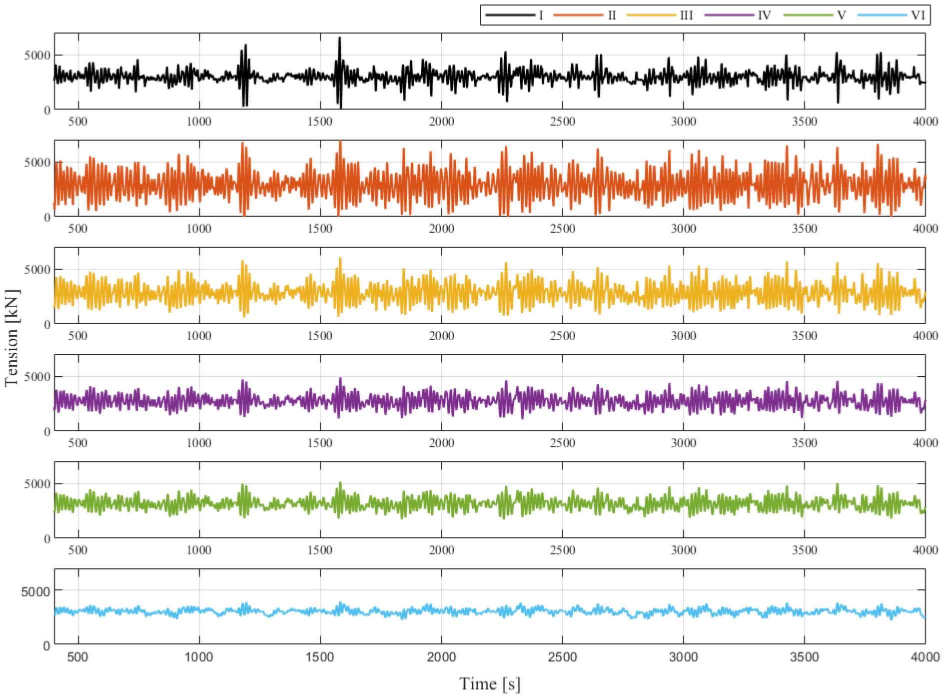

(a)

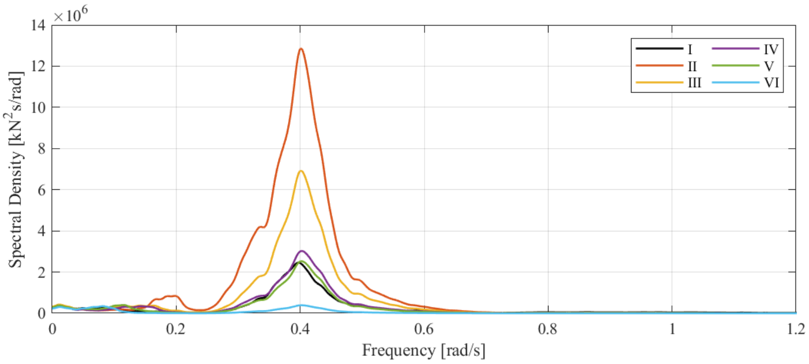

(b)

Figure 9.30: Time series (a) and power spectra (b) of mooring line tension in line number 1 during DLC 1.6 acting towards 180° for the investigated mooring systems.

9.3.7 Design Tension and Utilization Factor

As for the chain mooring system the design tension value and utilization factor are calculated for each mooring line during all DLCs.

Results for design tension value and utilization factor for all investigated mooring systems are presented in Table 9.6 and 9.7 for all load cases with environmental forces acting towards 180° and 0°, respectively. In addition, the tension MPM-value and utilization factor for all systems and DLCs is presented as a bar chart in Figure 9.31 for the most heavily loaded line.

Results show that the synthetic fibre rope system that has attained the largest design tension value is System II in line number 1 during DLC 6.1 acting towards 180°. All systems obtain the largest utilization factor during DLC 6.1 acting towards 180°. The chain mooring system still has the highest design tension value in line number 1 among the different systems. The highest design tension is found for System II for all the remaining DLCs, with the exception of DLC 1.1R acting towards 0°. It should also be noted that System II has considerably larger design tension levels in the leeward lines during all DLCs. This further supports the anticipation of System II being too stiff.

None of the synthetic fibre rope systems are found to have a utilization factor above 1. Disregarding System II the largest utilization factor is found to be 0.76 for System III during DLC 6.1 acting towards 180°. This is well within the limit of 1 and shows that a lower MBS potentially could be used.

Table 9.6: Design tension and utilization factor for all three lines for the investigated mooring systems with environmental forces acting in a direction of 180°. The largest value is marked in red while the second largest is marked in yellow.

System	DLC 6.1 - 180 deg						DLC 1.6 - 180 deg					
	Line 1		Line 2		Line 3		Line 1		Line 2		Line 3	
	T_d	UF	T_d	UF	T_d	UF	T_d	UF	T_d	UF	T_d	UF
I	18992	1.05	3751	0.21	2067	0.11	9663	0.53	1828	0.10	1819	0.10
II	18014	0.97	8503	0.46	7240	0.39	10996	0.59	4150	0.22	4176	0.22
III	14197	0.76	6237	0.33	3898	0.21	9294	0.50	2595	0.14	2582	0.14
IV	11294	0.61	4784	0.26	3614	0.19	7261	0.38	2592	0.14	2623	0.14
V	11056	0.59	4936	0.26	3512	0.19	7547	0.40	2709	0.15	2725	0.15
VI	6953	0.37	2983	0.16	2119	0.11	5504	0.29	2006	0.11	2036	0.11

System	DLC 1.1 - 180 deg						DLC 1.1R - 180 deg					
	Line 1		Line 2		Line 3		Line 1		Line 2		Line 3	
	T_d	UF	T_d	UF	T_d	UF	T_d	UF	T_d	UF	T_d	UF
I	5078	0.28	1872	0.10	2261	0.12	4474	0.25	1707	0.09	1638	0.09
II	7898	0.42	3628	0.19	3941	0.21	5223	0.28	2067	0.11	2158	0.12
III	6345	0.34	2200	0.12	2570	0.14	4682	0.25	1561	0.08	1556	0.08
IV	5339	0.29	2344	0.13	2557	0.14	4267	0.22	1530	0.08	1627	0.08
V	5580	0.30	2507	0.13	2767	0.15	4765	0.26	1968	0.11	2013	0.11
VI	4337	0.23	2047	0.11	2347	0.13	4408	0.24	1829	0.10	1907	0.10

During operational load cases with a less severe sea state and where the tension level is relatively small the chain mooring system is found to have a low utilization factor. However, during more extreme load cases the utilization factor can be observed to have a dramatic increase compared with the increase in the synthetic fibre rope systems. Higher waves impose large dynamic motions on the catenary mooring lines which causes additional loads.

The system with clearly better performance is the nylon system, with the highest utilization factor found to be 0.37. This is a difference of 0.6 compared with System II during the same load case. One concern for nylon fibre ropes is the fatigue lifetime, which for early studies has shown to be short. However, in a recent study by Chevillotte et al. [63] it is concluded that fatigue lifetime should not be a limiting factor for mooring of FWT with nylon fibre ropes, provided that appropriate coatings are applied to the nylon fibres. However, it currently exists little to no experience in using nylon fibre ropes for long term mooring applications, thus, making the long term performance of the ropes very uncertain. The FLOATGEN demonstrator, which is the first mooring system of such size that uses nylon fibre ropes, will provide valuable knowledge on how the nylon fibre ropes cope as a part of a long term mooring system.

Table 9.7: Design tension and utilization factor for all three lines for all the investigated mooring systems with environmental forces acting in a direction of 0°. The largest value is marked in red while the second largest is marked in yellow.

	DLC 6.1 - 0 deg						DLC 1.6 - 0 deg					
System	Line 1		Line 2		Line 3		Line 1		Line 2		Line 3	
	T_d	UF	T_d	UF	T_d	UF	T_d	UF	T_d	UF	T_d	UF
I	2808	0.16	9453	0.52	11581	0.64	1289	0.07	5903	0.33	5998	0.33
II	10103	0.54	10941	0.59	12040	0.65	5377	0.29	7099	0.38	7085	0.38
III	5379	0.29	8756	0.47	10130	0.54	2131	0.11	6262	0.34	6241	0.33
IV	5564	0.30	6526	0.35	7296	0.39	2980	0.16	4950	0.27	4942	0.27
V	4689	0.25	6716	0.36	7565	0.41	2564	0.14	5213	0.28	5193	0.28
VI	2339	0.13	4100	0.22	4997	0.27	1502	0.08	3911	0.21	3924	0.21

	DLC 1.1 - 0 deg						DLC 1.1R - 0 deg					
System	Line 1		Line 2		Line 3		Line 1		Line 2		Line 3	
	T_d	UF	T_d	UF	T_d	UF	T_d	UF	T_d	UF	T_d	UF
I	1495	0.08	3780	0.21	3692	0.2	1180	0.07	3712	0.21	3742	0.21
II	4695	0.25	5320	0.29	5172	0.28	1912	0.10	3732	0.20	3688	0.20
III	1943	0.10	4397	0.24	4220	0.23	1102	0.06	3815	0.20	3865	0.21
IV	2837	0.15	3730	0.20	3653	0.20	1284	0.07	3263	0.18	3244	0.17
V	2504	0.13	4079	0.22	3958	0.21	1579	0.08	3901	0.21	3919	0.21
VI	1713	0.09	3264	0.18	3198	0.17	1316	0.07	3439	0.18	3499	0.19

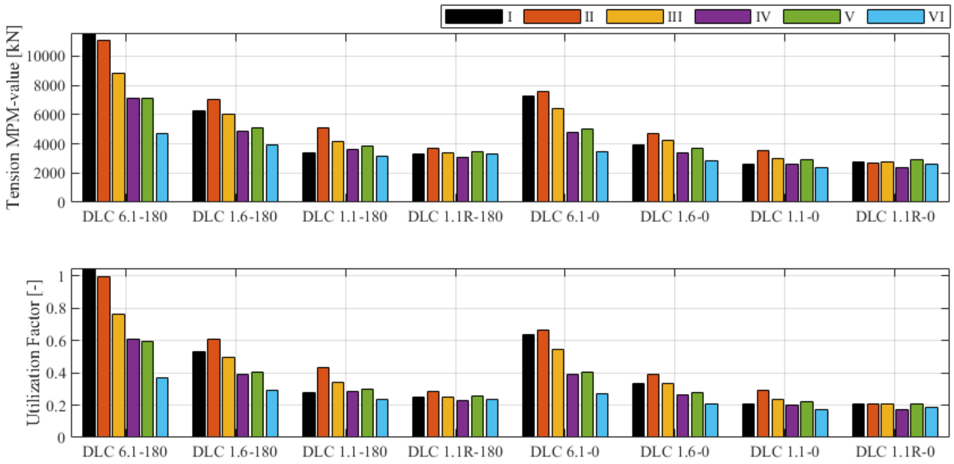

Figure 9.31: Mooring line tension MPM-value and utilization factor for the most heavily loaded line.

10 Conclusion and Recommendations for Further Work

The following sections will present a short summary of the main results and the main concluding points made from the work done in this thesis. Additionally, recommendations for how the work can be continued is presented in further work.

10.1 Conclusion

In this thesis, a numerical simulation comparison study of different mooring concepts and design methods for FWTs has been performed in accordance with ULS design. Four load cases acting in two directions have been considered including operational conditions with the turbine rotating and extreme conditions with the turbine in idle. Design tension and utilization factor values for the mooring system have been calculated in accordance with ULS regulations. Representative load cases are selected to investigate the FWT motion and mooring line tension responses.

In the comparison between the quasi-static and fully dynamic simulation approaches, it is found large differences in dynamic responses and utilization factors during extreme loading conditions. The anticipation was that the two approaches would give quite equal results due to the shallow water depth. However, it is found that the mooring lines will experience large dynamic excitations even at this water depth, due to the severity of the sea state. As a result, the calculated design tension for the quasi-static approach was underestimated by 22% compared to the fully dynamic approach which had a utilization factor above 1.

Further, it is found that during operational load cases with sea states of less severity the difference in obtained utilization factor is smaller between the two approaches. Thus, it is concluded that a quasi-static approach is not suitable for ULS calculations for mooring design. However, for station keeping at operational conditions with low significant wave height, the quasi-static approach may be adequate.

From the results of the synthetic fibre rope systems, it is found that the pure polyester system with a line length of 700 m has the largest dynamic responses during most load cases. This is further reflected in the design tension and utilisation factor where System II obtains the largest values among the synthetic fibre rope systems. Furthermore, the large degree of dynamic tension resulted in a high occurrence of slack lines for System II which is unwanted behaviour. The results show that System II is a too stiff system to be used for mooring of FWTs, indicating that the main properties of the catenary system are not well transferred to a taut system with polyester lines.

It is further found that the high degree of dynamic tension is reduced by attaching clump weights to the mooring lines. This makes the short lines of 700 m from System II a more feasible solution. However, System III is still found to have quite an extensive amount of tension responses and is considered to be on the edge of what can be tolerated in terms of allowance of slack and fatigue life.

Among the polyester systems, it is System IV and V, with a line length of 1250 m, which is found to have the most optimal results in terms of ULS design and responses. Both systems generally have a lower variation in tension responses compared to the chain and other polyester systems. System V is found to have a lower degree of dynamic tension due to the inclusion of the clump weights.

However, it is found that the system that by far has the best performance is the nylon mooring system. Tension responses due to waves are near negligible when compared to the other systems. Furthermore, the calculated utilization factor for the nylon system is the lowest during all load cases due to the small dynamic responses. It should be noted that the nylon system is the system that obtains the largest surge offset. However, as stated in Section 7.2, no strict limit of the permissible offset of a FWT exists and as long as the power cable is designed in correlation to the expected offset of the FWT it should not be a limiting factor. Finally, development of the fatigue life of nylon ropes is being made and as stated by Chevillotte et al. [63] fatigue lifetime should not be a limiting factor for mooring of FWT with nylon fibre ropes, provided that appropriate coatings are applied to the nylon fibres.

In conclusion, pure synthetic fibre rope mooring configurations are found to be highly suitable for the mooring of FWTs in shallow European waters. For systems with polyester mooring ropes, it may be necessary to incorporate clump weight components to reduce to amount of dynamic responses in the mooring lines and to reduce the horizontal stiffness of the system. Furthermore, an adequate mooring line length should be used for systems with polyester lines to avoid a too stiff behaviour. Nylon ropes are found to be the best performing material for mooring of FWTs in shallow waters due to the material properties resulting in an appropriate stiffness even with short mooring lines. System IV and V are recommended as possible solutions for a polyester due to a low occurrence of slack line and an acceptable level of mooring line tension dynamics. These systems also keep the offset of the FWT during operational conditions at a tolerable level. System VI is the overall recommended mooring solution based on the obtained results. It is found to absorb the wave excitations of the FWT to a much larger degree than the other systems and has a low amount of dynamic tension in the mooring lines which is reflected in a low utilization factor.

10.2 Further Work

Suggested actions for the continuation of the work done in this thesis are listed in this section.

- Perform ALS and FLS simulations of the recommended mooring systems to investigate if the mooring systems can withstand a mooring line failure and have a sufficient lifetime.
- Perform wave contour and non-collinear weather analysis for the recommended mooring systems to possibly uncover a worse loading condition for these systems as this may not be the same as for the chain mooring system.
- If ALS and FLS simulations give results that are well within the limit the mooring systems should be further optimised.
- Generate new wind files with a sufficient number of wind seeds such that each simulation has a different input for both the wind and waves.
- Perform a quasi-static analysis of a taut mooring system with a linear elastic model for the mooring lines as a comparison to the work done in this thesis. Taut systems have a lower amount of mooring line dynamics which can lead to quite equal results between the quasi-static and fully dynamic approaches.
- Investigate additional system configurations with nylon fibre ropes or a combination of polyester and fibre ropes.
- Carry out a cost analysis of the recommended mooring systems and compare them with a chain only mooring system.
- Additional responses of the FWT should be controlled when the mooring system is changed. This includes, but is not limited to, tower bending moments and axial force, structural forces in the floater and fatigue life of structural components.
- Investigate the feasibility of modelling the RNA on the wind turbine as a drag element during extreme load cases.

Bibliography

[1] IEA. 'World energy outlook 2021'. IEA, Paris. (2021), [Online]. Available: https://www.iea.org/reports/world-energy-outlook-2021.

[2] ——, 'Renewable energy market update - may 2022'. IEA, Paris. (2022), [Online]. Available: https://www.iea.org/reports/renewable-energy-market-update-may-2022.

[3] DNV, *Energy transition outlook 2021 - technology progress report*, 2021.

[4] ——, 'Floating wind: The power to commercialize'. (2020), [Online]. Available: https://www.dnv.com/focus-areas/floating-offshore-wind/commercialize-floating-wind-report.html.

[5] Wind-Europe, *Floating offshore wind vision statement*, Report, 2017.

[6] DNVGL. 'Dnvgl-st-0119 - floating wind turbine structures'. (2018), [Online]. Available: https://www.google.com/maps/place/Brittany,+France/@47.3580864,-3.5823234,6.51z/data=!4m5!3m4!1s0x4811ca61ae7e8eaf:0x10ca5cd36df24b0!8m2!3d48.2020471!4d-2.9326435?hl=en.

[7] M. Tomren, *Design and numerical analysis of mooring systems for floating wind turbines*, Spesialisation project at NTNU, 2021.

[8] DNV, *Floating wind: The power to commercialize*, Report.

[9] A. Durakovic, 'World's largest floating wind farm takes final shape', *OffshoreWIND*, 2021.

[10] Windcrete, *Second offshore floating wind farm in scotland, kincardine, starts delivering energy.*

[11] Equinor. 'How hywind works'. (2021), [Online]. Available: https://www.equinor.com/en/what-we-do/floating-wind/how-hywind-works.html.

[12] ——, 'Hywind tampen'. (2021), [Online]. Available: https://www.equinor.com/en/what-we-do/hywind-tampen.html.

[13] ——, 'Equinor photos for press'. (2021), [Online]. Available: https://cloud.brandmaster.com/brandcenter/en/equinorbc/component/default/22936.

[14] Bluewater. 'Floating wind systems'. (2021), [Online]. Available: https://www.bluewater.com/products-technology/floating-wind-systems/.

[15] B. ideol. 'Bw ideol's first floater in operation'. (2021), [Online]. Available: https://www.bw-ideol.com/en/floatgen-demonstrator.

[16] M. Kai-Tung, L. Yong, K. Chi-Tat Thomas and W. Yongyan, *Mooring System Engineering for Offshore Structures.* Gulf Professional Publishing, 2019, ISBN: 9780128185513. [Online]. Available: https://search.ebscohost.com/login.aspx?direct=true&db=nlebk&AN=2005337&site=ehost-live.

[17] C. Subrata, *Handbook of Offshore Engineering (2-volume Set).* Elsevier Science, 2005, ISBN: 9780080443812. [Online]. Available: https://search.ebscohost.com/login.aspx?direct=true&db=nlebk&AN=248830&site=ehost-live.

[18] O. M. Faltinsen, *Sea loads on ships and offshore structures*, eng, Cambridge, 1990.

[19] K. Larsen, *Static equilibrium of a mooring line*, Lecture note, 2015.

[20] K. Larsen, *Axial stiffness of synthetic mooring lines – engineering models*, Memo - Equinor, 2021.

[21] DNV, *Best practice for analysis of mooring systems with polyester ropes*, 2015.

[22] S. Anchor and Chain. 'Stud link chain'. (2021), [Online]. Available: https://www.sotra.net/?produkter=stud-link-chain.

[23] Sotra-Anchor-and-Chain. 'Studless chain'. (2021), [Online]. Available: https://www.sotra.net/?produkter=studless-chain.

[24] Bridon, *Oil and gas*, Datasheet, 2013.

[25] S. Anchor and Chain. 'Shackles'. (), [Online]. Available: https://www.sotra.net/products/shackles/.

[26] VRYHOF, *Vryhof manual - the guide to anchoring*, 2015.

[27] R. Almeida. ‘Maersk wins 4-year contract from petrobras to launch some badass anchors’. (2012), [Online]. Available: https://gcaptain.com/maersk-wins-anchor-handling-contracts/.

[28] T. Kristiansen, *Marine dynamics -tmr 4182 marine dynamics - chapter 7*, 2019.

[29] DNVGL, *Dnvglrpc205 - environmental conditions and environmental loads*, 2019.

[30] D. of Marine Technology, *Marine dynamics - compendium in tmr 4182 marine dynamics*, 2019.

[31] ‘Aerodynamics of wind turbines’, in *Wind Energy Explained*. John Wiley & Sons, Ltd, 2010, ch. 3, pp. 91–155, ISBN: 9781119994367. DOI: https://doi.org/10.1002/9781119994367.ch3. eprint: https://onlinelibrary.wiley.com/doi/pdf/10.1002/9781119994367.ch3. [Online]. Available: https://onlinelibrary.wiley.com/doi/abs/10.1002/9781119994367.ch3.

[32] ‘Wind characteristics and resources’, in *Wind Energy Explained*. John Wiley & Sons, Ltd, 2009, ch. 2, pp. 23–89, ISBN: 9781119994367. DOI: https://doi.org/10.1002/9781119994367.ch2. eprint: https://onlinelibrary.wiley.com/doi/pdf/10.1002/9781119994367.ch2. [Online]. Available: https://onlinelibrary.wiley.com/doi/abs/10.1002/9781119994367.ch2.

[33] IEC-61400-1, *Wind energy generation systems - part 1: Design requirements*, IEC, 2019.

[34] ‘The wind resource’, in *Wind Energy Handbook*. John Wiley & Sons, Ltd, 2011, ch. 2, pp. 9–38, ISBN: 9781119992714. DOI: https://doi.org/10.1002/9781119992714.ch2. eprint: https://onlinelibrary.wiley.com/doi/pdf/10.1002/9781119992714.ch2. [Online]. Available: https://onlinelibrary.wiley.com/doi/abs/10.1002/9781119992714.ch2.

[35] B. Jonkman and L. Kilcher, ‘Turbsim user’s guide: Version 1.50’, National Renewable Energy Laboratory, Tech. Rep., 2012.

[36] SINTEF-Ocean, *Simo 4.20.2 theory manual*, 2021.

[37] E. Bachynski, *Tmr03 lecture note - basic aerodynamics for wind turbines*, 2021.

[38] E. Bachynski-Polic´, *Basic concepts in wind turbine control*, Lecture note in TMR-03 Integrated Dynamic Analysis of Wind Turbines, 2021.

[39] DNV, *Dnv-os-e301 - position mooring*, 2013.

[40] ——, *Dnvgl-st-0437 - loads and site conditions for wind turbines*, 2016.

[41] IEC, *Iec ts 61400-3-2 - wind energy generation systems – part 3-2: Design requirements for floating offshore wind turbines*, 2019.

[42] DNV, *Dnv-rp-h103 - modelling and analysis of marine operations*, 2011.

[43] K. Larsen, *Tmr4225 marine operations - lecture notes - station keeping and mooring of floating structures*, 2020.

[44] L.-h. Yuan, Y.-s. Ma, Y.-f. Zan and Z.-h. Wu, ‘Real-time method for calculating retardation functions’, *Journal of Marine Science and Technology*, vol. 25, no. 12, 2017, DOI: 10.6119/JMST-017-1226-12.

[45] Z. Gao, *Tmr03 - additional lecture notes – time-domain equations of motions*, 2021.

[46] SINTEF. ‘Sima’. (2021), [Online]. Available: https://www.sintef.no/en/software/sima/.

[47] ——, *Sima user guide*, 2021.

[48] SINTEF-OCEAN, *Riflex 4.20.2 theory manual*, 2021.

[49] K. Larsen and P. C. Sandvik, ‘Efficient Methods For The Calculation Of Dynamic Mooring Line Tension’, European Offshore Mechanics Symposium, vol. All Days, Aug. 1990.

[50] K. Larsen, *Time domain analysis overview*, 2021.

[51] SINTEF-OCEAN, *Riflex 4.20.2 user guide*, 2021.

[52] M. Yang, B. Teng, D. Ning and Z. Shi, ‘Coupled dynamic analysis for wave interaction with a truss spar and its mooring line/riser system in time domain’, *Ocean Engineering*, vol. 39, pp. 72–87, 2012, ISSN: 0029-8018. DOI: https://doi.org/10.1016/j.oceaneng.2011.11.002. [Online]. Available: https://www.sciencedirect.com/science/article/pii/S002980181100254X.

[53] K. C.T. and B. F.J., 'Mooring Line Dynamics: Comparison of Time Domain, Frequency Domain, and Quasi-Static Analyses', OTC Offshore Technology Conference, May 1991, OTC-6657-MS. DOI: 10.4043/6657-MS. eprint: https://onepetro.org/OTCONF/proceedings-pdf/91OTC/All-91OTC/OTC-6657-MS/1997242/otc-6657-ms.pdf. [Online]. Available: https://doi.org/10.4043/6657-MS.

[54] *Aerodynamic Roll-Yaw Instabilities of Floating Offshore Wind Turbines*, vol. Volume 9: Ocean Renewable Energy, International Conference on Offshore Mechanics and Arctic Engineering, V009T09A049, Aug. 2020. DOI: 10.1115/OMAE2020-18273. eprint: https://asmedigitalcollection.asme.org/OMAE/proceedings-pdf/OMAE2020/84416/V009T09A049/6695529/v009t09a049-omae2020-18273.pdf. [Online]. Available: https://doi.org/10.1115/OMAE2020-18273.

[55] F. d. P. Uggo and K. Rasmus, *Memo - jupiter - metocean summary*, Equinor, 2021.

[56] Google. 'Google maps - brittany'. (2021), [Online]. Available: https://www.google.com/maps/place/Brittany,+France/@47.3580864,-3.5823234,6.51z/data=!4m5!3m4!1s0x4811ca61ae7e8eaf:0x10ca5cd36df24b0!8m2!3d48.2020471!4d-2.9326435?hl=en.

[57] E. S. d. S. Carlos, A. B. Petter, E. Lene, B. Erin, E. Espen and H. Herbjørn, *Definition of the ino windmoor 12 mw base case floating wind turbine*, 2021.

[58] S. OCEAN, *Simo 4.20.2 user guide*, 2021.

[59] Ramnäs, *Ramnäs bruk product catalogue*, 2017.

[60] G. Benassai, A. Campanile, V. Piscopo and A. Scamardella, 'Ultimate and accidental limit state design for mooring systems of floating offshore wind turbines', *Ocean Engineering*, vol. 92, pp. 64–74, 2014, ISSN: 0029-8018. DOI: https://doi.org/10.1016/j.oceaneng.2014.09.036. [Online]. Available: https://www.sciencedirect.com/science/article/pii/S0029801814003692.

[61] M. Brommundt, L. Krause, K. Merz and M. Muskulus, 'Mooring system optimization for floating wind turbines using frequency domain analysis', *Energy Procedia*, vol. 24, pp. 289–296, 2012, Selected papers from Deep Sea Offshore Wind R&D Conference, Trondheim, Norway, 19-20 January 2012, ISSN: 1876-6102. DOI: https://doi.org/10.1016/j.egypro.2012.06.111. [Online]. Available: https://www.sciencedirect.com/science/article/pii/S1876610212011514.

[62] K. Xu, K. Larsen, Y. Shao, M. Zhang, Z. Gao and T. Moan, 'Design and comparative analysis of alternative mooring systems for floating wind turbines in shallow water with emphasis on ultimate limit state design', *Ocean Engineering*, vol. 219, p. 108 377, 2021, ISSN: 0029-8018. DOI: https://doi.org/10.1016/j.oceaneng.2020.108377. [Online]. Available: https://www.sciencedirect.com/science/article/pii/S0029801820312841.

[63] Y. Chevillotte, Y. Marco, G. Bles *et al.*, 'Fatigue of improved polyamide mooring ropes for floating wind turbines', *Ocean Engineering*, vol. 199, p. 107 011, 2020, ISSN: 0029-8018. DOI: https://doi.org/10.1016/j.oceaneng.2020.107011. [Online]. Available: https://www.sciencedirect.com/science/article/pii/S0029801820300883.

Appendix

A Time Series chain mooring system

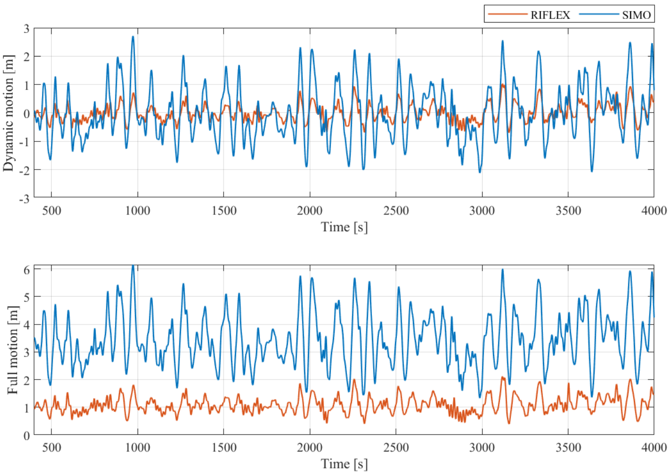

Figure A.1: Time series of FWT sway motion during DLC 6.1 acting towards 0° for the SIMO- and RIFLEX-model.

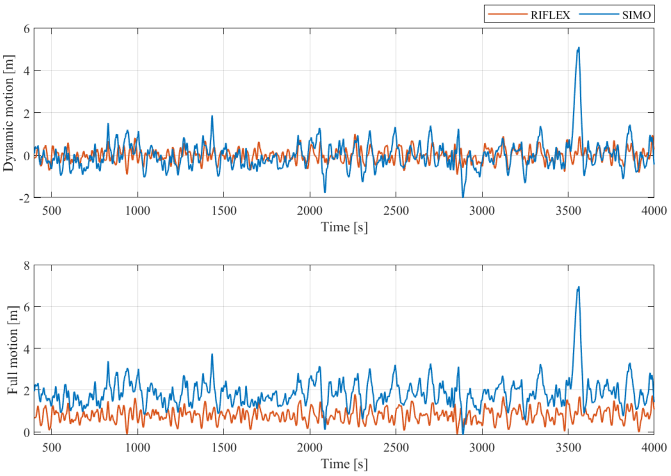

Figure A.2: Time series of FWT yaw motion during DLC 6.1 acting towards 0° for the SIMO- and RIFLEX-model.

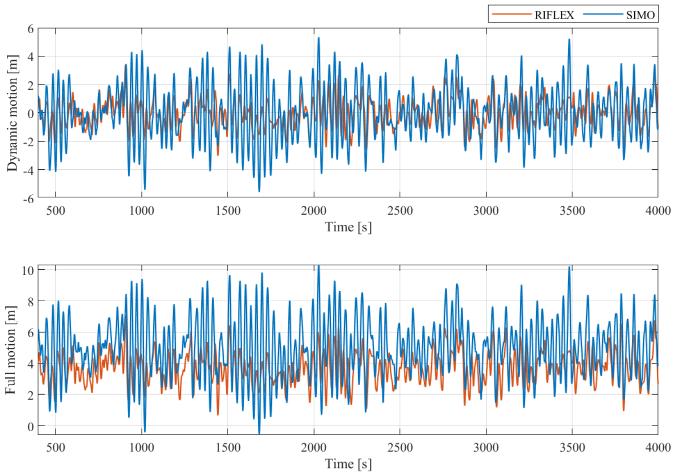

Figure A.3: Time series of FWT roll motion during DLC 6.1 acting towards 180° for the SIMO- and RIFLEX-model.

B Tension synthetic mooring systems

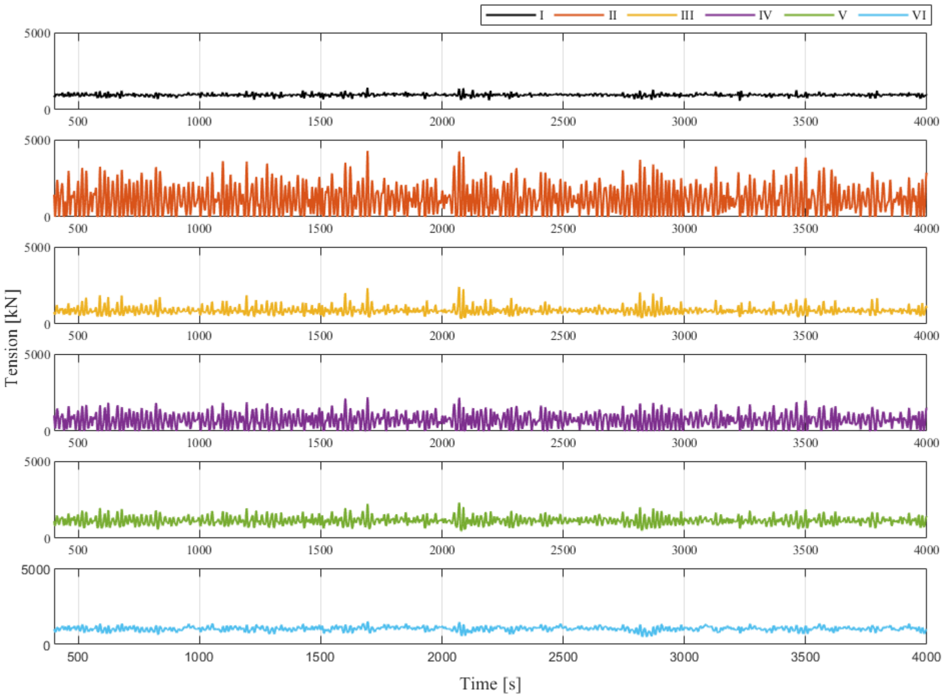

Figure B.1: Time series of mooring line tension in mooring line 3 during DLC 6.1 acting towards 180° for all systems.

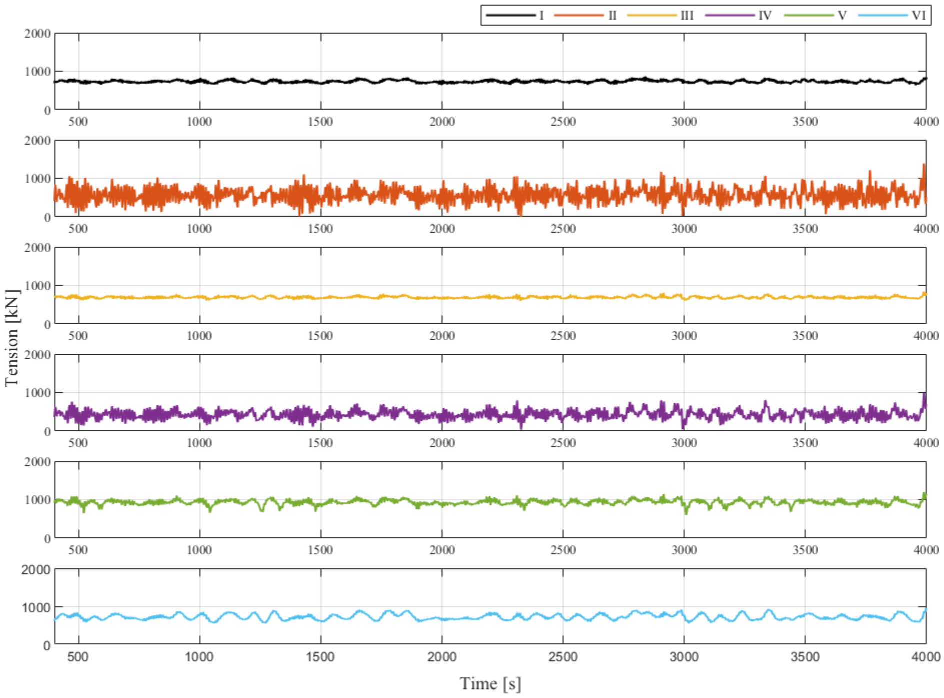

Figure B.2: Time series of mooring line tension in mooring line 1 during DLC 1.1R acting towards 180° for all systems.

Mathias Tomren

Design and Numerical Analysis of Mooring Systems for Floating Wind Turbines

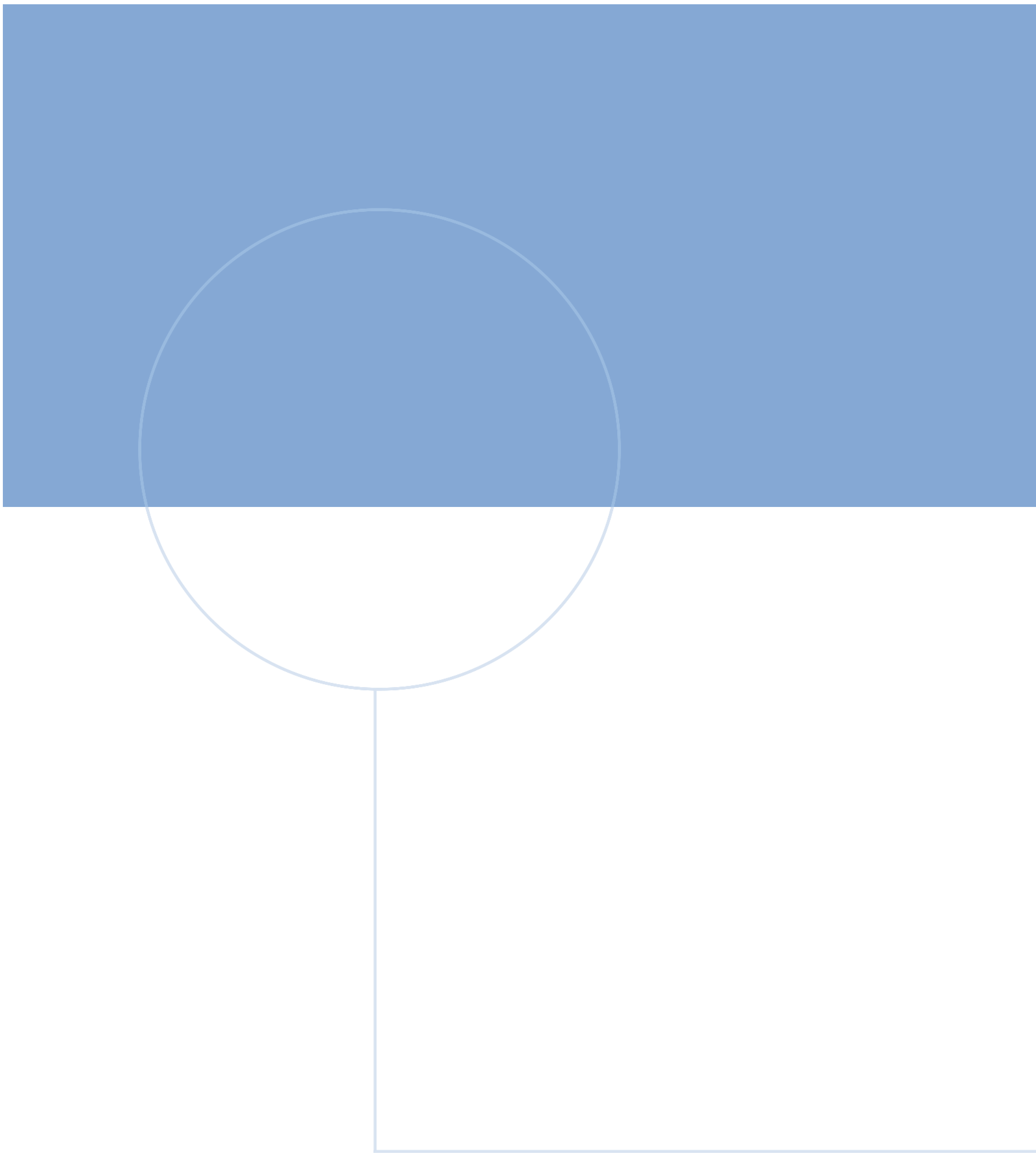

NTNU
Kunnskap for en bedre verden